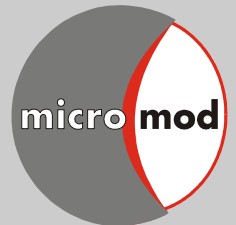


micromod Partikeltechnologie GmbH

modular designed particles



Technological Applications

Publications and Reviews

magnetic micro- and nanoparticles

Implementation in Life Sciences

www.micromod.de

Product overview

	10 nm	100 nm	1 µm	10 µm	100 µm	Product matrix
Magnetic particles	20 nm – 500 nm					dextran
		80 nm – 100 nm				bionized nanoferrite
			2 - 12 µm			polystyrene
				30 µm - 100 µm		poly(lactic acid)
		350 nm - 6 µm				silica
		150 nm				poly(ethylene imine)
		150 nm				chitosan
		50 - 250 nm				iron oxide
Fluorescent particles	10 nm – 20 µm					silica
	25 nm		6 µm			polystyrene, polymethacrylate
		250 nm		100 µm		poly(lactic acid)
Fluorescent magnetic particles		250 nm				albumin
		100 nm - 300 nm				dextran
		100 nm		30 µm - 100 µm		bionized nanoferrite poly(lactic acid)
White particles	10 nm – 20 µm					silica
	25 nm			100 µm		polystyrene, polymethacrylate
		250 nm		100 µm		poly(lactic acid)
		300 nm				latex
		250 nm				albumin
Colored particles		100 nm		100 µm		silica
			1 µm - 12 µm			polystyrene
		250 nm		100 µm		poly(lactic acid)
	10 nm	100 nm	1 µm	10 µm	100 µm	

micromod Partikeltechnologie GmbH
Friedrich-Barnewitz-Straße 4, D-18119 Rostock
Tel.: +49 381/54 34 56 10, Fax: +49 381/54 34 56 20
Technical Support Tel.: +49 381/54 34 56 14
E-mail: info@micromod.de, Internet: www.micromod.de

magnetic micro- and nanoparticles

Contents

	page
1 Introduction	2
2 Magnetic nano- and microparticles	4
2.1 Overview	4
2.2 Types of magnetic nano- and microparticles	4
2.3 Types of fluorescent magnetic nano- and microparticles	9
3 Terminology and characteristics of magnetic nanoparticles	12
3.1 Classification of magnetic materials	12
3.2 Magnetic anisotropy, domain structure and superparamagnetism	13
3.3 Relaxation behavior und frequency dependent susceptibility	14
4 Magnetic nano- and microparticles for biosensor applications	16
4.1 Introduction	16
4.2 Read-out Systems	17
4.3 Applications of substrate-based biosensor systems	22
4.4 Applications of substrate-free biosensor systems	26
4.5 Summary	32
5 Magnetic nanoparticles as contrast agents in Magnetic Resonance Imaging (MRI)	39
5.1 Introduction	39
5.2 MR imaging for diagnosis and therapy	41
5.3 MR imaging of MNPs in environmental systems	43
6 Magnetic nanoparticles for hyperthermia applications	46
6.1 Introduction	46
6.2 Characterization of MNPs for hyperthermia application	47
6.3 Basic studies on advantages and limitations of hyperthermia with MNPs	48
6.4 Non-temperature induced effects of magnetized MNPs in AMF in cancer cells	51
6.5 Hyperthermia for immune-related therapies	52
6.6 Summary	53
7 Magnetic nanoparticles as tracers for Magnetic Particle Imaging (MPI)	56
7.1 Introduction	56
7.2 Enhancement of the MPI technique to improve the imaging quality	57
7.3 Biomedical imaging applications	58
8 Targeting applications with magnetic nanoparticles	61
8.1 Magnetic nanoparticles for targeted magnetic resonance imaging (MRI) applications	61
8.2 MNPs for targeted magnetic particle imaging (MPI) applications	65
8.3 MNPs for targeted multimodal imaging purposes	65
8.4 Magnetic nanoparticles for targeted hyperthermia applications	66
8.5 Delivery of therapeutic molecules and MNPs inside cells by nontransgenic approaches	68
8.6 Biomimetic amplification of nanoparticle homing to tumors	68
9 Magnetic nanoparticles for stem cell tracking in soft tissue engineering approaches	71
10 Applications of fluorescent magnetic particles	73
10.1 Combination of optical imaging with Magnetic Resonance Imaging (MRI) or Magnetic Particle Imaging (MPI)	73
10.2 Visualization of MNPs at controlled apoptosis by nanoparticle rotation in dynamic magnetic fields	75
10.3 Nanoparticle-assisted optical tethering of endosomes (NOTE)	75
11 Magnetic silica particles for radionuclide extraction	77

1 Introduction

For more than 20 years, **micromod Partikeltechnologie GmbH** has been the reliable supplier of magnetic nano- and microparticles located in Rostock. The focus of micromod as a technology-oriented company is directed to the development and the production of monodisperse micro- and nanoparticles. The particles are made from various materials, including different sizes and covering a large spectrum of physical and chemical modifications. This has been widely utilized by our customers which have performed studies with micromod's magnetic micro- and nanoparticles.

The manifold application fields of magnetic micro- and nanoparticles comprise for example

- the separation of biomolecules like proteins or nucleic acids,
- the separation and sorting of cells,
- the separation of radionuclides or other metal ions,
- magnetic resonance imaging (MRI) and magnetic particle imaging (MPI),
- hyperthermia with alternating magnetic fields,
- biosensor and lab-on chip design,
- homing and tracking of stem cells,
- the specific targeting of cells and organs, or
- the magnetic supply and removal of reagents.

All these applications require customized physical, chemical and biochemical particle properties. Therefore micromod provides a large variety of magnetic particles with different magnetic properties, diameters, matrix materials and surface functionalizations.

We offer various products for separation with permanent magnets or for separation using high gradient magnetic fields.

Magnetic particles for separation *with permanent magnets* are provided in the size range from 130 nm – 100 µm:

- nanomag[®]-D - dextran based nanoparticles with magnetite core material
- PEI-M particles - nanoparticles with a poly(ethylene imine) coating
- Iron oxide particles - nanoparticles based on clusters of magnetite crystals
- micromer[®]-M - polystyrene based microspheres
- sicastar[®]-M - silica based microparticles
- sicastar[®]-M-CT - cluster-typed magnetic silica microparticles
- PLA-M particles - poly(lactic acid) based microparticles

Magnetic nanoparticles for separation *in high gradient magnetic field* possess particle sizes between 20 and 100 nm:

- nanomag[®]-D-spio - iron oxide embedded into a dextran matrix
- nanomag[®]-CLD-spio - iron oxide embedded into a matrix of cross-linked dextran

magnetic micro- and nanoparticles

Our assortment of magnetic particles is completed by particle types with a special design of magnetic properties.

- Bionized NanoFerrite - magnetic dextran or hydroxyethyl starch nanoparticles

Bionized NanoFerrite (BNF) particles are thermally blocked at room temperature and suitable for hyperthermia treatment.

- perimag® - dextran coated magnetic nanoparticles

Particles of perimag® series are designed for imaging applications (MPI, MRI) and are employable for homing and tracking of stem cells as well as for hyperthermia treatment.

Micromod is the reliable supplier of magnetic nano- and microparticles as system components for *in-vitro* diagnostics, high-throughput screening, magnetic bioseparation, cell labeling as well as for research and development of novel diagnosis and therapy methods.

A modern quality management according to EN ISO 13485 in combination with a sophisticated particle analysis system allows the micromod Partikeltechnologie GmbH to ensure customers (predominantly producers of diagnostic kits and high-throughput equipment, biotechnology companies and various research institutions) a high quality standard in all product categories. Selected types of magnetic particles can be manufactured under clean room conditions upon request.

This brochure provides a review of third party papers on applications of micromod's magnetic nano-and microparticles

- in biosensors and bioassays,
- as contrast agent for Magnetic Resonance Imaging (MRI),
- as tracer for Magnetic Particle Imaging (MPI),
- in magnetic field assisted hyperthermia,
- for selective targeting applications,
- for homing and tracking of stem cells,
- in combination with fluorescence labeling for optical imaging, and
- for magnetic separation of radionuclides or other metal ions.

2 Magnetic nano- and microparticles

Cordula Grüttner

micromod Partikeltechnologie GmbH, Friedrich-Barnewitz-Str. 4, 18119 Rostock, Germany

2.1 Overview

In the recent years, **micromod** has developed a large variety of magnetic nano- and microparticle types. The development of each particle type was with emphasis on a specific application in theranostics. The particle sizes range from only a few nanometers up to several micrometers. Most of the particles are available with different surface coatings and can be specifically linked to biomolecules like proteins or antibodies.

	Product matrix	10 nm	100 nm	1 μm	10 μm	100 μm	Product type
magnetic particles	dextran		20 nm – 100 nm				nanomag®-D-spio, -CLD-spio
	dextran			130 nm – 500 nm			nanomag®-D, -CLD, -silica
	dextran		130 nm				perimag®
	bionized nanoferrite		80 nm – 100 nm				BNF particles
	polystyrene			2 - 12 μm			micromer®-M
	poly(lactic acid)					30 μm-100 μm	PLA-M particles
	silica			350 nm - 6 μm			sicastar®-M, sicastar®-M-CT
	poly(ethylene imine)		150 nm				PEI-M particles
	chitosan		150 nm				nanomag®-C
	iron oxide		50 - 250 nm				Iron oxide particles
fluorescent magnetic particles	dextran		100 nm - 300 nm				nanomag®-CLD-F
	bionized nanoferrite		100 nm				BNF-F particles
	poly(lactic acid)					30 μm-100 μm	PLA-M-F particles

2.2 Types of magnetic nano- and microparticles

2.2.1 nanomag®-D

nanomag®-D are available with particle diameters of 130 nm, 250 nm and 500 nm and can be separated with a permanent magnet. The particles are prepared via the core-shell method with a core of magnetite and a dextran shell consisting of 75-80% (w/w) magnetite in a matrix of dextran (40.000 Da). Due to the irregular shape of the iron oxide multicore the nanoparticles are

partially thermally blocked at room temperature. Also due to the relatively fast separation of the nanomag®-D, the particles are very interesting for several substrate based biosensor schemes. Exemplary separation processes of 500 nm nanomag®-D particles are shown in Fig. 1.

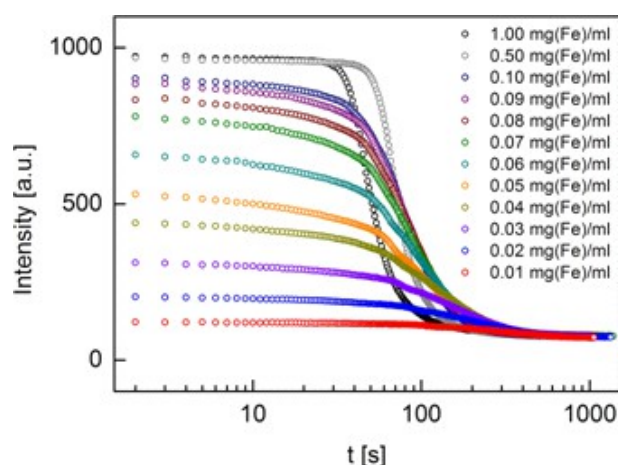


Fig. 1: Separation process of nanomag®-D for different iron concentrations.

magnetic micro- and nanoparticles

The nanomag®-D are designed with the surface functionalities OH (plain), NH₂ and COOH for the covalent binding of proteins, antibodies or other molecules. They are also available with covalently bound proteins (avidin, streptavidin, protein A, albumin) or other biomolecules (biotin, glutathion), and can be provided with covalently bound antibodies on request. They are offered with nickel(II) chelator nitrilotriacetic acid (NTA) or ready to use with the corresponding nickel complex (Ni-NTA) for the binding of histidine labeled proteins. These particles are also available with various hydrophilic surfaces (PEG 300, PEG-NH₂ or PEG-COOH) and with negative surface potentials (e.g. COOH, SO₃H).

2.2.2 nanomag®-D-spio

The superparamagnetic nanomag®-D-spio are available with particle diameters of 20 nm, 50 nm and 100 nm and cannot be separated with a conventional permanent magnet but in a high gradient magnetic field (magnetic column). The particles are prepared by precipitation of iron oxide in the presence of dextran. The functionalized nanomag®-D-spio consist of about 55-85% (w/w) iron oxide in a matrix of dextran (40.000 Da) in dependence on the diameter and surface modification. The particles show differences in the size of the iron oxide domains for different particle diameters. These particles are preferably applied for detection purposes in magnetic resonance imaging (MRI) or in magneto-immuno assays and show good specific power absorption rates for hyperthermia applications for a particle diameter of 100 nm.

The particles are designed with the surface functionalities OH (plain), NH₂ and COOH for the covalent binding of proteins, antibodies or other molecules and are available with covalently bound proteins (avidin, streptavidin, protein A, albumin) or other biomolecules (e.g. biotin) as well as with various hydrophilic surfaces (PEG 300, PEG-NH₂ or PEG-COOH).

2.2.3 perimag®

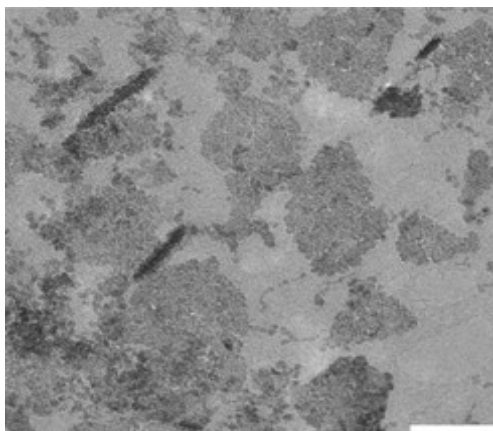


Fig. 2: Exemplary TEM image of perimag® nanoparticles [1]. The bar indicates 50 nm

perimag® exhibit excellent properties as contrast agents for Magnetic Resonance Imaging (MRI) and Magnetic Particle Imaging (MPI) [1, 3, 4]. The particles are suitable for homing and tracking of stem cells in regenerative medicine as well as for hyperthermia applications [5]. They are prepared by precipitation of iron oxide in the presence of dextran and are available with a particle diameter of 130 nm. The iron oxide crystals have sizes between 3 nm and 8 nm clustered to multi-core particles that are mostly superparamagnetic (Fig. 2) [1]. The particles cannot be separated with a conventional permanent magnet but in a high gradient magnetic field.

magnetic micro- and nanoparticles

The perimag® are designed with the surface functionalities OH (plain), NH₂ and COOH for the covalent binding of proteins, antibodies or other molecules [6] and are available with covalently bound streptavidin for the binding of biotinylated molecules. Furthermore, the particles can be manufactured under clean room conditions upon request.

2.2.4 nanomag®-CLD

nanomag®-CLD are prepared via the core-shell method with a core of magnetite and a dextran shell. The particles are available with particle diameters of 300 nm and 500 nm for separation with a permanent magnet.

They are designed with NH₂, COOH and PEG-COOH for the covalent binding of proteins, antibodies or other molecules and are available with covalently bound streptavidin or other protein surfaces on request.

2.2.5 nanomag®-CLD-spio

Superparamagnetic nanomag®-CLD-spio are prepared by precipitation of iron oxide in the presence of dextran and are available with particle diameters of 20 nm and 100 nm. They cannot be separated with a conventional permanent magnet but in a high gradient magnetic field. The particles consist of about 70-90% (w/w) iron oxide in a matrix of cross-linked dextran (40.000 Da) in dependence on the diameter and surface modification. The particles show differences in the size of the iron oxide domains for different particle diameters. nanomag®-D-spio are preferably applied for detection purposes in magnetic resonance imaging or in magneto-immuno assays and show good specific power absorption rates for hyperthermia applications for a particle diameter of 100 nm.

The particles are designed with amino groups on the surface for the covalent binding of proteins, antibodies or other molecules and can be provided with covalently bound antibodies on request.

2.2.6 BNF particles

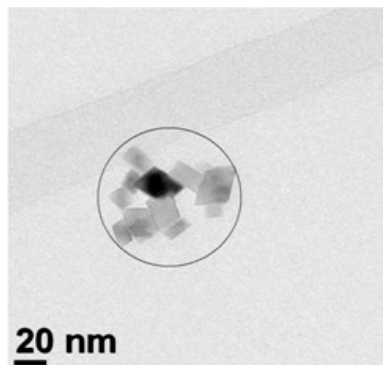


Fig. 3: Exemplary TEM image of BNF starch nanoparticles [2].

BNF particles (BNF – bionized nanoferrites) are prepared via the core-shell method with a core of 75-80% (w/w) magnetite and a shell of dextran or hydroxyethyl starch. The particles are available with particle diameters of 80 nm and 100 nm. BNF particles are magnetic multicore nanoparticles as presented in Fig. 3. They are thermally blocked at room temperature and show specific interaction with alternating magnetic fields [7-11]. 100 nm BNF particles can be separated with conventional permanent magnets, and 80 nm BNF particles have to be separated in high gradient magnetic fields or for several hours at a strong permanent magnet. Due to their specific relaxation behaviour

magnetic micro- and nanoparticles

in the presence of an alternating magnetic field, as presented in Fig. 4, these particles are also of special interest for substrate-free biosensors.

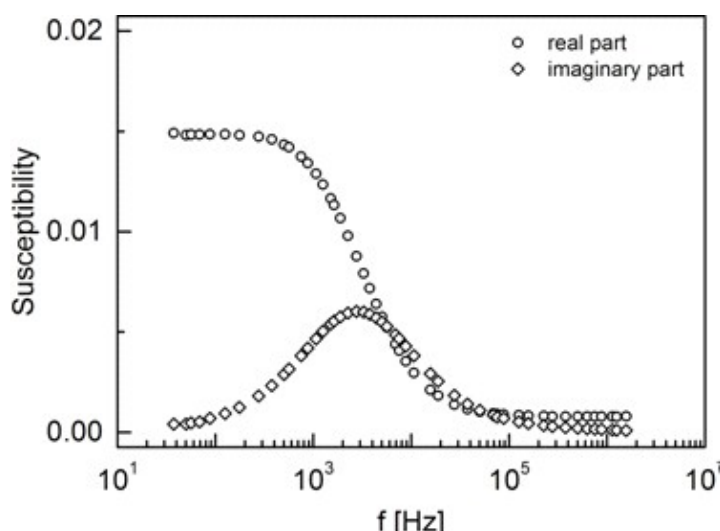


Fig. 4: AC susceptibility measurement of the BNF 80 nanoparticles

The particles are designed with the surface functionalities OH (plain), NH₂, PEG-NH₂, COOH and PEG-COOH for the covalent binding of proteins, antibodies or other molecules. They are available with covalently bound proteins (streptavidin, protein A) and can be provided with covalently bound antibodies on request. The particles can easily be filtered through 0.22 μm filters.

2.2.7 micromer®-M

micromer®-M are monodisperse particles which consist of magnetite around an organic matrix of a styrene-maleic acid-copolymer (Fig. 5). They are finally coated with a polymer layer for the encapsulation of magnetite and the introduction of chemical functionalities and can easily be separated with conventional permanent magnets. The particles are provided as standard products in the size range of 2 to 12 microns.

micromer®-M are designed with the surface functionalities NH₂, PEG-NH₂, COOH and PEG-COOH for the covalent binding of proteins, antibodies or other molecules and are available with covalently bound proteins (avidin, streptavidin, protein A, albumin) or other polymers (polyethylene imine (PEI)). Especially strept-avidin coated micromer®-M particles are interesting tools for certain substrate-based biosensor schemes also with the possibility to detect single particles [12].

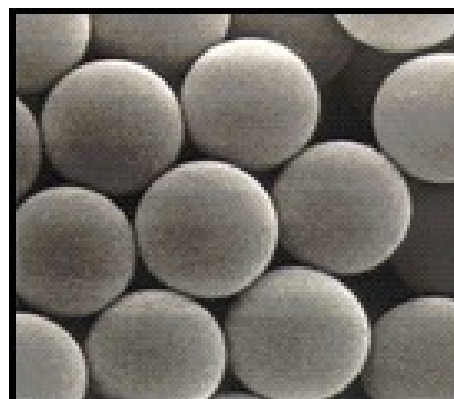


Figure 5. SEM image of 3 μm micromer®-M particles

magnetic micro- and nanoparticles

2.2.8 sicastar®-M

sicastar®-M are available with mean diameters of 350 nm or 1.5 μm . They are produced by hydrolysis of orthosilicates in the presence of magnetite and have a hydrophilic surface with terminal Si-OH-bonds (plain). The particles have monomodal size distributions, and can easily be separated with conventional permanent magnets. sicastar®-M are extremely stable in organic solvents and at high temperatures.

The particles are designed with the surface functionalities NH_2 , COOH , N-hydroxysuccinimide (NHS) and epoxy for the covalent binding of proteins, antibodies or other molecules. They are available with covalently bound proteins (avidin, streptavidin, protein A, albumin) and biotin and can be offered with nickel(II) chelator nitrilotriacetic acid (NTA) or ready to use with the corresponding nickel complex (Ni-NTA) for the binding of histidine labeled proteins. Furthermore, sicastar®-M are available with a hydrophobic octadecyl (C18) surface and are deliverable with an organic polymer shell (core-shell method) on request.

2.2.9 sicastar®-M-CT

sicastar®-M-CT consist of aggregates in the size range of 3 - 30 μm with a mean diameter of 6 microns. The particles are produced by hydrolysis of orthosilicates in the presence of magnetite and show a homogeneous distribution of magnetite in the silica matrix due to the special preparation method. They have a hydrophilic surface with terminal Si-OH-bonds and can easily be separated even in highly viscous media with conventional permanent magnets. sicastar®-M-CT are extremely stable in organic solvents and at high temperatures.

The particles are designed with the surface functionalities OH (plain), NH_2 , COOH and epoxy for the covalent binding of proteins, antibodies or other molecules and are available with covalently bound proteins (avidin, streptavidin, protein A, albumin). sicastar®-M-CT can be offered with nickel(II) chelator nitrilotriacetic acid (NTA) or ready to use with the corresponding nickel complex (Ni-NTA) for the binding of histidine labeled proteins and are available with a hydrophobic octadecyl (C18) surface.

2.2.10 nanomag®-silica

nanomag®-silica are prepared via the core-shell method with a core of magnetite and a dextran shell with a simultaneous cross-linking of the dextran strands by silica nanostructures. The particles have a diameter of 250 nm and a magnetite content of 75-80%. These particles can easily be separated with a conventional permanent magnet.

nanomag®-silica are designed with the surface functionalities OH (plain), NH_2 and COOH for the covalent binding of proteins, antibodies or other molecules and are available with the hydrophobic octadecyl (C18) surface especially for nucleic acid separation.

magnetic micro- and nanoparticles

2.2.11 nanomag®-C

nanomag®-C are prepared via the core-shell method with a core of magnetite and a chitosan shell and have a diameter of 150 nm and a magnetite content of 75-80%. They can easily be separated with a conventional permanent magnet. The particles have already amino functionalities without any further surface modifications (surface: plain).

2.2.12 PLA-M particles

PLA-M particles consist of magnetite (40% w/w) in a matrix of poly(D,L-lactic acid) with a molecular weight of 17.000 Da. The particles are available with mean diameters of 30 μm and 100 μm . They are established in the field of magnetic drug targeting in connection with a controlled drug release. The half-life time of the beads under *in-vivo* conditions mainly depends on the molecular weight of the polymers and increases with the molecular weight of the polymer. The PLA-M particles can also be offered with carboxylic acid or amino groups on the surface and can be loaded with drugs on request.

2.2.13 PEI-M particles

PEI-M particles are prepared via the core-shell method with a core of magnetite and a poly(ethylene imine) shell. The particles have a diameter of 150 nm and a magnetite content of 75-80% and can be separated with a conventional permanent magnet.

2.2.14 Iron oxide particles

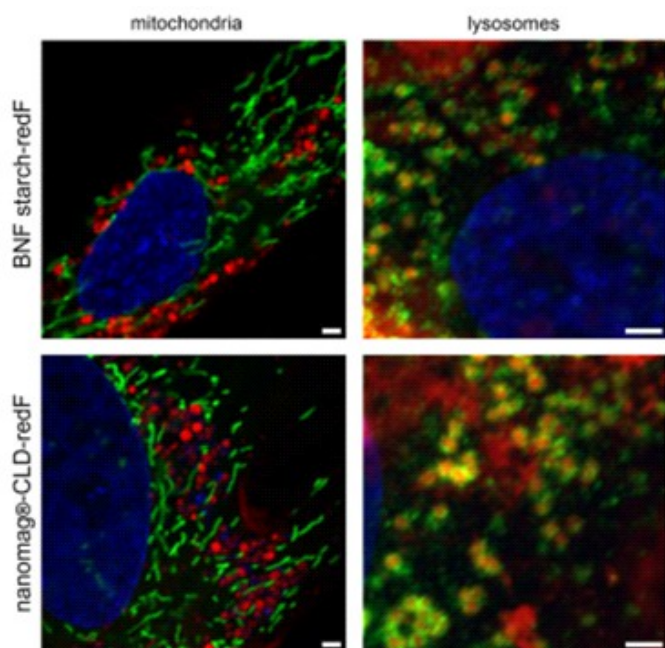
Iron oxide particles are available with hydrodynamic diameters of 50 nm and 250 nm. The surface of the 50 nm particles is colloidal stabilized with carboxylic acid groups. The 50 nm particles possess nearly no sedimentation tendency and cannot be separated with conventional permanent magnets. For magnetic separation a high gradient magnetic system is recommended. The 250 nm iron oxide particles consist of monodisperse magnetite aggregates and can be separated with permanent magnets. They possess a low tendency of sedimentation and are also available with gold labeling.

2.3 Types of fluorescent magnetic nano- and microparticles

Fluorescent magnetic particles allow the application of magnetic properties together with the ability of optical visualization. Selected magnetic particles of **micromod's** standard assortment are available with a green or red fluorescence. Customized magnetic particles are available with specific fluorescent dyes on request.

2.3.1 nanomag[®]-CLD-redF

nanomag[®]-CLD-redF particles show a red fluorescence (excitation: 552 nm, emission: 580 nm). The 100 nm nanomag[®]-CLD-redF particles are prepared by precipitation of iron oxide in the presence of dextran. They consist of about 80-90% (w/w) iron oxide in a matrix of crosslinked



dextran (40.000 Da) and cannot be separated with a conventional permanent magnet but in a high gradient magnetic field. The 300 nm nanomag[®]-CLD-redF are prepared by the core-shell method. They consist of about 80-90% (w/w) iron oxide in a matrix of crosslinked dextran (40.000 Da) and can easily be separated with conventional permanent magnets. The nanomag[®]-CLD-redF particles are available with a plain surface, e.g. for stem cell labeling [13] (Fig. 8) or with amino groups on the surface for the covalent binding of proteins, antibodies or other molecules [14, 15].

Figure 8. Intracellular localization of nanoparticles. Confocal laser scanning images of stem cells labeled with BNF-Starch-redF or nanomag[®]-CLD-redF and stained for mitochondria and lysosomes (both shown in green). Cell's nuclei were counterstained with Hoechst 33342 (blue).

2.3.2 BNF-F

BNF-redF particles have a red fluorescence (excitation: 552 nm, emission: 580 nm). They are thermally blocked at room temperature and show specific interaction with alternating magnetic fields. Fluorescent BNF particles are prepared via the core-shell method with a core of 75-80% (w/w) magnetite and a shell of crosslinked dextran (BNF-Dextran-redF) or crosslinked hydroxyethyl starch (BNF-Starch-redF). They are available with a particle diameter of 100 nm and can be separated with strong conventional permanent magnets. BNF-F possess a plain surface or amino groups on the surface for the covalent binding of proteins, antibodies or other molecules. They are available with covalently bound streptavidin for the binding of biotinylated biomolecules.

2.3.3 PLA-M-F

Fluorescent PLA-M particles consist of magnetite (40% w/w) in a matrix of poly(D,L-lactic acid) with a molecular weight of 17.000 Da. They are available with mean diameters of 30 μm and 100 μm (broader size distributions) and with red fluorescence (PLA-M-redF, excitation: 552 nm, emission: 580 nm) or green fluorescence (PLA-M-greenF, excitation: 502 nm, emission: 527 nm). The fluorescent PLA-M particles can be loaded with drugs on request.

References

- [1] Eberbeck, D., et al., *Multicore magnetic nanoparticles for magnetic particle imaging*. IEEE TRANSACTIONS ON MAGNETICS, 2013. **49**(1): p. 269-274.
- [2] Ludwig, F., et al., *Magnetic, Structural, and Particle Size Analysis of Single-and Multi-Core Magnetic Nanoparticles*. Magnetics, IEEE Transactions on, 2014. **50**(11): p. 1-4.
- [3] Konkle, J.J., et al., *A Convex Formulation for Magnetic Particle Imaging X-Space Reconstruction*. PloS one, 2015. **10**(10): p. e0140137.
- [4] Zheng, B., et al., *Quantitative Magnetic Particle Imaging Monitors the Transplantation, Biodistribution, and Clearance of Stem Cells In Vivo*. Theranostics, 2016. **6**(3): p. 291-301.
- [5] Kilian, T., et al., *Stem cell labeling with iron oxide nanoparticles: impact of 3D culture on cell labeling maintenance*. Nanomedicine, 2016. **11**(15): p. 1957-1970.
- [6] Drews, L.B., et al. *Imaging atherosclerotic plaques in vivo using peptide-functionalized iron oxide nanoparticles*. in *Magnetic Particle Imaging (IWMPI), 2013 International Workshop on*. 2013. IEEE.
- [7] Dennis, C., et al., *The influence of collective behavior on the magnetic and heating properties of iron oxide nanoparticles*. Journal of Applied Physics, 2008. **103**(7): p. 07A319.
- [8] Dennis, C., et al., *The influence of magnetic and physiological behaviour on the effectiveness of iron oxide nanoparticles for hyperthermia*. Journal of Physics D: Applied Physics, 2008. **41**(13): p. 134020.
- [9] Dennis, C., et al., *Nearly complete regression of tumors via collective behavior of magnetic nanoparticles in hyperthermia*. Nanotechnology, 2009. **20**(39): p. 395103.
- [10] Krycka, K., et al., *Internal magnetic structure of dextran coated magnetite nanoparticles in solution using small angle neutron scattering with polarization analysis*. Journal of Applied Physics, 2011. **109**(7): p. 07B513.
- [11] Bordelon, D.E., et al., *Magnetic nanoparticle heating efficiency reveals magneto-structural differences when characterized with wide ranging and high amplitude alternating magnetic fields*. Journal of Applied Physics, 2011. **109**(12): p. 124904.
- [12] Lagae, L., et al., *On-chip manipulation and magnetization assessment of magnetic bead ensembles by integrated spin-valve sensors*. Journal of Applied Physics, 2002. **91**(10): p. 7445-7447.
- [13] Kasten, A., et al., *Comparative In Vitro Study on Magnetic Iron Oxide Nanoparticles for MRI Tracking of Adipose Tissue-Derived Progenitor Cells*. PloS one, 2014. **9**(9): p. e108055.
- [14] Rimkus, G., et al., *mVCAM-1 specific iron oxide nanoparticles based probes for multimodal imaging purposes*. Biomed Tech, 2012. **57**: p. 77-80.
- [15] Zhang, E., et al., *Dynamic Magnetic Fields Remote-Control Apoptosis via Nanoparticle Rotation*. ACS Nano, 2014. **8**(4):**3192-201**(8(4)): p. 3192-201.

3 Terminology and characteristics of magnetic nanoparticles

Kerstin Witte^{1,2}, Fritz Westphal²

¹ University of Rostock, Institute of Physics, Albert-Einstein-Str. 23, 18059 Rostock, Germany

² micromod Partikeltechnologie GmbH, Friedrich-Barnewitz-Str. 4, 18119 Rostock, Germany

3.1 Classification of magnetic materials

If a material is placed in an external magnetic field \mathbf{H} , the individual magnetic moments of each atom will contribute to the overall magnetic induction \mathbf{B} :

$$\mathbf{B} = \mu_0(\mathbf{H} + \mathbf{M}), \quad (1)$$

where μ_0 is the vacuum permeability and \mathbf{M} the magnetization. All materials show some kind of magnetic behavior which essentially depends on the atomic structure and the temperature of the material. The magnetic behavior can be classified using the magnetic susceptibility χ :

$$\mathbf{M} = \chi\mathbf{H}. \quad (2)$$

Eq. (1) describes the magnetization which is induced by the external magnetic field. For diamagnets χ is negative and in the range of -10^{-3} up to -10^{-6} [1]. Diamagnetic behavior is present in every material, but can only be observed when no other magnetic behavior is present [2]. Most materials show small positive response in the presence of an external magnetic field. These materials are called paramagnets and their susceptibility is in the order of 10^{-6} up to 10^{-1} [1]. Here each atom in the materials has a small randomly oriented magnetic moment and the interactions between the magnetic moments are negligible. When an external field is applied the magnetic moments start to align, thus a net magnetization proportional to the external magnetic field can be observed.

Some materials also show ordered magnetic states at certain temperatures. Here, three different classes of materials can be distinguished – ferromagnets, ferrimagnets and antiferromagnets. In ferromagnetic materials the magnetic moments of each atom strongly interact with the neighboring magnetic moments leading to a parallel alignment of the moments [2]. The magnetic moments are spontaneously magnetized in regions of uniform magnetization so called domains. The response of such a ferromagnetic material is nonlinear and a hysteresis can be observed. The schematic of a hysteresis is presented in Fig. 1. After the initial magnetization of the ferromagnet in an external field the saturation magnetization M_s is reached. This magnetization corresponds to a complete alignment of the domains along the external

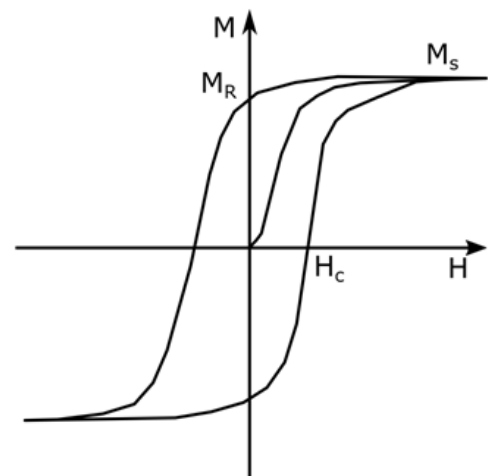


Fig. 1: Schematics of the initial magnetization curve and the hysteresis loop of a ferromagnet with main points of interest

magnetic micro- and nanoparticles

magnetic field. If the external magnetic field is reduced to zero after a first saturation of the sample, the magnetization does not reduce to zero. The magnetization left without an external magnetic field is the remanence M_R . If the magnetic field is reversed, the magnetization will further decrease and reach zero again. The magnetic field at this point is called coercivity H_c [2]. In antiferromagnetic materials the interaction between neighboring atoms is strongly negative. This leads to an antiparallel alignment of the neighboring magnetic moments. Furthermore only one kind of magnetic moment is present in the material, wherefore the antiparallel alignment of the moments leads to a net magnetic moment of zero [2]. Ferrimagnetism is normally observed in materials with two or more different species of magnetic moments. The interaction between neighboring atoms is also strongly negative, but in contrast to the antiferromagnets the magnetic moments of the atoms do not cancel out completely [2].

3.2 Magnetic anisotropy, domain structure and superparamagnetism

Ferro- and ferrimagnetic materials show certain crystallographic directions which are easier to magnetize than others. These directions are the so called easy axes of magnetization and are defined by the magnetic anisotropy. Furthermore, the magnetic anisotropy is the actual origin of hysteresis and coercivity [3]. The magnetocrystalline anisotropy involves the electrostatic crystal-field interaction and relativistic spin-orbit-coupling [3]. Considering defect free bulk materials magnetic properties as the saturation magnetization, coercivity or the Curie temperature depend only on the chemical and crystallographic structure of the material due to the magnetocrystalline anisotropy [4]. The size and shape of these materials are not crucially important.

Nanostructured magnetic materials show a wide range of unusual magnetic properties which are strongly influenced by finite size and surface effects [4]. A lot of these effects are strongly influenced by the effective anisotropy of the material. Due to the reduction of the size the influence of shape- and surface anisotropy increases and can affect the physical properties of the material and the domain structure. By reducing the particle size of a material also the number of domains will reduce. Normally a magnet consists of several domains separated by domain

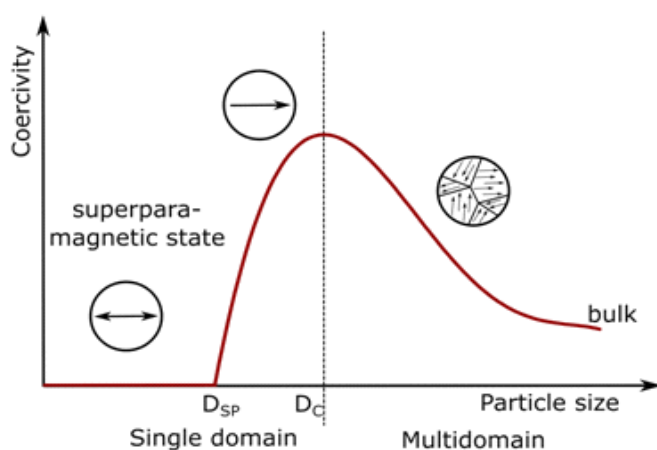


Fig. 2: Illustration of the particle size dependence of the coercivity.

walls. When the particle size is reduced these domains start to rearrange. An example for influence of the domain structure on the macroscopic properties is the behavior of the coercivity in dependence of the particle size (Fig. 2). With a decreasing particle size, the coercivity of immobilized particles increases. A maximum is reached at the certain critical size D_C . This critical size strongly depends on the effective anisotropy of the material investigated. At this size it is energetically unfavorable for

the magnet to build several domains. The magnet is in single domain state. With a further decrease of the particle size the coercivity decreases drastically and reaches zero in the superparamagnetic state [5].

Nanoparticles in a single domain state can be described by assuming that they exhibit an effectively uniaxial anisotropy with only one anisotropy constant, since the particles are so small, that all spins are aligned parallel [3]. The anisotropy energy can be described by:

$$E = K_1 V \sin 2\theta, \quad (3)$$

with K_1 being the first anisotropy constant along an easy axis, V the particle volume and θ the angle between the easy axis of magnetization and the magnetization vector. Eq. (3) shows that the anisotropy energy directly depends on the volume of the particle. When the particle size decreases, the anisotropy energy can reach the same order of magnitude as the thermal energy $k_B T$. Due to this fact flips between the energetic minima of differently oriented easy axes are possible and the nanoparticle behaves like a paramagnetic material. The time scale of such jump can be described by the Néel relaxation time, which is an exponential function:

$$\tau_N = \tau_0 e^{K_1 V / (k_B T)}, \quad (4)$$

with τ_0 being the Néel relaxation constant in the order of 10^{-9} s [6]. It describes the time constant necessary for a particle to relax into an energetic minimum after a perturbation. When the Néel relaxation time of a nanoparticle is in the same order of magnitude as the measurement time, the superparamagnetic effect is observed. This measurement time can be different for different measurement methods and the transition to the superparamagnetic state can be observed for different particle sizes.

3.3 Relaxation behavior und frequency dependent susceptibility

Considering non-immobilized magnetic nanoparticles in suspension two relaxation mechanisms can be observed – Néel and Brown relaxation. The Néel relaxation as described above is a rotation of the magnetic moments within the particles. Brown relaxation is originated by a diffusive rotation of the particles in the liquid [7]. The Brownian relaxation can be described with the Brownian relaxation time τ_B by:

$$\tau_B = \frac{\pi \eta d_h^3}{2 k_B T}, \quad (5)$$

with η being the viscosity of the solution and d_h the hydrodynamic diameter of the particles [7, 8]. It is to be seen that in both cases, for Néel as well as for Brown relaxation, the relaxation time depends on the particle volume. Since both relaxation mechanisms are possible in a particle suspension, an effective relaxation time τ_{eff} as a linear combination of both relaxation processes can be observed [8]

$$\tau_{eff} = \frac{\tau_N \tau_B}{\tau_N + \tau_B} \quad (6)$$

The relaxation behaviour of nanoparticles with different diameters is dominated by different

relaxation mechanisms. When the Néel relaxation time is significantly longer than the Brownian relaxation time, the particles are in the so called blocked state [9].

In Eq. (2) a simple relation between the magnetic field and the magnetization was introduced via the susceptibility. Considering small amplitudes of the external field the susceptibility can be described independent from the external magnetic field [7]. The irreversibility of the hysteresis is taken into account when the susceptibility is described to be complex [7]. Therefore, in an alternating magnetic field the magnetic susceptibility can be described by:

$$M = \chi H = (\chi' - i\chi'')H, \quad (7)$$

where χ' is the real and χ'' the imaginary part of the susceptibility. According to the Debye model the complex susceptibility in dependence on the applied frequency can be described by [10]:

$$\chi(\omega) = \frac{\chi_0}{1 + i\omega\tau_{eff}} \quad (8)$$

However, ensembles of magnetic nanoparticles normally exhibit a distribution of relaxation times due to particle size distribution and are usually described by a log-normal distribution of the effective relaxation time.

References

- [1] Pankhurst, Q.A., et al., *Applications of magnetic nanoparticles in biomedicine*. Journal of physics D: Applied physics, 2003. **36**(13): p. R167.
- [2] Krishnan, K.M., *Fundamentals and applications of magnetic materials*. 2016: Oxford University Press.
- [3] Skomski, R., *Simple models of magnetism*. 2008: Oxford University Press on Demand.
- [4] Gubin, S.P., *Magnetic nanoparticles*. 2009: John Wiley & Sons.
- [5] Bean, C. and J. Livingston, *Superparamagnetism*. Journal of Applied Physics, 1959. **30**(4): p. S120-S129.
- [6] Néel, L., *Influence des fluctuations thermiques sur l'aimantation de grains ferromagnétiques très fins*. Comptes rendus hebdomadaires des séances de l'Académie, 1949. **228**(8): p. 664-666.
- [7] Hergt, R., S. Dutz, and M. Zeisberger, *Validity limits of the Néel relaxation model of magnetic nanoparticles for hyperthermia*. Nanotechnology, 2009. **21**(1): p. 015706.
- [8] Astalan, A.P., et al., *Biomolecular reactions studied using changes in Brownian rotation dynamics of magnetic particles*. Biosensors and Bioelectronics, 2004. **19**(8): p. 945-951.
- [9] Astalan, A.P., et al., *Magnetic response of thermally blocked magnetic nanoparticles in a pulsed magnetic field*. Journal of Magnetism and Magnetic Materials, 2007. **311**(1): p. 166-170.
- [10] Debye, P., *Polar Molecules*. 1945. New York: Dover.

4 Magnetic nano- and microparticles for biosensor applications

Kerstin Witte^{1,2}, Mikkel Fought Hansen³, Cordula Grüttner¹

¹ *micromod Partikeltechnologie GmbH, Friedrich-Barnewitz-Str. 4, 18119 Rostock, Germany*

² *University of Rostock, Institute of Physics, Albert-Einstein-Str. 23, 18059 Rostock, Germany*

³ *Technical University of Denmark, Department of Micro- and Nanotechnology, Kongens Lyngby, Denmark*

4.1 Introduction

Magnetic nanoparticles (MNPs) offer attractive possibilities for application in biomedicine. Living cells are in a size regime of 10 μm . Magnetic nanoparticles however are smaller by up to three orders of magnitude and their size is comparable to the size of analytes to be detected like viruses, proteins or genes [1]. A biosensor is an integrated analytical device that uses a recognition element, generally a biomolecule, to bind an analyte, and a transduction mechanism for the detection of this binding event [2].

Conventional biosensors normally used fluorescent tags to mark biomolecules. This often required heavy and expensive fluorescence detection systems and micro-spotters for detection. Therefore the application of MNPs with their unique properties attracted lots of attention for the development of novel biosensor systems. Over the last decades, magnetic separation and detection technology has emerged as one of the most promising solutions [3]. In this method, colloidal particles are manipulated by mismatches in their magnetization. Additionally, the magnetic force can be used to separate and detect particles with different nonmagnetic properties such as size, shape, density, or the amount of molecules which are attached to their surface [3].

Magnetic biosensors are classically divided into substrate-based and substrate-free biosensors. If the target is present, the probe functionalized MNPs directly bind to the sensor's surface. These sensors are called substrate-based biosensors [4]. In contrast substrate-free sensors make use of the resonance behavior of nanoparticles, where the probe and target hybridization causes a change in the resonance behavior [4]. The sensors are also different in their way of detecting the magnetic particles often called labels, their signal-to-noise ratio, sensor dimensions, types of particles used for the detection, experimental conditions as well as the amplification technique [5].

The product assortment of **micromod** provides different types of magnetic nano- and microparticles that are interesting tools for the development of both biosensor types (Table 1). The superparamagnetic dextran iron oxide composite particles of the nanomag[®]-D and nanomag[®]-D-spio type as well as the magnetic polystyrene microparticles (micromer[®]-M) were widely studied especially as tools in substrate based biosensors. The Bionized NanoFerrite particles BNF-Starch and BNF-Dextran are thermally blocked at room temperature and provide optimal magnetic properties as tools in substrate-free biosensors. Here we present an overview

on recent applications of magnetic nano- and microparticle systems that were provided by **micromod**. After a short introduction in the different biosensors in general, the results obtained with individual MNPs based sensors are discussed. Furthermore the substrate-based biosensor systems are divided by their read-out-systems, and the substrate-free biosensors are divided by properties of the particles, which were used in the sensor.

4.2 Read-out Systems

The biosensors applying MNPs can be divided directly by their general sensor read-out system as well as by the different particle properties used for the read-out. While for substrate-based biosensor systems mainly the bare presence of MNPs with their large magnetic moments is of advantage, the substrate-free biosensors mainly use different unique properties of nanoparticles especially resonance phenomena. An overview of the different read-out systems for biosensors is introduced.

The biorecognition assay normally starts with the introduction of an unknown sample previously specifically labeled with MNPs. This target corresponds to the analyte. If the analyte and target strands are complementary a biomolecular reaction occurs. For most substrate based sensors a washing step removes all other unrecognized targets. This washing step is not necessary for most substrate-free biosensor systems.

The following sections will further introduce specifications of the different sensor types and how the magnetic particles are used to determine the presence of a target.

4.2.1 Magnetoresistive sensors

A change in the resistivity due to a magnetic field is known since the 1860s as a magnetoresistive effect. Nevertheless, the discovery of the antiferromagnetic exchange coupling [6] and the giant magnetoresistive effect [7] led to the technological development for high sensitivity magnetic nanostructures [8]. In ferromagnetic transition metal alloys like FeNi or FeNiCo, the anisotropic magnetoresistive effect can be observed. A change of the alloys resistance occurs when the magnetization changes from parallel to transverse with respect to the direction of current flow. This is the basis for planar Hall sensors and anisotropic magnetoresistance sensors [8]. The basis for giant magnetoresistive sensors and spin-valve sensors is the giant magnetoresistive effect. This effect is based on the spin dependent interfacial and bulk scattering asymmetry in spin-up and -down conduction electrons in ferromagnetic-antiferromagnetic multilayer structures. The application of a magnetic field changes the relative orientation of two magnetic layers leading to a change in the resistance of the layer structure [7].

Magnetoresistive sensors are in general substrate-based. Thus, biochip platforms utilizing magnetoresistive sensors have been used in the last few years for biomolecular detection down to the femtomolar range [9, 10].

magnetic micro- and nanoparticles

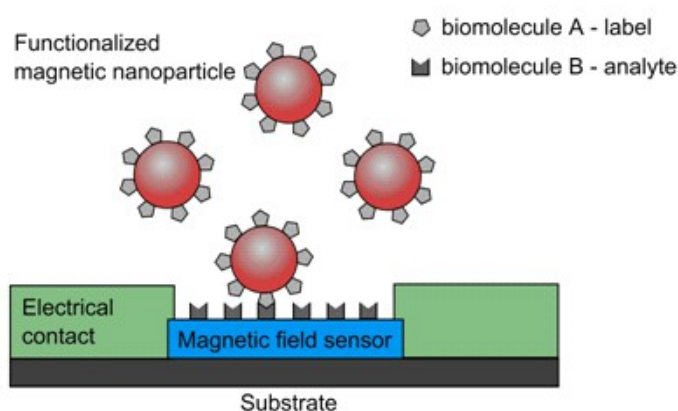


Fig. 1: Illustration of a magnetoresistive biosensor.

The MNPs are magnetized by applying an external magnetic field. The fringe field is created by the immobilized nanoparticles and detected by the magnetoresistive sensors (Figure 1) [8]. The sensor's electrical resistance varies proportional to the number of biomolecular recognition events [9].

4.2.2 Inductive sensors

Inductive sensors are based on the changes of the magnetic permeability of gases, liquids or solid samples placed inside a measuring coil [11]. MNPs in the coils or close to the coils lead to changes in the induced voltage in the sensor. The number of particles is proportional to the induced voltage immobilizing the functionalized nanoparticles in the sensor area [12].

Susceptibility sensors also utilize the detection techniques via induction. The particle's rotational dynamics as a result of binding events are detected instead of the bare presence of the particles. These biosensor types mainly use the Brownian relaxation phenomenon [13, 14]. This describes the physical frequency dependent rotation of MNPs in an external magnetic field. Due to the binding of target molecules onto the functionalized MNPs the hydrodynamic diameter of the particles changes and furthermore clustering can occur. As a consequence the Brownian relaxation time changes as well [13, 15]. The frequency dependent behavior can be determined in a classical AC susceptometer. Two pick-up coils are placed inside an excitation coil. The excitation coil generates a frequency dependent magnetic field which should generate identical voltages in the pick-up coils. Placing a sample in one of the pick-up coils leads to an asymmetric voltage in the coil system enabling the determination of the magnetic susceptibility.

4.2.3 SQUID sensors

Magnetometers based on DC superconducting quantum interference devices (SQUIDs) are the most sensitive devices for measuring weak magnetic fields [16]. They are operating at cryogenic temperatures with quantum-limited sensitivity in the regime of 10^{-17} T [17].

Below a critical temperature the electrical resistivity of certain materials approach zero due to the binding of electrons in weakly bound Cooper pairs [18]. The materials enter the superconducting state. If such a material is exposed to an external magnetic field, it behaves like an ideal diamagnet [19]. Therefore, when a superconducting material forms a ring, a magnetic field inside this ring would stay trapped below the critical temperature. Insertion of a small plate

magnetic micro- and nanoparticles

of a non-superconducting material in the ring enables the measurement of the tunneling current [20]. This so called Josephson effect provides the possibility of measuring small changes in the magnetic field inside a SQUID [17].

4.2.4 Optomagnetic sensors

Optomagnetic sensors allow fast, inexpensive, highly sensitive and also quantitative measurements of the concentration of biomolecular targets in solution by monitoring the light modulation of self-assembled nanoparticles or by their changing rotational behavior [21-24].

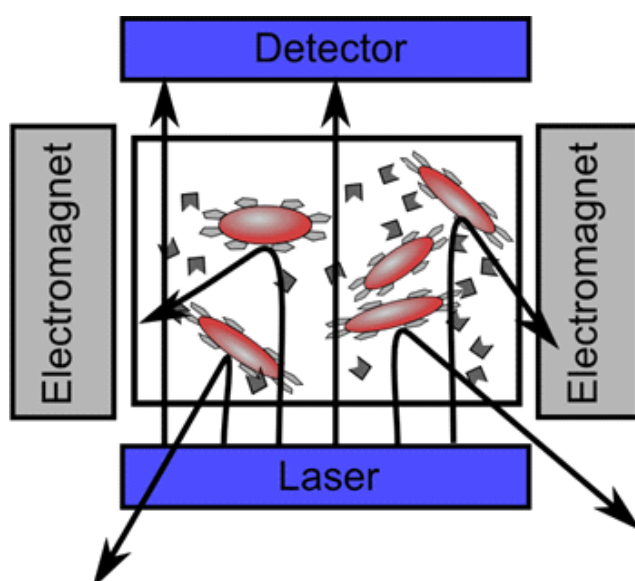


Fig. 2: Optomagnetic biosensor detection scheme

magnetic field is applied with a certain frequency the nanoparticles rotate physically and form chains. When the magnetic field is reversed the particle's chains will break due to thermal agitation and due to magnetic torque on individual particles. The rotation of nanoparticles, which normally do not have a regular shape, and the formation and breaking of chains will lead to modulations of transmitted light which follow the Brownian relaxation dynamics (illustrated in Fig. 2). The binding nanoparticles to an analyte changes the hydrodynamic size of the particles and consequently the Brownian relaxation dynamics [22]. Additional clustering of the particles due to binding to the same target is possible, which will also influence the scattering dynamics [21].

4.2.5 NMR sensors

Sensors based on nuclear magnetic resonance (NMR) are fast compared to other detection techniques due to the fact that they do not require solid-phase immobilization, diffusion of nanoparticles into the sensing element or discrete amplification steps [25].

The principle of NMR relies on the nuclear spin of atoms. Hydrogen atoms are the most important ones due to the largest nuclear spin. If the nuclei are in an external static magnetic field, the spins align parallel or antiparallel to this field. A transition between these two states can be achieved temporally by applying a time varying magnetic field perpendicular to the static field. The frequency of this field is the Larmor frequency and is proportional to the energy gap between the

magnetic micro- and nanoparticles

two energetic states of the nuclei's spins [26, 27]. The perturbation of the nuclear spin causes a change in the net magnetization longitudinal and transversal to the static magnetic field with two different relaxation times T_1 and T_2 respectively [26, 27]. Both relaxation processes are executed independently and simultaneously. The longitudinal relaxation with the relaxation time T_1 mainly depends on the static magnetic field strength. In contrast the transversal relaxation (T_2) results from the magnetic dipole-dipole interactions, diffusion constants of protons and inhomogeneities in the external field [26, 27]. However, the presence of MNPs strongly influence the relaxation time T_2 [26, 27].

NMR sensors are so called proximity sensors which accelerate the relaxation rate of neighboring hydrogen nuclei [25]. Assays employing diagnostic magnetic resonance use affinity-conjugated MNPs which bind to molecular targets and therefore induce a change in the relaxation rate of the hydrogen nuclei. Two different modes can be distinguished. In the first mode large structures such as whole cells are labeled and after the labeling step additional unbound particles are washed out. In the second mode the magnetic relaxation switching is used. The principle of magnetic relaxation switches is represented in Fig. 3 [26]. The targets are used to assemble the MNPs into larger clusters and affect their relaxation rate [25]. For both modes the binding effects are performed in solution. The presence of MNPs in the solution influences the relaxation of the hydrogen nuclei by dipolar coupling of the protons and the magnetic moment of the nanoparticles [28].

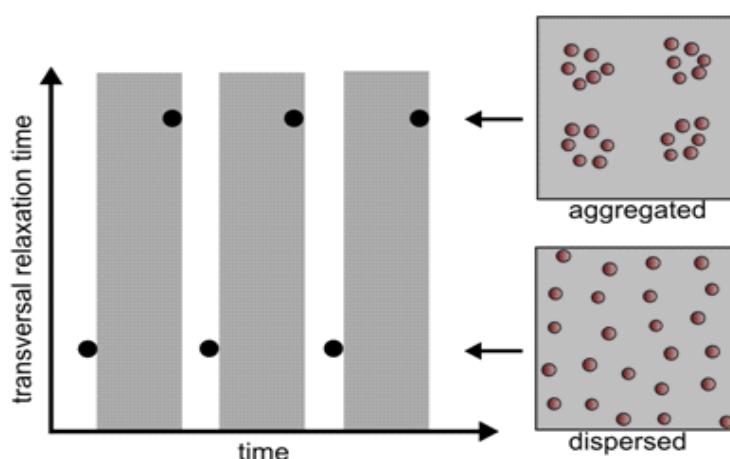


Fig. 3: Principle of magnetic relaxation switches. The grey area in the graph indicates that a homogenous magnetic field is turned on.

4.2.6 Ferromagnetic sensors

The general sensor consists of a microwave circuit built of a slot line and a coplanar waveguide. The active sensor area is the area between the slot line and waveguide which can be functionalized with analyte-specific ligands [29, 30]. The slot line is excited by a microwave signal which generates an AC magnetic field at the sensor area. The generated fields are orthogonal to the coplanar waveguide and therefore also orthogonal to the propagation mode allowed by the waveguide. Thus, no signal is detected. If MNPs are immobilized in the sensor area the field distribution is perturbed [29, 30]. The AC magnetic field from the slotline causes a time varying change in the magnetization of the nanoparticles which are immobilized at the sensor area. Hence, a field component is generated which is favorable for propagation in the coplanar waveguide. Therefore, the input signal is inductively coupled to the output signal, which itself is proportional to the input frequency and enhanced by stimulated ferromagnetic resonance (FMR)

in the MNPs [29]. The FMR frequency is the natural frequency at which the magnetization precesses around an applied field in response to an excitation field. If the applied frequency from the slotline has the frequency of the nanoparticle's ferromagnetic resonance, the time varying components of magnetization are significantly enhanced and the magnetic flux into the waveguide increases [30].

4.2.7 Higher harmonics sensors

Magnetic particle imaging (MPI) is a relatively novel imaging technique using the nonlinear magnetization curve of small MNPs in order to produce high resolution images [31]. The magnetization of particles saturates at certain field strength. If an oscillating magnetic field with a certain frequency and a sufficiently high amplitude is applied, the particle will exhibit a magnetization which contains the driving frequency and a series of higher harmonic frequencies as illustrated in Fig. 4 [31]. The design of nanoparticles for MPI sets requirements in respect to the

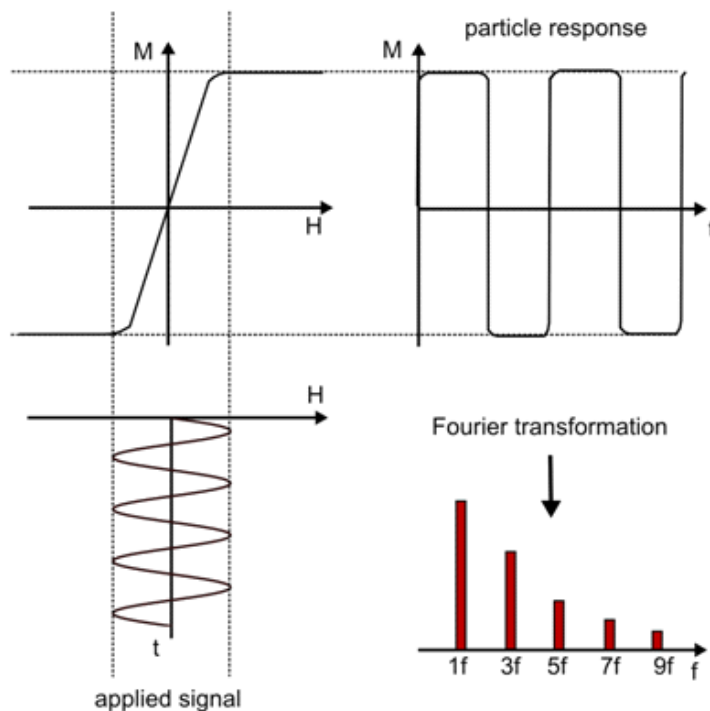


Fig. 4: Schematics of the MPI following the applied signal and the response from the particle.

particle's size, material, shape, and coating which determines the amplitude of the magnetic moment and the relaxation time constant of the particle [32]. Therefore also the dynamics of the nanoparticles can influence the MPI signal. Magnetic spectroscopy of nanoparticle Brownian motion (MSB) is a related technique and can be used to investigate the microscopic environment of the particle including its temperature [33] and the chemical bonding state [34]. The unique spectral signature of different nanoparticle types renders the harmonics based detection of multiple particles possible [35]. The general set-up is quite similar to an AC susceptometer and can consist of a driving coil generating a harmonic applied field. Inside the driving coil the pick-up coil and a balance coil are placed. The pick-up coil contains the sample. This coil and the balancing coil are placed in series that the current generated in the balancing coil cancels the current generated in the pick-up coil leaving only the signal from the nanoparticles which can be further analyzed [33, 35].

particle's size, material, shape, and coating which determines the amplitude of the magnetic moment and the relaxation time constant of the particle [32]. Therefore also the dynamics of the nanoparticles can influence the MPI signal. Magnetic spectroscopy of nanoparticle Brownian motion (MSB) is a related technique and can be used to investigate the microscopic environment of the particle including its temperature [33] and the chemical bonding state [34]. The unique spectral signature of different nanoparticle types renders the harmonics based detection of multiple particles possible [35]. The general set-up is quite similar to an

4.3 Applications of substrate-based biosensor systems

4.3.1 Biosensing principles

On-chip magnetic biosensors rely on magnetic detection of MNPs being developed as compact biosensors with a direct electrical readout. These sensors are sensitive to very small quantities of nanoparticles. The magnetic particle detection systems are usually substrate-based, In this case the particles are attached to a sensor surface by target molecules.

4.3.2 Magnetoresistive sensor systems

Spin valve sensors are in general multilayered metallic nanostructures exhibiting giant magnetoresistance. The structure incorporates free and pinned antiferromagnetically coupled layers. Their application as magnetic field sensors is based on resistance changes which occur in the presence of an applied or local magnetic field as a result of changes in the relative orientation of the two magnetic layers [36]. In this regard, 2 μm micromer[®]-M streptavidin functionalized particles were utilized in single and differential sensor architectures [36]. The particles were attached to the sensor surface by streptavidin-biotin binding. It was described that the system can be used to detect biological binding of small numbers of particles up to single particles [36]. Therefore, it was illustrated that 6 to 20 microspheres of 2 μm micromer[®]-M lead to sensor saturation signals for a small spin-valve sensor [36].

Micromagnetic simulations for the detection of single microparticles for spin valve sensors indicated that single or only few particles in the size of 2 μm like the micromer[®]-M can possibly be used as markers [37].

A spin-valve sensor design was introduced that captures the flux generated by MNPs, remaining insensitive to the magnetic fields applied to magnetize and manipulate the particles by integrating two tapered current lines at both sides of the spin-valve sensor [38]. The current lines tapering is necessary to generate a magnetic gradient on the particles which moves them towards the spin-valve sensor [38]. Nanomag[®]-D particles with a high saturation magnetization and a diameter of approximately 250 nm were used to demonstrate the working principle of the sensor set-up [38]. With this set-up it was possible to detect all particles by guiding them to the sensor area. In addition, information about the movement of particles moving between the current line across the sensor was studied. A precise positioning, transport and detection of single 2 μm micromer[®]-M particles and small amounts of 250 nm nanomag[®]-D nanoparticles on a chip surface was shown [39]. The real time spin-valve response of 250 nm nanomag[®]-D particles with a cystic fibrosis transmembrane conductance regulator-related DNA target was measured when it was hybridized onto a complementary DNA probe [39].

The movement of biomolecules labeled with MNPs was precisely controlled by simple aluminum tapered current lines while the particles were simultaneously detected with spin-valve sensors [40]. The particles tended to move more readily to the narrower section of the line, where the local magnetic field generated was higher. This principle was then used to design various on-chip current line structures. For example horseradish peroxidase and streptavidin were labeled with

400 nm nanomag[®]-D and 2 μm micromer[®]-M particles, respectively. The nanomag[®]-D particles lead to a higher signal nevertheless they tend to agglomerate in an external magnetic field at used concentration. In contrast the micromer[®]-M particles enabled the detection of single particles with a small number of biomolecules attached [40, 41].

On-chip spin-valve sensors with tapered aluminum current lines were used to detect the binding of streptavidin-functionalized superparamagnetic nanoparticles onto sensor's surface-bound biotin [5]. Both micrometer- and nanometer-sized labels were studied. The detection of biomolecular recognition was demonstrated with 2 μm micromer[®]-M and 250 nm nanomag[®]-D particles by biotin-streptavidin binding [5]. micromer[®]-M particles were chosen due to their rather uniform size and shape. In addition, the capability of detecting single particles was demonstrated with these particles [5]. The signal-to noise-ratio for smaller particles was too small for the developed sensor [5].

Various results proved the detection of biomolecular recognition of biotin and streptavidin using 250 nm nanomag[®]-D particles. Despite the fact that these particles are characterized by a smaller moment compared to micromer[®]-M, the binding signal is increased since more particles can bind to the surface [42]. The usage of 100 nm and 50 nm nanomag[®]-D-spio particles led to the conclusion that the usage of the smallest particles required to many particles for this type of sensor [42].

MNPs in combination with giant magnetoresistance biosensors can be applied for direct separation of particles which is desirable for many applications. A microfabricated device was developed for electrically controllable separation of magnetic particles with different magnetophoretic mobilities using 2 μm micromer[®]-M particles with streptavidin on the surface and Dynabeads[®] with a similar diameter [43]. The system is based on four aligned current carrying conductors which are identical in structure but independent in operation [43]. The conductors are working periodically in series generating a traveling magnetic field. By adjusting the switching frequency between the conductors, the velocity of the nanoparticles can be maximized being in good agreement with computational models [43].

An on-chip magnetic bead transport device based on a set of two tapered current conductors was developed and tested using 2 μm micromer[®]-M particles [44]. The device is capable of trapping single magnetic microparticles and guiding them along a defined magnetic track opening the possibility of controlled manipulation of magnetically labeled biomolecules [44]. The technical set-up requires a set of two saw-tooth shaped magnetic field generating current conductors, shifted linearly in phase 180°. For the current conductors with rectangular cross sections, the magnetic field is maximal close to the corners of the cross section and is mainly oriented perpendicular to the edge of the conductor. Since the used micromer[®]-M particles are superparamagnetic, the magnetic moment of the particles will align in the same direction [44]. The derived results are in good agreement with theoretical models.

Domain walls in magnetic nanostrips are a source of strong magnetic field gradients and can be used to transport individual magnetic particles. Thus they are also suitable to transport viable cells which are labeled with MNPs [45]. Different techniques to trap MNPs based on domain wall traps were tested using 130 nm nanomag[®]-D particles on silicon and polydimethylsiloxane substrate to demonstrate the usefulness of this method for lab-on-chip magnetic separation [45].

In order to explore the advantages of magnetic force guided biofunctionalized particles the total force balance of a particle moving parallel to a magnetoresistive chip surface was studied via a computational approach and experimentally validated using 2 μm micromer[®]-M particles with a uniform size distribution [46]. The forces included the magnetic force, the drag force and the surface force leading to an approach that can predict the mobility of a particle. The model was validated with micromer[®]-M particles in water, and a good agreement with the experimental results was obtained [46]. Based on this model, a technique was developed that enhances the magnetic force applied on a particle for a fixed current or enables the usage of a smaller current maintaining the same magnetic force [47]. The derived set-up was experimentally validated using micromer[®]-M particles revealing that the mobility of the particles was enhanced by a factor of 3 by introducing a magnetic layer of $\text{Ni}_{80}\text{Fe}_{20}$ between the planes of SiO_2 on the sensor-chip [47].

A detection system that provides information on the position and time of the magnetic behavior of a single particle was introduced using a spin-valve sensor to detect the stray field of streptavidin coated micromer[®]-M particles [48]. The signal of the particle exhibits a distinct dipolar signature [48]. Furthermore, it was shown, that the particle – substrate distance needs to be optimized leading to a significantly higher peak to peak signal in the derived voltage. This parameter is also important for modeling [48]. The simulation model included the particle-substrate separation distance. The distance was determined by a force balance of the perpendicular force acting on the particles also including the magnetic and electrostatic forces. It was found that the ideal separation distance for particle and substrate is about 1250 nm in the used detection system. This result seems to be an important parameter [48].

A small portable and partially autonomously working biorecognition platform with a high signal to noise ratio was developed with 250 nm nanomag[®]-D nanoparticles using spin-valve and tunnel-junction sensor principles [9]. The biomolecular detection capabilities of the platform was demonstrated by performing a hybridization assay with complementary and non-complementary probes and streptavidin-functionalized 250 nm nanomag[®]-D particles tagged with 20mer single stranded DNA targets to recognize the 16S rDNA from *Escherichia coli* [9]. Superior detection limits of the 250 nm nanomag[®]-D down to 40 fM were reported.

magnetic micro- and nanoparticles

Magnetic particle sensors based on the planar Hall effect in thin films of exchange-biased permalloy have been fabricated and characterized with micromer[®]-M particles possessing a diameter of 2 μm and nanomag[®]-D particles with a diameter of 250 nm (Fig. 5) [49]. The sensor response to an applied magnetic field has been measured without and with coatings. The prepared sensor was based on a permalloy because of the higher anisotropic magnetoresistance compared to pure nickel. This technique is sufficiently sensitive to detect only a few magnetic beads and therefore also biomolecules even if only few are present in the sample [49]. Furthermore it was reported that the sensors are feasible of detecting just a few micromer[®]-M particles [50]. Due to the simple fabrication scheme, the planar Hall sensor can be easily integrated into lab-on-a-chip systems, and the particle detection in the field generated by the sensing current without applying external fields is promising [50].

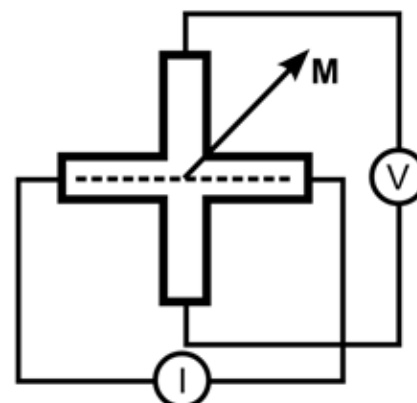


Fig. 5: Illustration of the micro-Hall sensor design.

It was shown that both the hysteresis in the sensor response and the attraction of nanoparticles to the sensor edges can be strongly reduced when a magnetic compensation stack is included under the sensor stack utilizing NH_2 -functionalized 250 nm nanomag[®]-D particles [51]. The addition of a compensation stack below the actual sensor stack nullifies most of the magnetostatic field. Thus the nanoparticles that are attracted to the sensor can only be easily washed off the sensor with a magnetic compensation layer [51].

4.3.3 Inductive sensors

In this case MNPs and a membrane are labeled with distinct antibodies to an analyte. The membrane immobilizes the analyte and the nanoparticles can bind to the analyte as well. The particles are localized and are directly proportional to the amount of analyte present in the membrane. The nanoparticles change the magnetic flux inside a coil due to their magnetization. The change of the voltage in a coil is therefore proportional to the amount of analyte in the tested sample [12].

Streptavidin coated nanomag[®]-D particles with a diameter of 250 nm were used for the quantification of immunochromatographic tests in a sandwich assay with two distinct antibodies directed against human chorionic gonadotropin (hCG) [12]. The first anti-hCG antibody was labeled with the nanoparticles and the second was immobilized as a narrow zone in a membrane. Capillary forces facilitated the migration of the immune complex along the membrane. The amount of nanoparticles that were labeled with the monoclonal anti-hCG bound to the detection zone was directly proportional to the hCG in the detector coil [12].

A differential micro-coil system consists in general of two coil pairs - an excitation coil pair and a sensing coil pair. The excitation coils are planar one-turn micro-coils connected in series to generate a magnetic field to excite MNPs. The sensing coils are reversed coupled multi-turn

planar micro-coils in series. If the system is in balance, induced disturbances due to external forces and excitations from the primary coils are canceled out. In the case that MNPs are in the center of the first sensing coil the system is not in balance anymore. Hence, the induced signal is directly proportional to the number of MNPs [52]. These results led to the development of a micro-coil system using high frequency excitation of MNPs [52]. The sensitivity and the detection limit of such a sensor system were modeled and simulated using the characteristics of 250 nm nanomag[®]-D particles. It was found that single 250 nm nanomag[®]-D particles should be detectable only with a lock-in amplifier [52].

4.3.4 Ferromagnetic resonance sensors

Among others streptavidin coated 250 nm nanomag[®]-D particles were chosen to demonstrate a proof-of-concept experiment of a ferromagnetic resonance sensor with a very high sensitivity for immunosensing applications [29, 53]. The waveguides were patterned in thin-film aluminum thermally evaporated on a glass substrate. The active sensor area was defined using photo-activated patterning of biotin [29, 53].

The magnetic particles were immobilized in the sensor area by streptavidin-biotin binding. A microwave signal operating at frequencies between 2 GHz to 4 GHz was applied to excite resonance in the immobilized particles. The binding of the nanoparticles to biotin on the sensor surface compared to the control was observed due to a distinct sensor output [29, 53].

4.4 Applications of substrate-free biosensor systems

Substrate-free sensor schemes predominantly make use of the resonant behavior of the nanoparticles. The probe and target hybridization causes a change in the particle's resonance behavior.

4.4.1 Susceptibility sensors

An on-chip platform was introduced based on current lines and highly sensitive magnetic tunnel junctions with a superparamagnetic free layer for measuring the Brownian relaxation frequency of NH₂-functionalized nanomag[®]-D particles with a diameter of 250 nm [10]. The particle suspension was excited by an alternating magnetic field that was generated by the current lines close to the sensor area. The measurement of the frequency dependent behavior was determined by the first harmonic of the magnetic tunnel junctions output signal via lock-in detection [10].

The principle of the micro-Hall biosensing relies on the magnetorelaxometry measurements of nanoparticle suspensions using a Hall effect sensor chip embedded in a microfluidic system (Figure 5) [54]. The alternating magnetic field is generated by the sensor bias current and the

complex magnetic susceptibility of the nanoparticles can be recorded as the second harmonic of the sensor response [54].

The magnetorelaxometric behavior of amino-functionalized nanomag[®]-D particles with diameters of 130 nm and 250 nm, respectively, was investigated with a planar Hall effect sensor and demonstrated the effectiveness of this method at ambient conditions [54]. The results of such on-chip relaxometry measurements resemble the results of substrate free SQUID biosensors only with an off-set of the peak [55, 56].

Microscopic magnetic field sensors based on planar Hall effect can be applied for the detection of complex magnetic responses. Here, the self-field bias current is used to generate an excitation field [57]. In this context plain 250 nm nanomag[®]-D particles were investigated in dependence on frequency as well as temperature. It was found that the observations are comparable to the Cole-Cole model for Brownian motion [57]. Nevertheless, the determined hydrodynamic diameter from the on-chip measurements are approximately 25% higher compared to results obtained in the DynoMag[®] susceptometer because interactions between nanoparticles themselves and the sensor surface increase the rotational friction [57].

In vitro quantification of the interaction between human endothelial cells and MNPs with different surface coatings was investigated with a desktop susceptometer [14]. In detail plain nanomag[®]-D particles as well as nanomag[®]-D with COOH, PEG-COOH, PEG 300 and silica C18 surfaces were used to determine the influence of the degree of hydrophilicity and surface charge on the cell uptake [14]. The magnetic susceptibility as a function of the cell concentration was measured leading to the determination of the concentration of MNPs. The real and imaginary part of the magnetic susceptibility were determined at a frequency of 2 kHz and compared to a standard curve in order to link the particle concentration in the cells to the measured magnetic susceptibility [14]. The nanomag[®]-D particles with COOH or PEG-COOH surface groups adhered to the human endothelial cells and were phagocytosed to a considerable degree [14].

The basic principle of Brownian relaxation biosensors relies on the binding of biomolecules on the surface of MNPs. This results in a change of the particle's hydrodynamic diameter and consequently in a change of the Brownian relaxation time (Figure 6) [13, 15]. nanomag[®]-D particles, which are clusters of magnetite single domain crystallites embedded into dextran, characteristic of 130 nm size were used to demonstrate the general principle of the system. Therefore nanomag[®]-D particles were functionalized with protein A and used to specifically bind prostate specific antigen [13].

The volume-amplified MNPs detection assay (VAM-NDA) is based on changes in the Brownian relaxation behavior of MNPs that are linked to biomolecules in four general steps [58]:

1. A target recognition through hybridization to a padlock probe accompanied by ligation of the circular probe target complex (i.e. DNA coil),
2. An enzymatic amplification of the DNA circles by rolling circle amplification (RCA) leading to random-coiled single-stranded DNA structure with a repeating sequence,

magnetic micro- and nanoparticles

3. A magnetic labeling of the DNA-coils by means of adding MNPs exhibiting Brownian relaxation behavior, which are equipped with single-stranded DNA-probes (detection oligonucleotides) complementary to the DNA-coil sequence [59].
4. Immobilization: A fraction of the beads proportional to the DNA-coil concentration will link to the DNA-coils. During this immobilization the beads undergo a dramatic increase in the hydrodynamic diameter that strongly influences their Brownian relaxation frequency [59, 60].

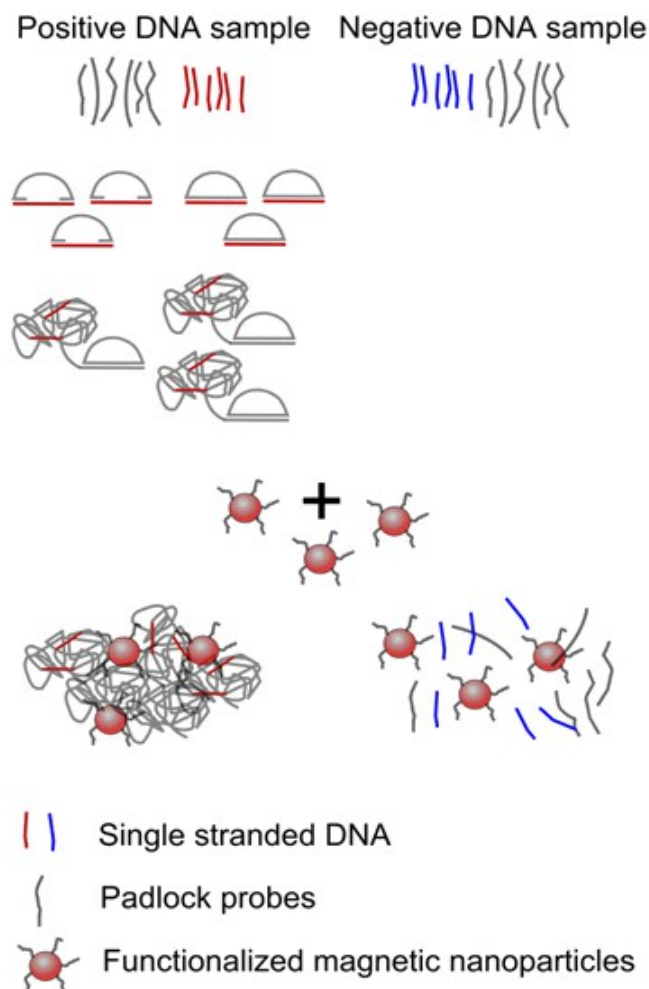


Fig. 6: Schematic illustration of the volume-amplified MNPs detection assay.

A sensitive singleplex detection system of bacterial DNA sequences was reported using a portable AC susceptometer. The detection relied on the MNPs-based bioassay principle [59]. Two types of avidin coated MNPs - 100 nm BNF-Starch and 250 nm nanomag[®]-D - were used and conjugated with varying amounts of biotinylated oligonucleotides. The frequency dependent magnetic volume susceptibility was determined with the portable DynoMag[®] system in the range from 1 Hz up to 250 kHz with an AC field amplitude of 0.5 mT at ambient temperatures [61]. The application of conjugation chemistry (avidin-biotin) on the 100 nm BNF-Starch avidin particles facilitated a more efficient, fast, simple, robust, and stable VAM-NDA system for the detection of bacterial target sequences [59]. The same avidin-functionalized BNF-Starch particles with a

nominal diameter of 100 nm in combination with padlock probes and a DynoMag[®] system were used to develop a method to test rifampicin-resistant mycobacterium tuberculosis [62]. The padlock probes were especially designed to detect mutations in the *rp₀B* gene due to chromosomal mutations.

In a first step amine-functionalized nanomag[®]-D particles with a mean particle diameter of 130 nm were functionalized with oligonucleotides and tested in a superconducting quantum interference device [63]. In this study the excess of oligonucleotides was varied. For low surface coverages, interparticle crosslinking via SS-bridges caused aggregation of the ferrofluid. The interparticle repulsion rises with an increasing surface coverage. It was observed that a surface coverage of approximately 40 oligonucleotides per nanoparticle relates to an optimal behavior of nearly non-interacting particles. Due to the high surface coverage and most likely hydration of oligonucleotide chains, the entropic repulsion effect was decreased leading to a higher crosslinking probability accompanied by a change of the hydrodynamic size of the nanoparticles [63]. Here, it is worth to mention that aging effects create further complications in the nanoparticle systems and have to be taken into account during the surface functionalization [55].

In a second experiment amine-functionalized BNF and nanomag[®]-D particles with different mean diameters of 40 nm, 130 nm and 250 nm were also conjugated with oligonucleotides and tested in a SQUID in the frequency regime from 0.5 to 1000 Hz in order to detect the frequency dependent magnetization [56]. It was shown that the use of small 40 nm nanoparticles enables a turn-off as well as a turn-on detection, while larger nanoparticles only exhibit turn-off detection. In addition, the smaller particles showed fast immobilization kinetics immobilizing larger number of coils. Thus particles of different sizes can be used in multiplex detection strategies [56]. The effects of the particle size variation, particle surface coverage of probe oligonucleotides and the particle concentration itself on the performance of the volume-amplified MNPs detection assay were evaluated [64, 65]. It was found that the detection sensitivity can be improved using smaller amounts of particles [64, 65]. The utilization of 40, 80, 130 and 250 nm BNF and nanomag[®]-D particles, respectively with NH₂ groups on the surface revealed that with rolling circle amplification larger nanoparticles in a polydisperse particle size distribution are easier immobilized in the RCA DNA coils than smaller beads [66].

Amine-functionalized BNF and nanomag[®]-D particles with different mean diameters of 80 nm, 130 nm and 250 nm were further used for the quantitative detection of *Vibrio vulnificus*, *V. cholera* and *Escherichia coli* by SQUID [60]. In general, the possibility of a k-plex detection with the VAM-NDA method utilizing k different kind of MNPs showing Brownian relaxation functionalized with k types of oligonucleotides, respectively [60]. The biblix detection of *V. vulnificus* and *V. cholera* with 250 nm and 130 nm nanomag[®]-D particles was shown in detail exemplifying the usefulness of this method receiving a yes/no answer upon the presence of a target [4, 60].

4.4.2 Optomagnetic sensors

The detection of a *Vibrio cholerae* DNA-sequence was established with avidin-coated 100 nm BNF-Starch and 250 nm nanomag[®]-D particles that were conjugated with biotinylated oligonucleotides via optomagnetical detection using turn-on type read-out [21]. The DNA coils were formed upon a padlock probe ligation followed by rolling circle amplification. It was shown that in the low frequency region a limit of detection of 10 pM can be achieved for an RCA time of 60 min [21]. Streptavidin coated BNF-Starch nanoparticles with a diameter of 100 nm were applied in the detection of bacteria causing urinary tract infections in patient samples with a total assay time of 4h [67]. This assay was also based on padlock probe recognition followed by two cycles of RCA. The optoelectronic devices were low cost devices from blu-ray drives [67]. In addition a detection approach was implemented which relies on the monomerization of the RCA products. Using monomers to link and agglutinate two types of streptavidin coated magnetic particles (Dynabeads MyOne[®] and 100 nm BNF-Starch) functionalized with universal nontarget specific detection probes and introducing a magnetic incubation scheme led to the possibility of multiplex detection of *Escherichia coli*, *Proteus mirabilis* and *Pseudomonas aeruginosa* at clinically relevant concentrations [67]. The results represented an increase in sensitivity by a factor of 30 compared to previously reported detection schemes.

A competitive turn-on immunoassay strategy with two different kinds of magnetic particles (5 μm avidin modified micromer[®]-M and streptavidin modified 100 nm BNF particles) was investigated for *Salmonella* detection with a total assay time of 3 h [68]. In the immunoassay scheme the target bacteria were captured by antibody coated micromer[®]-M to form large immune-magnetic aggregates at certain concentrations. The formed aggregates were incubated with modified 100 nm BNF particles. The unbound particles in the suspension were detected by a blu-ray optomagnetic setup [68]. The competitive strategy was investigated with a direct immunoassay scheme binding the antibody conjugated BNF particles directly to the bacteria. It was found that the competitive strategy is approximately 20 times more sensitive [68]. Furthermore, a homogeneous biphase detection strategy for *Salmonella typhimurium* and *Escherichia coli* was reported binding the *E. coli* bacteria with antibody conjugated 250 nm nanomag[®]-D particles and simultaneously *S. typhimurium* to the biotinylated-antibody coated micromer[®]-M. Thereby immune-magnetic aggregates were formed preventing the binding of the 100 nm streptavidin particles [68].

A biosensing platform for the detection of proteins based on agglutination of aptamer coated magnetic nano- and microparticles was introduced using two ways of the target detection. For optomagnetic read-out nanoparticles were used and for optical imaging microparticles were applied [69]. The particles in this study were streptavidin coated 100 nm BNF and 1 μm Dynabeads. The particles were functionalized with specific aptamers by forming biotin-streptavidin bonds for the agglutination assay for thrombin detection. The aptamers had a specific affinity binding to two structurally opposite sides of the thrombin molecule. The optomagnetic read-out uses the changing dynamics of the BNF nanoparticles and its aggregates. The imaging of the microparticles uses the direct visualization and quantification of

the average size of microparticle aggregates. Identical detection limits of 25 pM were obtained with a short sample-to-answer time [69].

The optomagnetic and AC susceptibility read-out system were compared by their performance using 100 nm BNF particles in an agglutination assay to detect C-reactive protein [70]. Both methods are highly correlated and take advantage of the frequency shift in the dynamic response to an applied time varying magnetic field. In the case of the AC susceptibility method the magnetic response was investigated. In contrast, the optomagnetic method detects the frequency dependent modulation of the optical transmission of laser light [70]. The COOH-labeled 100nm BNF particles being used in this study were functionalized with polyclonal C-reactive protein antibodies. The C-reactive proteins possess multiple binding sites for the antibodies which may result in crosslinking the particles. The measurement and analysis strategies were compared. In all experiments identical samples containing various C-reactive protein concentrations were used [70]. Excellent correlation was found for turn-off detection scheme showing that both methods probe the same Brownian relaxation dynamics. In turn-on and phase-based detection schemes the correlation was less clear because both methods have different sensitivity to the size of agglomerates [70]. The optomagnetic measurement method was superior due to the fast assay time compared to the AC susceptometry and the higher sensitivity [70].

4.4.3 NMR sensors

Amine-functionalized nanomag[®]-CLD-spio particles were used to exploit the primary-secondary antibody binding against specific targets. It was quantitatively shown that a multiplex assay against several targets is feasible using a NMR relaxometer [71].

In addition, a prototype for a biomarker monitoring device based on magnetic relaxation switches was developed with the same nanomag-CLD[®]-spio particles [72]. The implantable sensors were tested *in vivo* in C57BL6 mice inducing acute myocardial infarction. A relaxation time increase in the myocardial infarction group compared to the sham and control group for all three biomarkers used was evident [72]. Such a sensor can provide information on the biomarker levels throughout longer time intervals enabling the possibility to identify previously undetectable infarcts [72].

4.4.4 Higher harmonics sensors

The magnetic moment of a superparamagnetic nanoparticle tries to reach energy equilibrium under the influence of an alternating magnetic field. The magnetization in the static case is well defined and will influence the amplitude of the harmonics and the rate with which the harmonics will decrease with increasing harmonic number. If the frequency increases, the particles cannot reach the equilibrium state anymore and a phase lag can develop between the particle magnetization and the drive field. Therefore, each type of nanoparticle has a unique spectral response [35].

magnetic micro- and nanoparticles

100 nm nanomag[®]-D-spio particles have been used to study the magnetic spectroscopy of Brownian motion in combination with other nanoparticle types [35]. It was found that each particle type has a unique response, which was demonstrated for up to three different particle types. This makes MNPs very interesting for the evaluation of the particle's microscopic environment and the chemical bound state as basis for biosensing applications [35].

4.5 Summary

In the last years the development of MNPs for biosensor applications dramatically increased. The substrate-free as well as the substrate-based biosensor systems utilize MNPs due to their sensitivity, time efficiency, low costs and also the possibility to have a quantitative simultaneous detection of several targets. An overview of magnetic particles produced by **micromod** for the described biosensor schemes is summarized in the following Table. The outstanding magnetic properties and the high diversity of surface functionalizations allow the use of BNF, nanomag[®]-D and micromer[®]-M particles as superior tools in biosensor applications.

Overview of micromod's particles used for different biosensor schemes
(sb – substrate-based, sf – substrate-free).

BNF-Starch

size	coating	sb/sf	detection technique	remarks	references
100nm	avidin	sf	Brownian relaxation	detection of rifampicin-resistant mycobacterium tuberculosis [46]	[45, 46]
	streptavidin	sf	optomagnetic	detection of bacteria causing urinary tract infection by multiplex [49], and biblex sensing [50]	[49] [50]
	avidin	sf	optomagnetic	limit of detection 10 pM [48]	[48]
40 nm	amine	sf	Brownian relaxation	biblex detection of bacterial DNA [38], smaller particles better for turn-on detection [26]	[26, 38, 42-44]
80 nm	amine	sf	Brownian relaxation	multiplex detection [40]	[40, 44]
100 nm		sf	higher harmonics		[47]

nanomag[®]-D-spio

size	coating	sb/sf	detection technique	remarks	references
50 nm	plain	sf	higher harmonics		[47]
50 nm	streptavidin	sb	magnetoresistive		[14]
100 nm	streptavidin	sb	mangetoresistive		[14]

nanomag[®]-CLD-spio

size	coating	sb/sf	detection technique	remarks	references
50 nm	amine	sf	magnetic relaxation switch	possible multiplex assay [33], <i>in vivo</i> in C57BL6 mice inducing acute myocardial infarction [34]	[33, 34]

magnetic micro- and nanoparticles

nanomag®-D

size	coating	sb/sf	detection technique	remarks	references	
130 nm		sb	magnetoresistive		[18]	
		sf	Brownian relaxation		[36]	
	amine	sb	Hall-effect		[22]	
	amine	sf	Brownian relaxation	biblex detection of bacterial DNA [38], smaller particles better for turn-on detection [26], multiplex detection [40]	[26, 38, 40-44]	
250 nm		sb	magnetoresistive	measuring brownian relaxation frequency [7]	[7, 10, 11]	
		sb	Hall-effect	limit of detection 4pM [4]	[4, 23, 27]	
		sf	optomagnetic	biblex detection [50]	[50]	
	streptavidin	sb	magnetoresistive	larger binding signal compared to micromer®- M [14]	[5, 6, 14]	
	streptavidin	sb	sandwich assey		[29]	
	streptavidin	sb	ferromagnetic resonance		[31, 32]	
	avidin	sf	Brownian relaxation		[45]	
	avidin	sf	optomagnetic	limit of detection 10 pM [48]	[48]	
	amine	sb	Hall-effect		[22] [28]	
	amine	sf	Brownian relaxation	biblex detection of bacterial DNA [38] larger particles better for turn-off detection [26], multiplex detection [40]	[26, 38, 40, 42-44]	
	400 nm	horseradish peroxidase	sb	magnetoresistive	high signal, but agglomeration for used concentration	[12, 13]
			sf	magnetic susceptibility	<i>in vitro</i> quantification of human endothelial cells and magnetic nanoparticles	[35]
COOH		sf	magnetic susceptibility	<i>in vitro</i> quantification of human endothelial cells and magnetic nanoparticles	[35]	
PEG-COOH		sf	magnetic susceptibility	<i>in vitro</i> quantification of human endothelial cells and magnetic nanoparticles	[35]	
PEG 300		sf	magnetic susceptibility	<i>in vitro</i> quantification of human endothelial cells and magnetic nanoparticles	[35]	
silica C18		sf	magnetic susceptibility	<i>in vitro</i> quantification of human endothelial cells and magnetic nanoparticles	[35]	

micromer®- M

size	coating	sb/sf	detection technique	remarks	references
2 µm		sb	magnetoresistive	detection of single particles [11],[11, 17, 19, 20] comparison with simulations and optimization [19, 20]	
		sb	Hall-effect		[23, 24]
	streptavidin	sb	magnetoresistive	saturation for 6 to 20 spheres [9],[5, 9, 12, 13, detection of single particles [5], 16, 21] detection of single particles with small numbers of attached biomolecules [12, 13], comparison with simulations [16]	
5 µm	avidin	sf	optomagnetic	biblex detection [50]	[50]

*HRP: horseradish peroxidase

References

- [1] Gubin, S.P., *Magnetic nanoparticles*. 2009: John Wiley & Sons.
- [2] Griffin, G.D. and D.N. Stratis-Cullum, *Biosensors*, in *Encyclopedia of Microbiology (Third Edition)*, M. Schaechter, Editor. 2009, Academic Press: Oxford. p. 88-103.
- [3] Friedman, G. and B. Yellen, *Magnetic separation, manipulation and assembly of solid phase in fluids*. *Current Opinion in Colloid & Interface Science*, 2005. **10**(3-4): p. 158-166.
- [4] Svedlindh, P., et al., *Bionanomagnetism*, in *Nanomagnetism And Spintronics: Fabrication, Materials, Characterization And Applications*, N. Farzad and A. Norgaret, Editors. 2011, World Scientific.
- [5] Ferreira, H., et al., *Biodetection using magnetically labeled biomolecules and arrays of spin valve sensors*. *Journal of Applied Physics*, 2003. **93**(10): p. 7281-7286.
- [6] Grünberg, P., et al., *Layered magnetic structures: evidence for antiferromagnetic coupling of Fe layers across Cr interlayers*. *Physical Review Letters*, 1986. **57**(19): p. 2442.
- [7] Baibich, M.N., et al., *Giant magnetoresistance of (001) Fe/(001) Cr magnetic superlattices*. *Physical review letters*, 1988. **61**(21): p. 2472.
- [8] Graham, D.L., H.A. Ferreira, and P.P. Freitas, *Magnetoresistive-based biosensors and biochips*. *Trends in Biotechnology*, 2004. **22**(9): p. 455-462.
- [9] Germano, J., et al., *A portable and autonomous magnetic detection platform for biosensing*. *Sensors*, 2009. **9**: p. 4119-4137.
- [10]]Donolato, M., et al., *On-chip measurement of the Brownian relaxation frequency of magnetic beads using magnetic tunneling junctions*. *Applied Physics Letters*, 2011. **98**(7): p. 073702.
- [11] Baglio, S., S. Castorina, and N. Savalli, *Integrated inductive sensors for the detection of magnetic microparticles*. *IEEE Sensors Journal*, 2005. **5**(3): p. 372-384.
- [12] Laitinen, M.P.A., et al., *Method and apparatus using selected superparamagnetic labels for rapid quantification of immunochromatographic tests*. *Nanotechnology, Science and Applications*, 2009. **2**: p. 13-20.
- [13] Astalan, A.P., et al., *Biomolecular reactions studied using changes in Brownian rotation dynamics of magnetic particles*. *Biosensors and Bioelectronics*, 2004. **19**(8): p. 945-951.
- [14] Ström, V., et al., *A novel and rapid method for quantification of magnetic nanoparticle-cell Interactions using a desktop susceptometer*. *Nanotechnology*, 2004. **15**(5): p. 457.
- [15] Connolly, J. and T.G. St Pierre, *Proposed biosensors based on time-dependent properties of magnetic fluids*. *Journal of Magnetism and Magnetic Materials*, 2001. **225**(1): p. 156-160.
- [16] Kotitz, R., et al., *SQUID based remanence measurements for immunoassays*. *IEEE transactions on applied superconductivity*, 1997. **7**(2): p. 3678-3681

- [17] Fagaly, R., *Superconducting quantum interference device instruments and applications*. Review of scientific instruments, 2006. **77**(10): p. 101101.
- [18] Bardeen, J., L.N. Cooper, and J.R. Schrieffer, *Theory of superconductivity*. Physical Review, 1957. **108**(5): p. 1175.
- [19] Meissner, W. and R. Ochsenfeld, *Ein neuer effekt bei eintritt der supraleitfähigkeit*. Naturwissenschaften, 1933. **21**(44): p. 787-788.
- [20] Josephson, B.D., *Possible new effects in superconductive tunnelling*. Physics letters, 1962. **1**(7): p. 251-253.
- [21] Bejhed, R.S., et al., *Turn-on optomagnetic bacterial DNA sequence detection using volume-amplified magnetic nanobeads*. Biosensors and Bioelectronics, 2015. **66**: p. 405-411.
- [22] Ranzoni, A., et al., *Frequency-selective rotation of two-particle nanoactuators for rapid and sensitive detection of biomolecules*. Nano letters, 2011. **11**(5): p. 2017-2022.
- [23] Park, S.Y., H. Handa, and A. Sandhu, *Magneto-optical biosensing platform based on light scattering from self-assembled chains of functionalized rotating magnetic beads*. Nano letters, 2009. **10**(2): p. 446-451.
- [24] Baudry, J., et al., *Acceleration of the recognition rate between grafted ligands and receptors with magnetic forces*. Proceedings of the National Academy of Sciences, 2006. **103**(44): p. 16076-16078.
- [25] Haun, J.B., et al., *Magnetic nanoparticle biosensors*. Wiley Interdiscip Rev Nanomed Nanobiotechnol, 2010. **2**(3): p. 291-304.
- [26] Rümenapp, C., B. Gleich, and A. Haase, *Magnetic nanoparticles in magnetic resonance imaging and diagnostics*. Pharmaceutical research, 2012. **29**(5): p. 1165-1179.
- [27] Prasad, P.V., *Magnetic resonance imaging: methods and biologic applications*. 2006: Springer Science & Business Media.
- [28] Gossuin, Y., et al., *Magnetic resonance relaxation properties of superparamagnetic particles*. Wiley Interdisciplinary Reviews: Nanomedicine and Nanobiotechnology, 2009. **1**(3): p. 299-310.
- [29] Chatterjee, E., et al., *A microfluidic sensor based on ferromagnetic resonance induced in magnetic bead labels*. Sensors and Actuators B, 2011: p. doi:10.1016/j.snb.2011.02.012.
- [30] Ghionea, S., P. Dhagat, and A. Jander, *Ferromagnetic resonance detection for magnetic microbead sensors*. IEEE Sensors Journal, 2008. **8**(6): p. 896-902.
- [31] Gleich, B. and J. Weizenecker, *Tomographic imaging using the nonlinear response of magnetic particles*. Nature, 2005. **435**(7046): p. 1214-1217.

- [32] Rauwerdink, A.M. and J.B. Weaver, *Harmonic phase angle as a concentration-independent measure of nanoparticle dynamics*. Medical physics, 2010. **37**(6): p. 2587-2592.
- [33] Weaver, J.B., A.M. Rauwerdink, and E.W. Hansen, *Magnetic nanoparticle temperature estimation*. Medical physics, 2009. **36**(5): p. 1822-1829.
- [34] Rauwerdink, A.M. and J.B. Weaver, *Measurement of molecular binding using the Brownian motion of magnetic nanoparticle probes*. Applied Physics Letters, 2010. **96**(3): p. 033702.
- [35] Rauwerdink, A.M., A.J. Giustini, and J.B. Weaver, *Simultaneous quantification of multiple magnetic nanoparticle*. Nanotechnology, 2010. **21**: p. 455101.
- [36] Graham, D.L., et al., *High sensitivity detection of molecular recognition using magnetically labelled biomolecules and magnetoresistive sensors*. Biosensors and Bioelectronics, 2003. **18**(4): p. 483-488.
- [37] Liu, Y., et al., *Micromagnetic simulation for detection of a single magnetic microbead or nanobead by spin-valve sensors*. Journal of applied physics, 2006. **99**(8): p. 08G102.
- [38] Lagae, L., et al., *On-chip manipulation and magnetization assessment of magnetic bead ensembles by integrated spin-valve sensors*. Journal of Applied Physics, 2002. **91**(10): p. 7445-7447.
- [39] Lagae, L., et al., *Magnetic biosensors for genetic screening of cystic fibrosis*. IEE Proceedings-Circuits, Devices and Systems, 2005. **152**(4): p. 393-400.
- [40] Graham, D., et al., *Single magnetic microsphere placement and detection on-chip using current line designs with integrated spin valve sensors: Biotechnological applications*. Journal of Applied Physics, 2002. **91**(10): p. 7786-7788.
- [41] Graham, D.L., et al., *Detection of biomolecular recognition using magnetoresistive sensors*. Biosensors 2002, 2002: p. P3-6.33.
- [42] Ferreira, H.A., et al., *Detection of biomolecular recognition using nanometer-sized magnetic labels and spin-valve sensors*. Magnetism Conference, INTERMAG 2003, IEEE Int., 2003: p. EC-04.
- [43] Liu, C., et al., *On-chip separation of magnetic particles with different magnetophoretic mobilities*. Journal of applied physics, 2007. **101**(2): p. 024913.
- [441] Wirix-Speetjens, R. and J. De Boeck, *On-chip magnetic particle transport by alternating magnetic field gradients*. Magnetism, IEEE Transactions on, 2004. **40**(4): p. 1944-1946.
- [45] Donolato, M., et al., *Characterization of domain wall-based traps for magnetic beads separation*. Journal of Applied Physics, 2012. **111**(7): p. 07B336.
- [46] Wirix-Speetjens, R., et al., *A force study of on-chip magnetic particle transport based on tapered conductors*. IEEE Transactions on Magnetism, 2005. **41**(10): p. 4128-4133.

- [47] Wirix-Speetjens, R., et al., *Enhanced magnetic particle transport by integration of a magnetic flux guide: Experimental verification of simulated behavior*. Journal of applied physics, 2006. **99**(8): p. 08P101.
- [48] Wirix-Speetjens, R., et al., *Single magnetic particle detection: Experimental verification of simulated behavior*. Journal of applied physics, 2006. **99**(10): p. 103903.
- [49] Ejsing, L., et al., *Planar Hall effect sensor for magnetic micro-and nanobead detection*. Applied Physics Letters, 2004. **84**(23): p. 4729-4731.
- [50] Ejsing, L., et al., *Magnetic microbead detection using the planar Hall effect*. Journal of Magnetism and Magnetic Materials, 2005. **293**(1): p. 677-684.
- [51] Dalslet, B.T., M. Donolato, and M.F. Hansen, *Planar Hall effect sensor with magnetostatic compensation layer*. Sensors and Actuators A: Physical, 2012. **174**: p. 1-8.
- [52] Makiranta, J.J. and J.O. Lekkala. *Modeling and simulation of magnetic nanoparticle sensor*. in *Engineering in Medicine and Biology Society, 2005. IEEE-EMBS 2005. 27th Annual International Conference of the*. 2005. IEEE.
- [53] Chatterjee, E., *Detection techniques for biomolecules using semi-conductor nanocrystals and magnetic beads as labels*. 2011.
- [54] Dalslet, B.T., et al., *Bead magnetorelaxometry with an on-chip magnetoresistive sensor*. Lab Chip, 2011. **11**: p. 296-302.
- [55] Strömberg, M., et al., *Aging phenomena in ferrofluids suitable for magnetic biosensor applications*. Journal of applied physics, 2007. **101**(2): p. 023911.
- [56] Strömberg, M., et al., *Microscopic mechanisms influencing the volume amplified magnetic nanobead detection assay*. Biosensors and Bioelectronics, 2008. **24**: p. 696-703.
- [57] Osterberg, F.W., et al., *Chip-based measurements of brownian relaxation of magnetic beads using a planar hall effect magnetic field sensor*. AIP Conf. Proc., 2012. **1311**: p. 176-183.
- [58] Strömberg, M., et al., *Sensitive molecular diagnostics using volume-amplified magnetic nanobeads*. Nano letters, 2008. **8**(3): p. 816-821.
- [59] Strömberg, M., et al., *A magnetic nanobead-based bioassay provides sensitive detection of single-and bplex bacterial DNA using a portable AC susceptometer*. Biotechnology journal, 2014. **9**(1): p. 137-145.
- [60] Strömberg, M., et al., *Multiplex detection of DNA sequences using the volume-amplified magnetic nanobead detection assay*. ANALYTICAL CHEMISTRY, 2009. **81**: p. 3398-3406.
- [61] Ahrentorp, F., et al. *Sensitive high frequency AC susceptometry in magnetic nanoparticle applications*. in *Aip Conference Proceedings*. 2010.
- [62] Engström, A., et al., *Detection of rifampicin resistance in Mycobacterium tuberculosis by padlock probes and magnetic nanobead-based readout*. PloS one, 2013. **8**(4): p. e62015.

- [63] Strömberg, M., et al., *Interbead interactions within oligonucleotide functionalized ferrofluids suitable for magnetic biosensor applications*. Journal of Physics D: Applied Physics, 2007. **40**(5): p. 1320.
- [64] Zardán Gómez de la Torre, T., et al. *Molecular diagnostics using magnetic nanobeads*. in *Journal of Physics: Conference Series*. 2010. IOP Publishing.
- [65] Zardán Gómez de la Torre, T., *Detection of Biomolecules Using Volume-Amplified Magnetic Nanobeads*. 2012.
- [66] Zardan Gomez de la Torre, T., et al., *Investigation of immobilization of functionalized magnetic nanobeads in rolling circle amplified DNA coils*. J. Phys. Chem. B, 2010. **114**: p. 3707-3713.
- [67] Mezger, A., et al., *Scalable DNA-Based Magnetic Nanoparticle Agglutination Assay for Bacterial Detection in Patient Samples*. ACS nano, 2015. **9**(7): p. 7374-7382.
- [68] Tian, B., et al., *Blu-ray optomagnetic measurement based competitive immunoassay for Salmonella detection*. Biosensors and Bioelectronics, 2016. **77**: p. 32-39.
- [69] Uddin, R., et al., *Lab-on-a-disc agglutination assay for protein detection by optomagnetic readout and optical imaging using nano-and micro-sized magnetic beads*. Biosensors and Bioelectronics, 2016. **85**: p. 351-357.
- [70] Fock, J., et al., *Comparison of optomagnetic and AC susceptibility readouts in a magnetic nanoparticle agglutination assay for detection of C-reactive protein*. Biosensors and Bioelectronics, 2016.
- [71] Ling, Y., C.C. Vassiliou, and M.J. Cima, *Magnetic relaxation-based platform for multiplexed assays*. Analyst, 2010. **135**: p. 2360-2364.
- [72] Ling, Y., et al., *Implantable magnetic relaxation sensors measure cumulative exposure to cardiac biomarkers*. Nature biotechnology, 2011. **29**(3): p. 273-277.

5 Magnetic nanoparticles as contrast agents in Magnetic Resonance Imaging (MRI)

Kerstin Witte^{1,2}, Cordula Grüttner²

¹ University of Rostock, Institute of Physics, Albert-Einstein-Str. 23, 18059 Rostock, Germany

² micromod Partikeltechnologie GmbH, Friedrich-Barnewitz-Str. 4, 18119 Rostock, Germany

5.1 Introduction

The magnetic resonance imaging (MRI) is based on the principle of nuclear magnetic resonance. Certain nuclei possess magnetic moments. In the presence of a magnetic field the magnetic moments undergo precession [1]. The frequency at which the nuclei precess about the magnetic field is known as the Larmor frequency ω_L with:

$$\omega_L = \gamma B_0, \quad (1)$$

with B_0 being the magnetic field strength and γ being the gyromagnetic ratio. The most important nuclei for magnetic resonance imaging is hydrogen due to the large number in biological tissue [1, 2]. The gyromagnetic ratio for pure hydrogen is $\gamma/2\pi = 42.58$ MHz/T [1].

The net magnetic field a nucleus experiences is a sum not only of the external magnetic fields but also of the field which is generated by electrons surrounding the nucleus. This results in slight shifts of the Larmor frequency of the nucleus and is characteristic for the molecular groups [1]. Therefore by analyzing the different Larmor frequency also different types of tissue can be identified.

A net magnetic field of the oscillating nuclei can be generated by a resonant radio frequency excitation and also be detected by a radio frequency receiver coil [1]. The applied resonant radio frequency excitation is in general a time-varying magnetic field in a plane perpendicular to B_0 leading to a torque of the nuclei [1, 2]. In practice the excitation signal is applied in a pulse a pulse sequence with a duration which is sufficient to obtain a coherent response [2]. However the signal will not persist because of inter-nuclear and inter-molecular forces which will lead to a loss of phase coherence [1]. The precession of the magnetic moment can be described by Bloch equations. The longitudinal relaxation of the magnetization can be described by:

$$M_{||}(t) = M_0 + (M_{||}(0) - M_0)e^{-t/T_1}, \quad (2)$$

with $M_{||}$ being the longitudinal magnetization, t being the time and T_1 being the longitudinal relaxation time [1]. The longitudinal relaxation time or also spin-lattice relaxation time describes a loss of energy from the system to the surrounding and is related to the dipolar coupling of the nuclei's magnetic moment to its surrounding [2].

The transversal relaxation of the magnetization depends on the phase coherency among the nuclei and can be described by:

$$M_{\perp}(t) = M_{\perp}(0)e^{-t/T_2^{(*)}}, \quad (3)$$

With M_{\perp} being the transverse magnetization and t being the time [1]. Here two different relaxation times for the transverse relaxation can be distinguished T_2 and T_2^* . As Eq. (3) shows the transverse relaxation describes the loss of coherence among the nuclei and a decay of the signal [1]. In magnetic resonance imaging both offer alternative types of signal contrast among tissues. Spin-echo acquisition provided by T_2 weighting and free induction decay (FID) by T_2^* weighting [1]. The transverse relaxation time T_2 is relatively fast compared to the longitudinal relaxation time and describes the dephasing of the nuclei due to intrinsic factors such as molecular size and tissue type [1]. The dephasing of the nuclei as a result of magnetic field inhomogeneities furthermore is described by T_2^* [1, 2]. T_2 and T_2^* are related to one another by:

$$\frac{1}{T_2^*} = \frac{1}{T_2} + \gamma \frac{\Delta B_0}{2}, \quad (4)$$

with ΔB_0 being the variation of the magnetic field [2].

The images are generated by spatially encoding a nuclear magnetic resonance signal from nuclei present in an object, applying a time varying linear magnetic field gradient. A high resolution and the ability to distinguish soft tissues are the main advantages of the magnetic resonance imaging. In some cases the contrast between different tissues is not sufficient and additional contrast agents are required to achieve sufficient contrast in the magnetic resonance image. Compared to conventional contrast agents, nanoparticle-based contrast agents offer enhanced cellular internalisation and slower clearance from tumors [2]. Furthermore conventional contrast agent can lead to severe adverse effects [3].

The function of the magnetic nanoparticles (MNPs) as agents for contrast enhancement in magnetic resonance imaging can be explained considering the relaxation mechanism in hydrogen nuclei in the presence of the magnetic nanoparticles. The nanoparticles show a strong T_1 relaxation. They also introduce strong inhomogeneities in the local magnetic field due to their high susceptibility, which also reduces the relaxation time T_2^* . Depending on the size of the nanoparticles, a strong influence of the T_1 or T_2 relaxation time can be observed. Smaller magnetic nanoparticles rather tend to shorten the relaxation time T_1 , while bigger ones shorten relaxation time T_2 , which results in dark areas in magnetic resonance images [4].

Among the broad variety of MNPs in the product assortment of **micromod** the particle types nanomag®-D-sprio, nanomag®-CLD-sprio, perimag® and BNF provide excellent properties as contrast agent for MRI. Here we provide a short review on third party papers on the application of these particle types for MR imaging in biomedicine and environmental systems. Targeted applications of MNPs for MRI are summarized in chapter 8.

5.2 MR imaging for diagnosis and therapy

5.2.1 Evaluation of the optimal dose of MRI contrast agent

Signal intensity of MR images significantly depends on the concentration of nanoparticles. For clinical studies it is important to find the minimum concentration of iron oxide nanoparticles that produces maximum signal intensity and determines the minimum injection dose. Saharkiz et al. analysed the relationship between the concentration of 20 nm carboxylated nanomag®-D-spio particles and signal intensity using inversion recovery sequence in T1-weighted MR images. The results indicate that the signal intensity is dependent on the concentration of nanoparticles and the inversion time. In addition, the signal intensity increased by increasing the inversion time from 200 to 400 ms for all studied concentrations. The linear relationship between the nanoparticle concentrations and the signal intensity was seen up to 77 $\mu\text{mol Fe/L}$ in 400 ms for long inversion time and 240 $\mu\text{mol Fe/L}$ in 200 ms for short inversion time. The inversion time is an important parameter to consider the relationship between signal intensity and nanoparticle concentrations. An increase in inversion time leads to a decrease in the range of linearity [5]. Furthermore the influence of the coating thickness of nanomag®-D-spio particles with different sizes and polyethylene glycol (PEG) modifications on their relaxivity in MRI was studied. Increments in coating thickness have more influence on relaxivities than differences in the core size of the nanoparticles [6].

5.2.2 Relaxivity measurements for lymphography application

In vitro and *in vivo* investigations in a rat model were performed by Firouznia et al. to investigate the relaxation times T₁, T₂ and T₂^{*} using 20 nm nanomag®-D-spio particles [7]. The relaxation properties of hydrogen nuclei in the presence of the particles at different doses were measured using spin echo and gradient echo imaging protocols. Four different doses of 0.0650 mg/ml, 0.0325 mg/ml, 0.0162 mg/ml and 0.0081 mg/ml particles were used. It was shown that the higher the dose was chosen also all relaxivities increased linearly. Based on these results an optimal protocol was developed for the *in vivo* studies of lymph nodes in rats. Accumulation of particles in the lymph nodes was observed in T₁, T₂ and T₂^{*} images 4 h after the injection [7].

5.2.3 Cell labelling for MRI tracking

Labelling of cells with MNPs holds promise for monitoring the temporal and spatial migration of stem cells into tissues. It is therefore possible to improve the development of cell tracking strategies for the repair or regeneration of tissues and other cell therapies. Human hematopoietic progenitor cells were labelled with various MRI contrast agents to obtain 1.5 T MR images. Daldrop-Link et al. investigated the amount of different types of magnetic particle based contrast agents and found a maximal internalisation for transferrin conjugated 50 nm nanomag®-CLD-spio particles, followed by ferumoxide, and ferumoxtran. Cell viability and proliferation were not significantly impaired after 7 days of exposure to any MR contrast agent [8].

The feasibility of intranasal administration of neural stem/progenitor cells (NSPCs) was investigated as an alternative, noninvasive, and direct passage for the delivery of stem cells to target malignant gliomas. Tumor-targeting and migratory pathways of murine and human NSPCs were investigated by intravital MRI and in histological time course analyses in different glioblastoma models. Reitz et al. have labelled the NSPCs with nanomag®-D-spio particles for MR imaging. Intranasally administered NSPCs displayed a rapid, targeted tumor tropism with significant numbers of NSPCs accumulating specifically at the intracerebral glioma site within 6 hours after intranasal delivery. This directional distribution of cells accumulating intra- and peritumorally makes the intranasal delivery of NSPCs a promising noninvasive and convenient alternative delivery method for the treatment of malignant gliomas with the possibility of multiple dosing regimens [9].

The influence of protamine sulfate on the labelling efficiency, long-term viability and the iron content stability of mammalian cells that were labelled with 20 nm nanomag®-D-spio particles was studied by *in vitro* MRI measurements over 3 weeks. The labelling efficiency when using protamine sulfate as transfection agent for magnetic cell labelling increased the particle uptake and allowed the cell tracing for a longer duration [10].

Wabler et al. studied the influence of cellular iron content on the MRI contrast of magnetic nanoparticles that were originally developed for hyperthermia treatment of cancer. Human prostate carcinoma DU-145 cells were loaded among other particle types with 100 nm BNF-Starch and 100 nm nanomag®-D-spio at a target concentration of 50pg Fe/cell using poly-D-lysine transfection reagent. T_2 -weighted MRI of serial dilutions of these labelled cells was performed at 9.4T and iron content quantification was performed using ICP-MS. For the range of nanoparticle concentrations internalized by cancer cells the signal intensity of T_2 -weighted MRI correlates closely with absolute iron concentration associated with the cells. This correlation may benefit applications for cell-based cancer diagnostic by MRI and hyperthermia therapy [11].

Cell penetrating peptides (CPPs) have been widely used to increase the cellular uptake of nanoparticles. Cavalli et al. have functionalized nanomag®-CLD-spio particles with surface benzaldehyde groups for conjugation of a γ -amino-proline-derived peptide. This new peptide-particle conjugate was found to have a remarkably higher cell penetrating capability in comparison to established TAT-peptide functionalized MNPs. The high level of uptake into HeLa cells was demonstrated by MRI studies to provide a decrease in the T_2 of labelled cells [12].

5.2.4 Noninvasive MRI of an asthma biomarker in the lung using PEG-functionalized MNPs

Asthma is a complex and chronic pulmonary disease characterized by airway hyper-responsiveness and inflammation, as well as underlying structural changes to the airways. Al Faraj et al. present a promising therapeutic approach to give the additional relief required for asthma patients. IL4 and IL13 were simultaneously inhibited via the common receptor chain IL4Ra to block adequately their biologic effects.

Nanomag®-CLD-spio were conjugated with anti-IL4R α blocking antibodies via polyethylene glycol (PEG) polymers of different lengths. The delivery of these blocking antibodies to the inflammatory sites in the lung via the developed nanocarriers was assessed using noninvasive free-breathing pulmonary MRI. The anti-IL4R α -conjugated nanocarriers have been confirmed to be efficient in targeting key inflammatory cells during chronic lung inflammation following intrapulmonary administration in the lung of ovalbumin-challenged asthmatic mice [13]. In another approach the targeting of MNPs to the lung after intravenous administration of BNF-Starch particles should be increased. To achieve a higher pulmonary delivery, high-energy flexible magnets were optimized and externally applied to a specific region of mouse lung. A free-breathing MRI protocol was then optimized to allow noninvasive monitoring [14].

5.2.5 MRI detection of protease producing tumor derived cells by proteolytic actuation of nanoparticle self-assembly

Inspired by the idea of initiating assembly by enzymatic removal of inhibitors, Harris et al. demonstrated with peptide-polymer chemistry that inorganic nanoparticles may be functionalized to exist in a “latent” state until triggered by a protease to self-assemble. The binding of biotin and neutravidin coated 50 nm nanomag®-D-spio particles was inhibited with polyethylene glycol (PEG) polymers that may be proteolytically removed to initiate assembly by matrix metalloproteinase-2 (MMP-2), a protease correlated with cancer invasion, angiogenesis and metastasis. MMP-2 initiated assembly amplifies the transverse (T₂) relaxation of nanoparticle suspensions in MRI, enables magnetic manipulation with external fields, and allows MRI detection of tumor-derived cells that produce the protease. This general approach may enable site-selective immobilization and enhanced image contrast in regions of tumor invasion *in vivo* [15].

5.3 MR imaging of MNPs in environmental systems

In biofilm research, the investigation of the biofilms’ physical structure is of high relevance for the understanding of mass transport processes. However, commonly used imaging techniques for biofilm imaging such as confocal laser scanning microscopy or electron microscopy rarely visualize the *real* biofilm due to their invasiveness and destructiveness. MRI represents the ideal tool to image the biofilm *in situ*, *non-invasively* and *non-destructively* with a spatial resolution of several 10 μ m. To gain specific structural and functional information, a variety of MRI contrast agents different types of MNPs were studied. Thereby the particle type (nanomag®-D-spio and BNF), the size (20 nm and 80 nm), the matrix material (dextran or starch) and the surface functionalities of the MNPs (plain, COOH, NH₂) were varied. Results elucidate the interactions between the biofilms’ surface and the contrast agents and open a new field for biotechnological applications by functional contrast enhancement [16].

The widespread application of MNPs in biomedicine might result in their release into the environment, where their fate will notably depend on their stability and on their transport behaviour in soil and aquatic systems. The successful application of MNPs for groundwater remediation also significantly depends on their mobility after the injection. Cuny et al. investigated the mobility of various MNPs in water-saturated porous media. Laboratory-scale transport experiments were conducted using columns packed with quartz sand as model solid phase. The same set of nanomag®-D-spio and BNF particles as in [16] was selected to study the influence of primary particle size and surface functionalization on particle mobility. MRI provided detailed spatially resolved information complementary to the quantitative detection of the particle breakthrough curves. The approach can be transferred to other porous systems and contributes to a better understanding of particle transport in environmental porous media and porous media in technical applications [17].

References

- [1] Prasad, P.V., *Magnetic resonance imaging: methods and biologic applications*. 2006: Springer Science & Business Media.
- [2] Pankhurst, Q.A., et al., *Applications of magnetic nanoparticles in biomedicine*. Journal of physics D: Applied physics, 2003. **36**(13): p. R167.
- [3] Colombo, M., et al., *Biological applications of magnetic nanoparticles*. Chem Soc Rev, 2012. **41**(11): p. 4306-34.
- [4] Geraldes, C.F. and S. Laurent, *Classification and basic properties of contrast agents for magnetic resonance imaging*. Contrast media & molecular imaging, 2009. **4**(1): p. 1-23.
- [5] Saharkhiz, H., et al., *The effect of inversion time on the relationship between iron oxide nanoparticles concentration and signal intensity in T1-weighted MR images*. Iranian Journal of Radiology, 2014. **11**(2).
- [6] Hajesmaeelzadeh, F., et al., *Effect of coating thickness of iron oxide nanoparticles on their relaxivity in the MRI*. Iranian Journal of Basic Medical Sciences, 2016. **19**(2): p. 166-171.
- [7] Firouznia, K., et al., *MR relaxivity measurement of iron oxide nano-particles for MR lymphography applications*. Pakistan Journal of Biological Sciences: PJBS, 2008. **11**(4): p. 607-612.
- [8] Daldrop-Link, H.E., et al., *Targeting of Hematopoietic Progenitor Cells with MR Contrast Agents 1*. Radiology, 2003. **228**(3): p. 760-767.
- [9] Reitz, M., et al., *Intranasal delivery of neural stem/progenitor cells: a noninvasive passage to target intracerebral glioma*. Stem cells translational medicine, 2012. **1**(12): p. 866-873.
- [10] Shanehsazzadeh, S., et al., *Evaluating the effect of ultrasmall superparamagnetic iron oxide nanoparticles for a long-term magnetic cell labeling*. Journal of Medical Physics, 2013. **38**(1): p. 34-40.

- [11] Wabler, M., et al., *Magnetic resonance imaging contrast of iron oxide nanoparticles developed for hyperthermia is dominated by iron content*. International Journal of Hyperthermia, 2014. **30**(3): p. 192-200.
- [12] Cavalli, S., et al., *Efficient gamma-amino-proline-derived cell penetrating peptide-superparamagnetic iron oxide nanoparticle conjugates via aniline-catalyzed oxime chemistry as bimodal imaging nanoagents*. Chemical Communications, 2012. **48**(43): p. 5322-5324.
- [13] Al Faraj, A., et al., *Specific targeting and noninvasive magnetic resonance imaging of an asthma biomarker in the lung using polyethylene glycol functionalized magnetic nanocarriers*. Contrast media & molecular imaging, 2015.
- [14] Al Faraj, A., et al., *Enhanced magnetic delivery of superparamagnetic iron oxide nanoparticles to the lung monitored using noninvasive MR*. Journal of Nanoparticle Research, 2014. **16**(10): p. 1-11.
- [15] Harris, T.J., et al., *Proteolytic Actuation of Nanoparticle Self-Assembly*. Angewandte Chemie, 2006. **118**(19): p. 3233-3237.
- [16] Ranzinger, F., et al., *Direct surface visualization of biofilms with high spin coordination clusters using Magnetic Resonance Imaging*. Acta biomaterialia, 2016. **31**: p. 167-177.
- [17] Cuny, L., et al., *Magnetic resonance imaging reveals detailed spatial and temporal distribution of iron-based nanoparticles transported through water-saturated porous media*. Journal of contaminant hydrology, 2015. **182**: p. 51-62.

6 Magnetic nanoparticles for hyperthermia applications

Kerstin Witte¹, Cordula Grüttner²

¹ University of Rostock, Institute of Physics, Albert-Einstein-Str. 23, 18059 Rostock, Germany

² micromod Partikeltechnologie GmbH, Friedrich-Barnewitz-Str. 4, 18119 Rostock, Germany

6.1 Introduction

Standard cancer therapies are based on surgery, chemotherapy, irradiation or combinations of these methods. Among the multiple attempts of alternative therapy concepts hyperthermia plays an important role [1]. Besides the whole body hyperthermia in which the body temperature is systematically raised to 41.8°C, there are different types of local hyperthermia using microwave radiation, capacitive or inductive coupling of radiofrequency fields, implanted electrodes, ultrasounds or lasers [1]. In local hyperthermia the temperature increase compared to the standard temperature of human body is considered to be therapeutically useful over a relatively broad temperature range with different mechanisms of cell damages by increasing temperature. Two different types of local hyperthermia will be further addressed – treatments of temperature of 42°C to 45°C for up to few hours, which is actually denoted as hyperthermia and mainly requires a combination with a toxic agent for a reliable damage of the cancer cells, and thermoablation which aims for the thermal killing of cancer cells applying temperatures of at least 50°C in the tumor region for several minutes [1, 2]. Using magnetic nanoparticles (MNPs) for local hyperthermia including actual hyperthermia and thermoablation, particles are dispersed into the target tissue and an external alternating magnetic field with a certain field strength and frequency is applied. This leads to heating of the particles via Neel loss, Brown loss, hysteresis or frictional losses [1, 3].

The heating efficiency, the specific power loss (SPL), of the particles depends on the magnitude of the magnetic fields for a given frequency as well as the properties of the MNPs themselves [1, 4]. The most influential factors are saturation magnetization, anisotropy, relaxation time, particle concentration, Brownian motion and inter-particle interactions as well as particle size, core size, size distribution, particle shape and crystallinity [1, 4, 5].

The specific power loss SPL is related to the loss power density P , which for example is for superparamagnetic nanoparticles in the linear response theory connected to the imaginary part of the susceptibility χ'' , the magnetic field H and the frequency f by [1]:

$$P(f, H) = \mu_0 \pi \chi''(f) H^2 f.$$

Therefore, it is a function of the external field and the frequency, nevertheless the increase of f and H is limited due to technical but also medical limitation. Due to an alternating magnetic field also eddy currents are induced in the body of the patient leading to an unwanted heating of cancerous as well as healthy tissue reducing the selectivity [1]. A limiting criterion for the product of magnetic field and frequency was determined for current loop with a diameter of 30 cm to be

$4.85 \cdot 10^8 \text{ Am}^{-1}\text{s}^{-1}$ [1, 6]. Depending on the body region being exposed to the alternating magnetic field and the seriousness of the cancer this product may be exceeded.

The common measure of the SPL is the specific absorption rate (SAR) and is associated by the unit mass of magnetic material involved [5]:

$$\text{SAR} = \frac{m_{\text{sample}}}{m_{\text{iron oxide}}} \cdot C_m \cdot \frac{\Delta T}{\Delta t}$$

Where C_m is the specific heat capacity of the sample, m_{sample} and $m_{\text{iron oxide}}$ are the masses of the ferrofluid and the iron oxide, respectively, and ΔT is the temperature increase and Δt the time interval.

This overview will consider MNPs from **micromod** that were demonstrated to be interesting tools for hyperthermia applications. Especially MNPs of the product types nanomag[®]-D-spio, nanomag[®]-D and Bionized NanoFerrite (BNF) with nominal hydrodynamic diameters of 20 nm to 250 nm were investigated in various hyperthermia studies. These particles provide high heating rates and suitable surface modifications to improve colloidal stability, prevent aggregation of nanoparticles, ensure non-toxic status in physiological conditions and allow the introduction of functional groups for binding of target-specific biomolecules for hyperthermia applications. Targeted applications of MNPs for hyperthermia are summarized in chapter 8.

6.2 Characterization of MNPs for hyperthermia application

Bordelon et al. reported that the amplitude-dependent heating properties (4 kA/m to 94 kA/m) of Bionized NanoFerrite (BNF) nanoparticles and nanomag[®]-D-spio both with a hydrodynamic diameter of 100nm, and Feridex[®] particles with a hydrodynamic diameter in the range of 120 nm to 180 nm show qualitatively different behavior [4]. For the realization of the studies a calorimeter coil was developed to generate fields up to 100 kA/m at a frequency of 150 kHz. The considerable changes in the amplitude-dependent heating suggests that the particles have significantly different magneto-structural differences beside their similar size regimes and their chemical composition [4]. Strong interactions between the particles exist and are especially pronounced for the BNF particles, contributing to the heating of the particles in an external magnetic field [4].

Two types of BNF particles were produced with a different thickness of the dextran shell to investigate the influence of the shell thickness on the heating properties. Both kinds of BNF particles, once with a single dextran and the second with a double dextran layer, showed similar saturation magnetization, anisotropy and volume of the particles but significantly different SAR values of 150 W/g(Fe) and 1075 w/g(Fe), respectively, measured at 86 kA/m and 150 kHz [7]. Due to the double dextran coating of the particles the interaction radius of the particles was increased by a factor of approximately 3 [7].

magnetic micro- and nanoparticles

Furthermore, the specific absorption rate of BNF particles with different hydrodynamic diameters of 30 nm, 60 nm and 90 nm was studied in dependence on the amplitude of the alternating magnetic field (AMF) for a frequency of 153 kHz (Fig. 1). With an increasing particle size a direct increase of the SAR can be observed as well as an increasing SAR for increasing amplitudes [8].

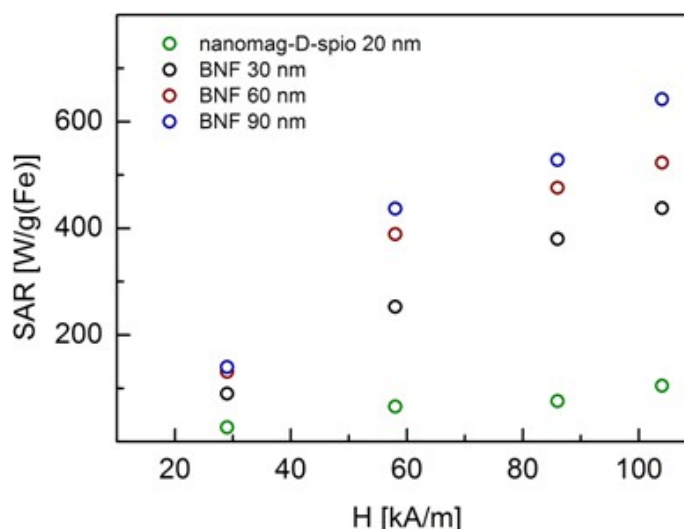


Figure 1. SAR of the BNF 30 nm, 60 nm, 90 nm and nanomag[®]-D-spio particles in dependence of the amplitude of the magnetic field for a frequency of 153 kHz (compare [8]).

6.3 Basic studies on advantages and limitations of hyperthermia with MNPs

6.3.1 Optimization of magnetic field strength and duration of hyperthermia treatment

It was expected that inter-particle interactions may affect the heating of MNPs in an AMF in two ways: the dipolar interaction will be significantly stronger for couple particles in an oscillating magnetic field and thereby amplifying the heating and due to the small interaction radius compared to the particle size particles group closer together enhancing the local heat output [7, 9]. *In vivo* mouse therapy was performed in an AMF inductor with twelve female mice (C3H/HeJ) bearing MTG-B murine breast tumors with a volume of $180 \pm 40 \text{ mm}^3$ [9]. The particle suspension was directly injected into the central region of the tumor after the mice were anaesthetized and treated with different external magnetic fields. Each mouse received a normalized dose of particles per tumor volume ($4.98 \pm 0.03 \text{ mg(Fe)/cm}^3$) [9]. The therapy was adjusted by varying the amplitude of the magnetic field and the duration of the therapy using a fixed frequency of 150 kHz. The therapy began when the tumor reached a temperature of $40.5 \text{ }^\circ\text{C}$ and terminated after 15 min, or when the rectal temperature of the mouse reached $41.5 \text{ }^\circ\text{C}$ or the tumor temperature $55 \text{ }^\circ\text{C}$ [9]. At higher field amplitudes the heat dose or SAR created a rapid heating leading to shorter treatment time [9]. When the magnetic field amplitude was 55.7 kA/m or higher the SAR increased drastically and produced substantial intra-tumor heating with the used nanoparticles, but also non-specific heat deposition by eddy currents was increased [9]. Nevertheless, a greater

therapeutic response was achieved using higher magnetic fields with a shorter duration of the treatment. Experimental evidence demonstrated that for interacting BNF nanoparticles, determined by their spacing and anisotropy, the resulting collective behavior in the kilohertz frequency regime generates significant heat, leading to nearly complete regression of aggressive mammary tumors in mice [9].

6.3.2 Relation between cancer cell association with MNPs and tumor cell cytotoxicity

The physical association of cancer cells with MNPs was studied to determine the nanoparticle-induced cytotoxicity [10]. The time dependent cellular uptake of intratumorally administered iron oxide nanoparticles in a murine breast adenocarcinoma cell line (MTG-B) was studied *in vivo*. Tumors with averaging volumes of 115 mm^3 were injected with 100 nm BNF-Dextran particles. The tumors were then excised and fixed for TEM at time 0.1–120 h after injection. Intracellular uptake was 5.0, 48.8 and 91.1% uptake at one, 2 and 4 h post-injection, respectively, suggesting two time domains for intratumorally delivered MNP hyperthermia. Based on the observations of Giustini et al., there does not appear to be a specific anatomic location of the nanoparticles within the cells. Once tumor cells have aggregated the nanoparticles intracellularly, more heat will be deposited into the tumor upon AMF activation with the same field strength and frequency, resulting in greater tumor cytotoxicity [10].

6.3.3 BNF particles as tools for numerical modeling of local heat transfer boundary conditions

Pearce et al. developed a numerical model based on finite element method that reveals the extent and dominance of local heat transfer boundary conditions and provides a new approach that may simplify the numerical problem sufficiently to make ordinary computer machinery capable of generating useful predictions [11]. Two numerical model series were executed assuming uniform nanoparticle heating in a magnetic field with uniformly dispersed individual nanoparticles and with clusters of MNPs of varying size in single- and multiple-cell sized model spaces. Experimental studies provided calibration and guidance for the numerical model studies [11]. A mouse flank tumor was injected with 100 nm BNF-Starch particles and heated for 24 min in a magnetic field with 48 kA/m peak to peak. The surface temperature was monitored reaching 42°C after 17 min of the treatment. Numerical results showed the importance of nanoparticles clustering to achieve adequate heating [11]. The volume powder generation to achieve therapeutic values decreases dramatically when the distance between unheated isothermal surfaces increases. It was shown that local heat transfer is the dominant mechanism [11] supporting the suggestion that the minimal treatable tumor size is likely about 2 mm in radius [12]. It was pointed out that to achieve tissue heating with nanoparticles and nanoparticle constructions the nanoparticle-nanoparticle association, the total iron dose, the volumetric powder density and the tissue geometry have to be matched [11].

6.3.4 Determination of the minimum tumor size for nanoparticle-mediated hyperthermia

Hedayati et al. studied the influence of cell cluster size on intracellular nanoparticle hyperthermia. Therefore DU145 cells were cultured in flasks in the presence of poly-D-lysine coated 100 nm BNF–Starch nanoparticles [13]. Afterwards cell pellets were formed and exposed to an AMF with amplitudes in the regime of 50 Oe to 1200 Oe for *in-situ* measuring the temperature of the pellets. The measured surface temperatures were consistent with those predicted by a heat diffusion model ignoring intercellular thermal barriers [13]. After heat treatment the cells were plated and the fractional survival was determined by a clonogenic assay [13]. It was shown that for a given intracellular nanoparticle concentration, a critical minimum number of cells is required for cytotoxic hyperthermia. Above this threshold, the cytotoxicity increases with raising cell number. It was suggested that the minimum tumor volume threshold is 1 mm³ below which nanoparticle-mediated heating is unlikely to be effective as the only cytotoxic agent [13].

6.3.5 Protection of healthy tissue at hyperthermia treatment

To assess the potential for injuries of normal tissue by hyperthermia treatment in mice, twenty three male nude mice received intravenous injections of 100 nm nanomag[®]-D-spio particles on three days and were exposed to an AMF on the sixth day. A day later, the blood, liver and spleen were harvested and analyzed [14]. Each mouse was treated for 30 min in an AMF with a frequency in the regime of 140–160 kHz with amplitudes of 0 kA/m, 24 kA/m and 60 kA/m. In this pilot study it was demonstrated, that MNPs producing only modest heat output can cause damage, and even death, when sequestered in sufficient concentrations. The superparamagnetic iron oxide dextran nanoparticles are deposited in liver and spleen, making these the sites of potential toxicity [14].

6.3.6 Image-guided hyperthermia therapy of liver cancer

In a feasibility study, Attaluri et al. sought to determine whether a formulation composed of MNP iron oxide multi-crystallite cores and ethiodised oil might provide sufficient heating using AMFs and image-guidance for transcatheter intra-arterial and intratumoral delivery in animal models [15]. The developed formulation, called BNF-lip, comprises 100 nm BNF-Starch particles emulsified with polysorbate 20 in ethiodised oil. *In vivo* thermal therapy capability was tested in two groups of male Foxn1^{nu} mice bearing subcutaneous HepG2 xenograft tumors. Group I was used to screen conditions for group II. In group II, mice received one of BNF-lip, BNF alone, or PBS, followed by alternating magnetic field hyperthermia, with different durations (15 or 20 min) and amplitudes (0, 16, 20, or 24 kA/m). Furthermore, image-guided fluoroscopic intra-arterial injection of BNF-lip was tested in New Zealand white rabbits, bearing liver VX2 tumors. The tumors were histopathologically evaluated for distribution of BNF-lip. The BNF-lip formulation produced maximum tumor temperatures with AMF amplitudes larger than 20 kA/m (Fig. 2) and showed positive X-ray visibility and substantial shortening of T1 and T2 relaxation time, with sustained

magnetic micro- and nanoparticles

intratumoral retention up to 7 days post-injection [15]. Intratumoral BNF-lip distribution correlated well with CT imaging of intratumoral BNF-lip distribution. The BNF-lip formulation has favorable thermal and dual imaging capabilities for image-guided thermal therapy of liver cancer.

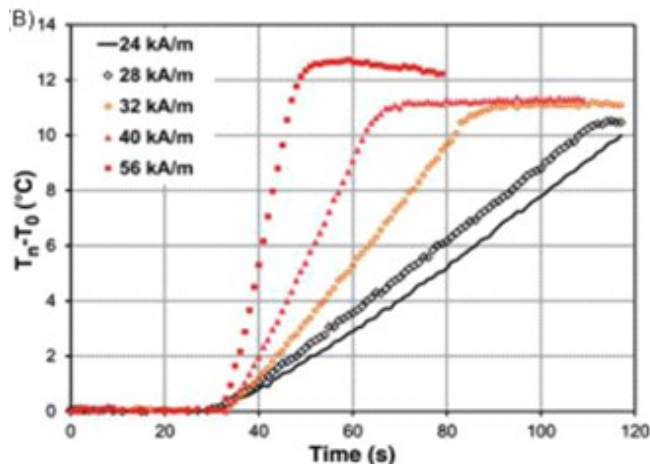


Figure 2. Specific heating rate measurements of BNF-lip formulation with varying amplitude at 155 kHz.

6.3.7 Comparison of MNP assisted hyperthermia and microwave hyperthermia

Comparing the effects of hyperthermia with MNPs to microwave hyperthermia treatment thermal doses equivalent to 60 min at 43°C were delivered to syngeneic mouse mammary adenocarcinoma flank tumors using both heating methods [16]. The MNPs used in the study were 100 nm BNF-Starch. After delivery of the particles the mouse tumor was exposed to an alternating magnetic field with a frequency of 165 kHz and a magnetic field strength of 35.8 kA/m obtaining a SAR of 151 W/g(Fe). The microwaves used in the study had a frequency of 915 MHz and were applied with a surface applicator. The time required for the tumor to reach three times the treatment volume was used as the endpoint of the primary study. The locally delivered particles resulted in a modest improvement in treatment efficacy as compared to microwave hyperthermia considering the same thermal dose [16]. Additionally, the tumors treated with MNP hyperthermia also demonstrated a reduction of the peritumoral normal tissue damage suggesting an improvement of the therapeutic ratio for locally delivered tumor hyperthermia [16].

6.4 Non-temperature induced effects of magnetized MNPs in AMF in cancer cells

The damaging effects of MNPs on magnetically labelled cancer cells when subjected to oscillating gradients in a strong external magnetic field were studied. Human breast cancer cells were labeled with plain 80 nm BNF-Starch particles, placed in the high magnetic field, and subjected to oscillating gradients generated by an imaging gradient system of a 9.4T preclinical MRI system. Changes in cell morphology and a decrease in cell viability were detected in cells treated with oscillating gradients. An approximately 26.6% reduction in cell viability was detected in magnetically labeled cells subjected to the combined effect of a static magnetic field

and oscillating gradients. No reduction in cell viability was observed in unlabeled cells subjected to gradients, or in MNP-labeled cells in the static magnetic field. As no increase in local temperature was observed, the cell damage was not a result of hyperthermia. Hapuarachchige et al. consider the coherent motion of internalized and aggregated nanoparticles that produce mechanical moments as a potential mechanism of cell destruction. This strategy provides a new way to eradicate a specific population of MNP-labeled cells, potentially with MRI guidance using standard MRI equipment, with minimal side effects for the host [17].

6.5 Hyperthermia for immune-related therapies

In vitro experiments using magnetically-loaded dendritic cells as vectors for thermotherapy have shown the potential of this 'Trojan horse' strategy for immune-related therapies. Therefore, the effects of alternating magnetic fields on the death rate of dendritic cells containing MNPs were investigated [18, 19]. Human-monocyte-derived dendritic cells were co-incubated with functionalized 250 nm nanomag[®]-D particles [18]. The cells were exposed to external alternating magnetic fields using field strengths of 3.2, 6.4, 9.5 and 12.7 kA/m at a constant frequency of 260 kHz for 5, 10 and 15 min. The viability of the dendritic cells could be controlled by the choice of the field strength and exposure time as well as the amount of particles loaded. About 20% of cells showed Annexin-negative/PI-positive staining after 5–10 min of exposure to the alternating magnetic field [18]. Necrotic-like populations were observed after exposure times of 10 min pointing out that locally relevant cell structures or metabolic processes can yield irreversible cell damage. Nevertheless, controlled cell death of dendritic cells containing MNPs was observed by adequate tuning of the parameters of the AMF and the concentration of the nanoparticles [18].

Staphylococcus aureus (*S. aureus*) has emerged as a leading cause of colonization and infection in various soft-tissue wounds including venous leg ulcers and diabetic foot ulcers resulting in the development of chronic non-healing wounds [20]. A novel antimicrobial magnetic thermotherapy was proposed in which an AMF is used to rapidly heat magnetic particle conjugated *S. aureus*. Therefore streptavidin coated 100 nm nanomag[®]-D-spio particles were conjugated to biotinylated anti-proteinA mAb and locally injected into the infected wound. Heating could facilitate efficient and rapid inactivation of bacterial cells and biofilms without further compromising fragile patients or exacerbating drug resistance [20]. The antimicrobial efficacy of this platform was evaluated in the treatment of both an *in vitro* culture model of *S. aureus* biofilm and a mouse model (EGFP-lys mice) of cutaneous *S. aureus* infection. In the systematic study, the bacteria were exposed to the nanomag[®]-D-spio particles in varying concentrations and exposed to an AMF with a field strength of 18 kA/m, 31 kA/m and 40 kA/m using a frequency of 2.1 MHz for 3 min. A 99.9% reduction in *S. aureus* bioluminescence was achieved at a dose of 150 µg nanoparticles at 40 kA/m and 99% at 200 µg using 31 kA/m demonstrating that an antibody-targeted MNP bound to *S. aureus* was effective at thermally inactivating *S. aureus* [20].

6.6 Summary

The development of MNPs for hyperthermia applications significantly increased over the last decades. Particles from **micromod** were studied in a broad variety of hyperthermia studies with different focusses from the basic to the applied research. An overview on the nanoparticles that were described in this review is given together with the core size, the hydrodynamic particle diameter and the parameters of the AMFs for the hyperthermia treatment in Table 1. The outstanding magnetic properties and the high diversity of surface functionalizations allow the use of BNF and nanomag[®]-D particles as interesting tools in hyperthermia applications. A short review on targeting of MNPs for hyperthermia applications is given in chapter 8.

Tab.1: Overview of the MNPs used for heating experiments with specific SAR values for a given field strength and frequency.

Particle name	Hydrodynamic diameter [nm]	Surface	SAR [W/g(Fe)]	H [kA/m]	f [kHz]	Reference
BNF	30	dextran	90	29	153	[8]
			253	58	153	
			380	86	153	
			438	104	153	
BNF	60	dextran	131	29	153	[8]
			389	58	153	
			476	86	153	
			523	104	153	
BNF	90	dextran	140	29	153	[8]
			437	58	153	
			528	86	153	
			642	104	153	
BNF	108	starch	11	12	150	[4, 5]
			78	24	150	
			278	40	150	
			537	94	150	
	110	151	35.8	165	[16]	
BNF	100	dextran	250	35.8	150	[21]
nanomag [®] -D-spio	86	dextran	44	12	150	[4, 5]
			91	24	150	
			116	40	150	
			162	94	150	
nanomag [®] -D-spio	20	dextran	27	29	153	[8, 22]
			66	58	153	
			76	86	153	
			105	104	153	
nanomag [®] -D-spio	100	dextran/ streptavidin	900	31	2100	[20]

References

- [1] Hergt, R., et al., *Magnetic particle hyperthermia: nanoparticle magnetism and materials development for cancer therapy*. Journal of Physics: Condensed Matter, 2006. **18**(38): p. S2919.
- [2] Dennis, C., et al., *The influence of magnetic and physiological behaviour on the effectiveness of iron oxide nanoparticles for hyperthermia*. Journal of Physics D: Applied Physics, 2008. **41**(13): p. 134020.
- [3] Colombo, M., et al., *Biological applications of magnetic nanoparticles*. Chem Soc Rev, 2012. **41**(11): p. 4306-34.
- [4] Bordelon, D.E., et al., *Magnetic nanoparticle heating efficiency reveals magneto-structural differences when characterized with wide ranging and high amplitude alternating magnetic fields*. Journal of Applied Physics, 2011. **109**(12): p. 124904.
- [5] Grüttner, C., et al., *Synthesis and functionalisation of magnetic nanoparticles for hyperthermia applications*. International Journal of Hyperthermia, 2013. **29**(8): p. 777-789.
- [6] Brezovich, I.A., *Low frequency hyperthermia: capacitive and ferromagnetic thermoseed methods*. Medical physics monograph, 1988. **16**: p. 82-111.
- [7] Dennis, C., et al., *The influence of collective behavior on the magnetic and heating properties of iron oxide nanoparticles*. Journal of Applied Physics, 2008. **103**(7): p. 07A319.
- [8] Grüttner, C., et al., *Synthesis and antibody conjugation of magnetic nanoparticles with improved specific power absorption rates for alternating magnetic field cancer therapy*. J. Magn. Magn. Mat., 2007. **311**(1): p. 181-186.
- [9] Dennis, C., et al., *Nearly complete regression of tumors via collective behavior of magnetic nanoparticles in hyperthermia*. Nanotechnology, 2009. **20**(39): p. 395103.
- [10] Giustini, A., R. Ivkov, and P. Hoopes, *Magnetic nanoparticle biodistribution following intratumoral administration*. Nanotechnology, 2011. **22**(34): p. 345101.
- [11] Pearce, J., et al., *Magnetic Heating of Nanoparticles: The Importance of Particle Clustering to Achieve Therapeutic Temperatures*. Journal of Nanotechnology in Engineering and Medicine, 2013. **4**(1): p. 0110071-01100714.
- [12] Etheridge, M. and J. Bischof, *Optimizing magnetic nanoparticle based thermal therapies within the physical limits of heating*. Annals of biomedical engineering, 2013. **41**(1): p. 78-88.
- [13] Hedayati, M., et al., *The effect of cell-cluster size on intracellular nanoparticle-mediated hyperthermia: is it possible to treat microscopic tumors*. Nanomedicine, 2012. **8**(1): p. 29-41.
- [14] Kut, C., et al., *Preliminary study of injury from heating systemically delivered, nontargeted dextran-superparamagnetic iron oxide nanoparticles in mice*. Nanomedicine, 2012. **7**: p. 1697-1711.

- [15] Attaluri, A., et al., *Image-guided thermal therapy with a dual-contrast magnetic nanoparticle formulation: A feasibility study*. International Journal of Hyperthermia, 2016. **32**(5): p. 543-557.
- [16] Petryk, A.A., et al., *Comparison of magnetic nanoparticle and microwave hyperthermia cancer treatment methodology and treatment effect in a rodent breast cancer model*. International Journal of Hyperthermia, 2013. **29**(8): p. 819-827.
- [17] Hapuarachchige, S., et al., *Non-Temperature Induced Effects of Magnetized Iron Oxide Nanoparticles in Alternating Magnetic Field in Cancer Cells*. PLoS ONE, 2016. **11**(5): p. e0156294.
- [18] Asin, L., et al., *Controlled cell death by magnetic hyperthermia: effects of exposure time, field amplitude, and nanoparticle concentration*. Pharm. Res., 2012. **29**: p. 1319-1327.
- [19] Asin Pardo, L., *Biomedical applications of magnetic nanoparticles: magnetic hyperthermia in dendritic cells and magnetofection in brain cells*. PhD thesis, University of Zaragoza, Spain, 2012.
- [20] Kim, M.-H., et al., *Magnetic nanoparticle targeted hyperthermia of cutaneous staphylococcus aureus infection*. Ann. Biomed. Eng., 2013. **41**(3): p. 598-609.
- [21] Zhang, J., et al., *Herceptin-directed nanoparticles activated by an alternating magnetic field selectively kill HER-2 positive human breast cancer cells in vitro via hyperthermia*. Int. J. Hyperthermia, 2011. **27**(7): p. 682-697.
- [22] DeNardo, S.J., et al., *Development of tumor targeting bioprobes (¹¹¹In-chimeric L6 monoclonal antibody nanoparticles) for alternating magnetic field cancer therapy*. Clinical Cancer Research, 2005. **11**(19): p. 7087s-7092s.

7 Magnetic nanoparticles as tracers for Magnetic Particle Imaging (MPI)

Kerstin Witte^{1,2}, Cordula Grüttner², Fritz Westphal²

¹ University of Rostock, Institute of Physics, Albert-Einstein-Str. 23, 18059 Rostock, Germany

² micromod Partikeltechnologie GmbH, Friedrich-Barnewitz-Str. 4, 18119 Rostock, Germany

7.1 Introduction

Magnetic particle imaging (MPI) is a new imaging technique, providing three-dimensional imaging of magnetic nanoparticle (MNP) tracers with high spatial and temporal resolution [1]. In MPI, only the MNPs generate the signal, in contrast to hydrogen being the signal origins of Magnetic Resonance Imaging (MRI). The MPI signal is generated by the nonlinear magnetic response of the tracers to a sinusoidal magnetic field, which produces higher order harmonics in the signal that can be analysed by Fourier transformation as illustrated in Fig. 1. Further on, the higher harmonics can be filtered out. When the particles are additionally exposed to a superpositioning magnetic field of certain amplitude the generation of higher harmonics can be suppressed. A spatial encoding is possible [1] by generating a single point in the sample, a so called field free point (FFP), where the superpositioning field is zero. This can be obtained using a Maxwell coil pair which consists of two opposing coils driven by current flowing in opposite directions. A scanning movement of the FFP over the sampling volume can be used for a spatial image reconstruction of MNP positions.

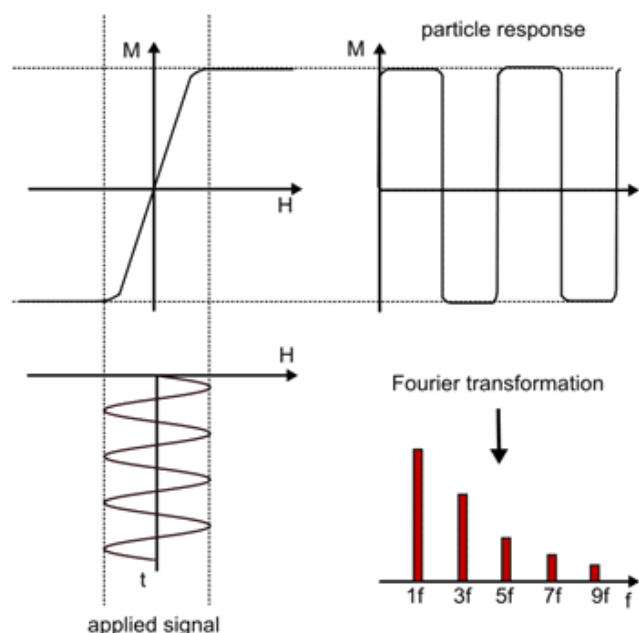


Fig. 1: Schematics of the MPI working principle.

The sensitivity of MPI depends critically on the magnetic moment of the tracers. Acceptable performance is expected for magnetite MNP with a core size of 30 nm and larger [2]. To date, Resovist® as approved contrast agent for MRI has been used in most MPI studies because of its comparatively large signal strength. This high MPI performance was not well understood since the size of the magnetite/maghemite cores is only about 5 nm [3]. However, there are clusters of primary 5 nm cores present in Resovist®, which have been identified as the most relevant MPS-active tracers [4]. Micromod's perimag® nanoparticles (former name: nanomag®-MIP or M4E) also have clusters and show promising tracer signals in MPI. The amplitude A_3 of the 3rd harmonic in the MPS spectrum of perimag® is twice as high as that of Resovist® (Figure 2). Here

magnetic micro- and nanoparticles

we provide a summary on the application of perimag® and nanomag®-D-spio particles as model contrast agents to demonstrate various new strategies for the enhancement of the MPI technique. Furthermore initial approaches to improve the evidence of imaging results in comparison to established imaging techniques (e.g. MRI or SPECT) will be addressed.

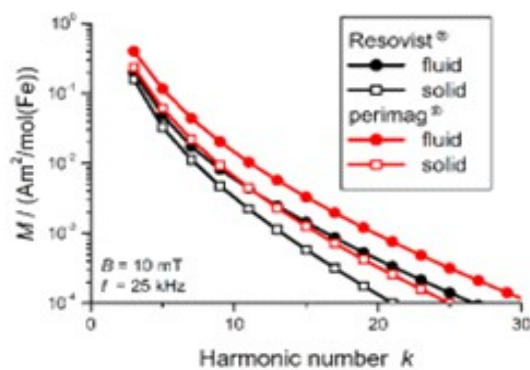


Figure 2. MPS-data obtained for suspended and immobilised (by freeze drying) MNPs of Resovist® and perimag [2].

7.2 Enhancement of the MPI technique to improve the imaging quality

Alternatively to image reconstruction by Fourier transformation the x-space approach raised increasing attention [5]. The x-space analysis commonly utilizes the FFP magnetic field gradient to localize magnetic nanoparticles. With the benefits of two orders of magnitude reduced acquisition time or one order of magnitude signal-to-noise ratio (SNR) improvement, a gradient called a Field Free Line (FFL) has been theoretically developed, and experimentally demonstrated. The FFL localizes particles to a line instead of a point. Konkle et al. have used a FFL with sample rotation and projection reconstruction to demonstrate experimental images with a 20 fold improvement in acquisition time compared to the first projection reconstruction (PR) MPI results. To gain this 20 fold speed up, a z-direction focus field coil configuration was implemented instead of the previously utilized translation stage [6]. Nanomag®-D-spio particles were used as tracers to prove this approach. The x-space approach overcomes time restrictions from overlap of FFP movement and harmonic analysis of a volume element by assuming an instant MNP response to traversing FFP, leading to the detection of a Point Spread Function (PSF). Mathematical analyses of the PSF by direct currency (DC) recovery methods are often more robust against variations in MNP characteristic spectroscopic signal response. Quantitative MPI across rat sized fields of view was demonstrated with x-space reconstruction methods. Critical to any medical imaging technology is the reliability and accuracy of image reconstruction. Furthermore, Konkle et al. have formulated x-space reconstruction as a 3d convex optimization problem and applied robust *a priori* knowledge of image smoothness and non-negativity to reduce non-physical banding and haze artifacts. Figure 3 demonstrates the improved imaging quality with the newly developed method [7]. Croft et al. have explored how nanoparticle relaxation affects image resolution. The influence of the time constant of nanoparticle rotation on the final image resolution was studied to reveal nonobvious conclusions for tailoring MPI imaging

magnetic micro- and nanoparticles

parameters for optimal spatial resolution and explain how a drive field sequence optimization can improve the MPI spatial resolution of multicore particles like perimag® (formerly known as nanomag®-MIP) [8].

Recently, there is a growing interest in the functional imaging capabilities of MPI. “Color MPI” techniques show the possibility of separating different nanoparticles, which could potentially be used to distinguish nanoparticles in different states or environments. Viscosity mapping is a promising functional imaging application for MPI, as increased viscosity levels *in vivo* have been associated with numerous diseases such as hypertension, atherosclerosis, and cancer. Utkur et al. proposed a viscosity mapping technique for MPI through the estimation of the relaxation time constant of the nanoparticles. Importantly, the proposed time constant estimation scheme does not require any prior information regarding the nanoparticles. The method was validated with extensive experiments in an in-house magnetic particle spectroscopy (MPS) setup at four different frequencies (between 250 Hz and 10.8 kHz) and at three different field strengths (between 5 mT and 15 mT) for viscosities ranging between 0.89 mPa·s to 15.33 mPa·s. For these experiments perimag® suspensions were diluted with different mixtures of water and glycerol. The results demonstrate that the viscosity mapping ability of MPI is in the biologically relevant viscosity regime [9].

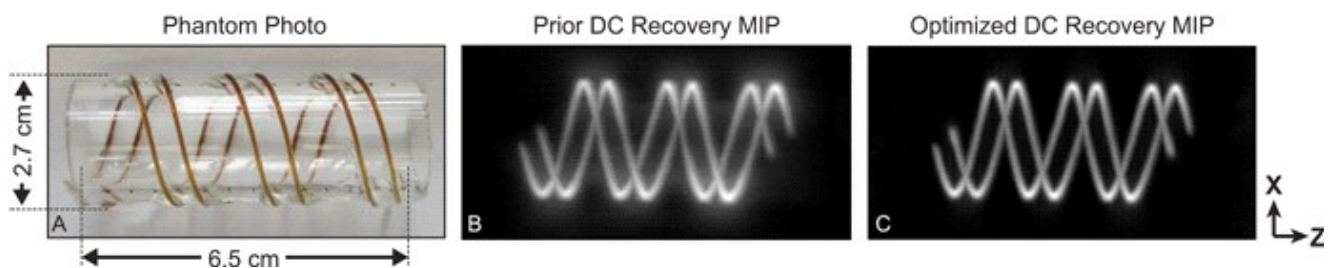


Figure 3. Experimental data from a double helix phantom filled with perimag® particles. The 3D dataset was reconstructed using the previous DC recovery method (middle) and the newly developed method (right) [7]

7.3 Biomedical imaging applications

MPI has a high potential for angiographic and cell tracking applications. MPI exhibits near perfect contrast with no background signal, as well as quantitative imaging capabilities [10]. Especially stem cell therapies have enormous potential for treating many debilitating diseases, including heart failure, stroke and traumatic brain injury. For maximal efficacy, these therapies require targeted cell delivery to specific tissues followed by successful cell engraftment. But commonly intravenous deliveries of mesenchymal stem cells (MSCs) become entrapped in lung microvasculature instead of the target tissues. Zheng et al. demonstrated that MPI can directly image MNP-tagged cells *in vivo*. Therefore MPI, fluorescence, and MRI tracer imaging techniques were compared by injection of perimag® particles together with Angiosense 680 EX fluorescent tracer into post-mortem mouse to demonstrate the advantages of the MPI technique [11]. The dynamic trafficking of intravenous MSC administrations using MPI indicates that injections of MNP-labelled MSCs are immediately entrapped in lung tissue and then cleared to the liver within

one day, whereas standard iron oxide particle (e.g. Resovist®) injections are immediately taken up by liver and spleen [12]. Drews et al. have selectively targeted and delivered a contrast agent to atherosclerotic plaques through the use of peptides that bind to unique markers of plaque development with the goal to use Magnetic Particle Imaging (MPI) to diagnose atherosclerotic plaques. Therefore aminated perimag® particles were conjugated to RGD peptide for injection into carotid ligation mice, and to CREKA peptide for injection in ApoE knockout mice. ApoE knockout mice develop atherosclerotic plaques in the aorta, which provides a greater surface area for contrast agent to bind. The selective binding of CREKA conjugated perimag® particles resulted in a low signal in the brachiocephalic artery present in MRI and MPI images. This effect was not visible for RGD conjugated perimag® in the carotid ligation mice model [13].

Aminated perimag® particles with a medium positive zeta potential (M4E) show direct uptake in human mesenchymal stem cells (hMSCs) without use of transfection agents. Kilian et al. analyzed the suitability of positively charged perimag® for safe human stem cell (hMSC) labelling and determined cell labelling maintenance in 2D and 3D culture for cell tracking by MRI and MPI (Fig. 4). The experiments demonstrated that the particles have neither toxic effects nor alter the function of the stem cells [14].

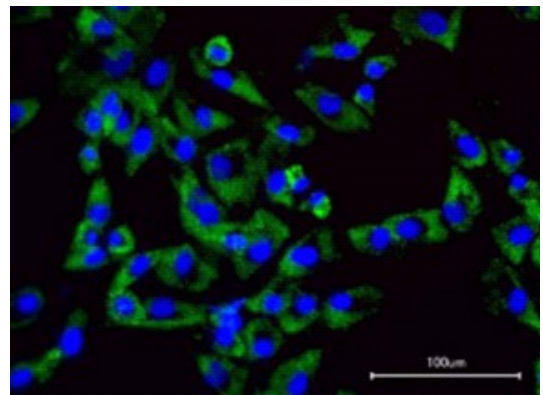


Figure 4. Labeling of hMSC with fluorescent perimag® (nucleus: blue; perimag® in cytoplasm: green) [14].

References

- [1] Gleich, B. and J. Weizenecker, *Tomographic imaging using the nonlinear response of magnetic particles*. Nature, 2005. **435**(7046): p. 1214-1217.
- [2] Eberbeck, D., et al., *Multicore magnetic nanoparticles for magnetic particle imaging*. IEEE TRANSACTIONS ON MAGNETICS, 2013. **49**(1): p. 269-274.
- [3] Lawaczeck, R., et al., *Magnetic iron oxide particles coated with carboxydextran for parenteral administration and liver contrasting: pre-clinical profile of SH U555A*. Acta Radiologica, 1997. **38**(4): p. 584-597.
- [4] Eberbeck, D., et al., *How the size distribution of magnetic nanoparticles determines their magnetic particle imaging performance*. Applied Physics Letters, 2011. **98**(18252).
- [5] Goodwill, P.W. and S.M. Conolly, *Multidimensional x-space magnetic particle imaging*. IEEE transactions on medical imaging, 2011. **30**(9): p. 1581-1590.
- [6] Konkle, J.J., et al., *Twenty-fold acquisition time improvement in 3D projection reconstruction MPI*. Magnetic Particle Imaging (IWMPI), 2013 International Workshop on, 2013: p. 1-1.

- [7] Konkle, J.J., et al., *A Convex Formulation for Magnetic Particle Imaging X-Space Reconstruction*. PloS one, 2015. **10**(10): p. e0140137.
- [8] Croft, L.R., et al., *Low drive field amplitude for improved image resolution in magnetic particle imaging*. Medical physics, 2016. **43**(1): p. 424-435.
- [9] Utkur, M., Y. Muslu, and E.U. Saritas, *Relaxation-based viscosity mapping for magnetic particle imaging*. 2017.
- [10] Saritas, E.U., et al., *Magnetostimulation Limits in Magnetic Particle Imaging*. IEEE Transactions on Medical Imaging, 2013. **32**(9): p. 1600-1610.
- [11] Zheng, B., et al. *In situ and ex vivo MPI performance compared to fluorescent and MRI imaging*. in *Magnetic Particle Imaging (IWMPI), 2015 5th International Workshop on*. 2015. IEEE.
- [12] Zheng, B., et al. *Quantitative stem cell imaging with magnetic particle imaging*. in *Magnetic Particle Imaging (IWMPI), 2013 International Workshop on*. 2013. IEEE.
- [13] Drews, L.B., et al., *Imaging atherosclerotic plaques in vivo using peptide-functionalized Iron oxide nanoparticles*. Magnetic Particle Imaging (IWMPI), 2013 International Workshop on, 2013: p. 1-1.
- [14] Kilian, T., et al., *Stem cell labeling with iron oxide nanoparticles: impact of 3D culture on cell labeling maintenance*. Nanomedicine, 2016. **11**(15): p. 1957-1970.

8 Targeting applications with magnetic nanoparticles

Cordula Grüttner

micromod Partikeltechnologie GmbH, Friedrich-Barnewitz-Str. 4, 18119 Rostock, Germany

8.1 Magnetic nanoparticles for targeted magnetic resonance imaging (MRI) applications

The high spatial resolution of magnetic resonance imaging (MRI) is ideally suited for detection of cancer and assessment of response to therapy. Up to now MRI has found limited application in tumor imaging due to a lack of sensitivity. Advances in the use of magnetic nanoparticles (MNP) have the potential to address this limitation. Due to their large magnetic moments MNPs significantly increase MRI R_1 and R_2 relaxivities, leading to a marked reduction in T_1 and T_2 times. This allows sensitive visualization *in vivo*. Clinical application of MNPs as contrast agents has been demonstrated with Endorem[®], Feridex[®] and Resovist[®]. These MNPs are not tumor specific *per se* but instead provide positive contrast in tumors based on their uptake by healthy phagocytic cells in preference to cancerous cells [1]. The development of specific antibody labeled MNPs has a high potential to improve the selective MR imaging of tumor cells. Here we report on different strategies for the design of antibody conjugated MNPs for targeted MRI for different cancer cell types.

8.1.1 MR imaging of carcinoembryonic antigen (CEA)-expressing human tumor cells

Vigor et al. have generated antibody-functionalized MNPs using a single chain Fv antibody fragment (scFv) specific for carcinoembryonic antigen (CEA), an oncofoetal cell surface protein. Nanomag[®]-D-spio particles with diameters of 20 nm and 50 nm and different surface modifications were investigated. The antibody fragments were conjugated to the surface of the plain dextran particles via periodate activation of the dextran-OH groups or by carbodiimide (EDC)/ N-hydroxysuccinimide (NHS) activation of nanomag[®]-D-spio particles with PEG-COOH surface groups (Figure 1).

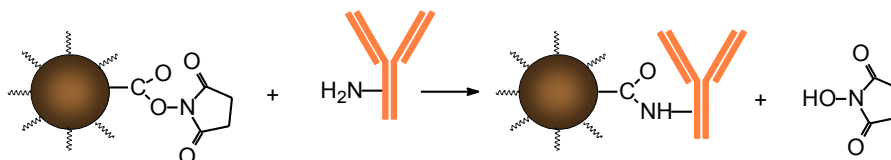


Figure 1. Activation of MNPs with COOH groups on the surface with EDC (1-Ethyl-3-(3-dimethylaminopropyl) carbodiimide) and NHS (N-hydroxysuccinimide) for conjugation with amino groups of the antibody

The targeting was confirmed by ELISA, cellular iron uptake, confocal laser scanning microscopy and MRI. The results demonstrated that the scFv-conjugated MNPs bound specifically to CEA-expressing human tumor cells, generating selective image contrast in MRI. The cellular interaction of the MNPs was influenced by hydrodynamic size and surface coating [1].

8.1.2 MR imaging of lymphocytes

Luchetti et al. found that monoclonal antibodies conjugated with superparamagnetic nanoparticles allow MRI detection of lymphocytes in the mouse brain. Different types of MNPs were conjugated with anti-mCD3 or anti-mB220 antibodies. Therefore the binding of biotinylated antibodies to the surface of streptavidin-modified particles was compared with the direct covalent binding of non-modified antibodies to the surface of 50 nm nanomag[®]-D-sprio, and 250 nm nanomag[®]-D particles by EDC/ NHS chemistry (Figure 1). These vectorialized MNPs were successfully employed to image B220+ cells in murine model of B-cell lymphoma. The specificity of the technique was confirmed by immunohistochemistry and electron microscopy. It was found that indirect antibody binding to streptavidin-modified MNPs allowed for enhanced particle vectorialization compared to covalent binding of the antibody to the particles [2].

8.1.3 MR imaging of prostate cancer cells

Many types of prostate cancer cells express high levels of prostate-specific membrane antigen (PSMA) on their cell surface. Abdolahi et al. studied the use of MNPs attached to an antibody that binds to the extracellular domain of PSMA, to specifically enhance the contrast of PSMA-expressing prostate cancer cells. Therefore the selective J591 mAb was conjugated to 20 nm nanomag[®]-D-sprio particles with PEG-NH₂ groups on the surface by maleimide chemistry (Figure 2.). These J591-nanoparticle conjugates were evaluated *in vitro* for specific detection of prostate cancer by MRI. Cell uptake experiments with two types of prostate cancer cell lines demonstrated the high potential of the antibody-nanoparticle conjugate as specific contrast agent for PSMA-expressing prostate cancer cells [3]

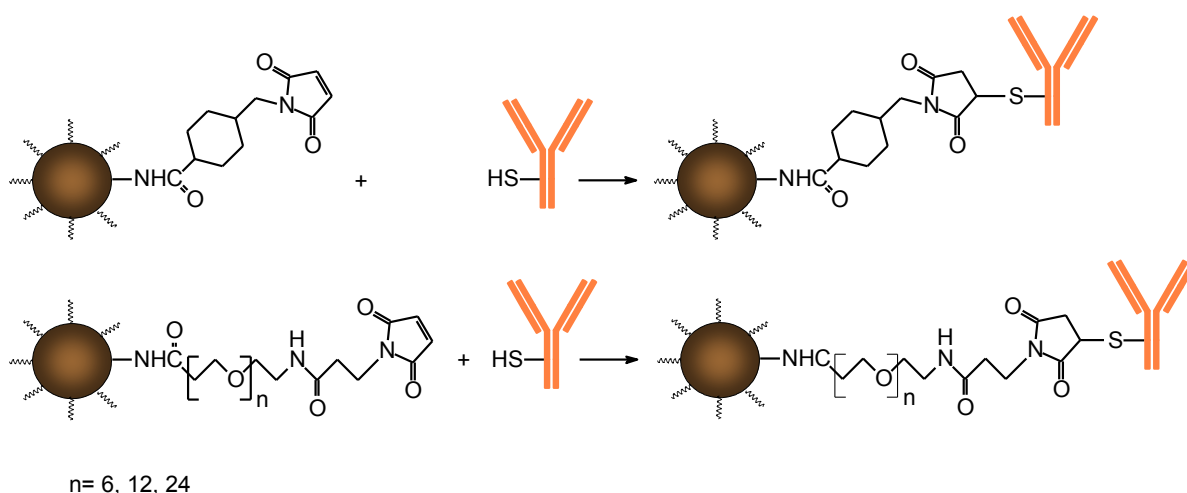


Figure 2. Functionalization of MNPs with amino groups on the surface with maleimide or PEG-maleimide groups for conjugation with thiol groups of the antibody

8.1.4 C595 antibody conjugated particles for MR imaging of ovarian and breast cancer cells

In another approach Shahbazi-Gahrouei and Abdolahi conjugated C595 mAb against MUC1-expressing ovarian cancer cells to the surface of 20 nm nanomag[®]-CLD-spio particles by maleimide chemistry (Figure 2). This potential MRI contrast agent for ovarian cancer detection was investigated *in vitro* and *in vivo* (mice). No cytotoxicity of the conjugate was found. MRI and biodistribution results showed good tumor accumulation and high sensitivity in detection [4, 5]. Shanehsazzadeh et al. also investigated C595 mAb conjugated 20 nm nanomag[®]-CLD-spio particles *in vitro* and *in vivo* for breast cancer imaging. In addition the antibody conjugated MNPs were radiolabeled with ^{99m}Tc for biodistribution studies. The conjugate showed considerable targeting yield for uptake in MUC1-positive breast cancer cell lines *in vitro*. In contrast to the results of the *in vivo* study of Shahbazi-Gahrouei and Abdolahi [5] the radiolabeled nanoprobe showed a high accumulation in liver and spleen demonstrating a significant reduction of the *in vivo* targeting. The reason for these different *in vivo* results could be the different tumor models (ovarian and breast cancer model) or a change of the surface properties of the nanoprobe by the radiolabeling process [6].

8.1.5 Detection of chronic obstructive pulmonary disease (COPD) by targeted MRI

Chronic obstructive pulmonary disease (COPD) was predicted to be the third leading cause of death by 2020. Al Faraj et al. studied the targeting and MR imaging of a specific alveolar macrophage subpopulation in lipopolysaccharide-induced COPD using antibody-conjugated MNPs [7]. The *in vivo* effect of pulmonary administration of MNPs on the polarization profile of macrophages was assessed, and a noninvasive free breathing MRI protocol with the use of antibody conjugated 20 nm nanomag[®]-CLD-spio particles was developed. CD86 or CD206 antibodies were covalently attached on the surface of PEG-NH₂ functionalized particles by maleimide chemistry (Figure 2). The MNPs were found to be biocompatible for lung administration in preclinical settings. Cluster of differentiation of CD86- and CD206-conjugated nanomag[®]-CLD-spio particles enabled successful noninvasive detection of M1 and M2 macrophage subpopulations. The particles were found to co-localize with inflammatory regions induced by lipopolysaccharide challenge and could offer a promising strategy for an early and better diagnosis of pulmonary inflammatory diseases using noninvasive MRI [7].

8.1.6 High specificity targeting and MR detection of human neuroblastoma using multifunctional anti-GD2 nanoparticles

Baiu et al. have developed biocompatible, tumor-specific multifunctional magnetic nanoparticles for the targeting of neuroblastoma, an aggressive pediatric malignancy [8]. Therefore clinical-grade humanized monoclonal antibody (hu14.18K322A) designed to target GD2 antigen on neuroblastoma with reduced nonspecific immune interactions was conjugated to 80 nm BNF-Starch nanoparticles by maleimide conjugation (Figure 2). The targeting capability *in vitro* and *in vivo* was assessed by immunofluorescence, electron microscopy, analytical spectrophotometry, histochemistry and magnetic resonance R2* relaxometry. The biocompatible nanoconstructs

magnetic micro- and nanoparticles

demonstrated high tumor specificity *in vitro* and *in vivo*, and low background uptake in a mouse flank xenograft model. Specific accumulation in tumors enabled particle visualization and quantification by magnetic resonance R2* mapping (Figure 3). This anti-GD2 iron-oxide nanoconstruct was shown to be an interesting diagnostic and therapeutic scaffold for neuroblastoma and potentially other GD2-positive malignancies and should be further developed toward clinical application [8].

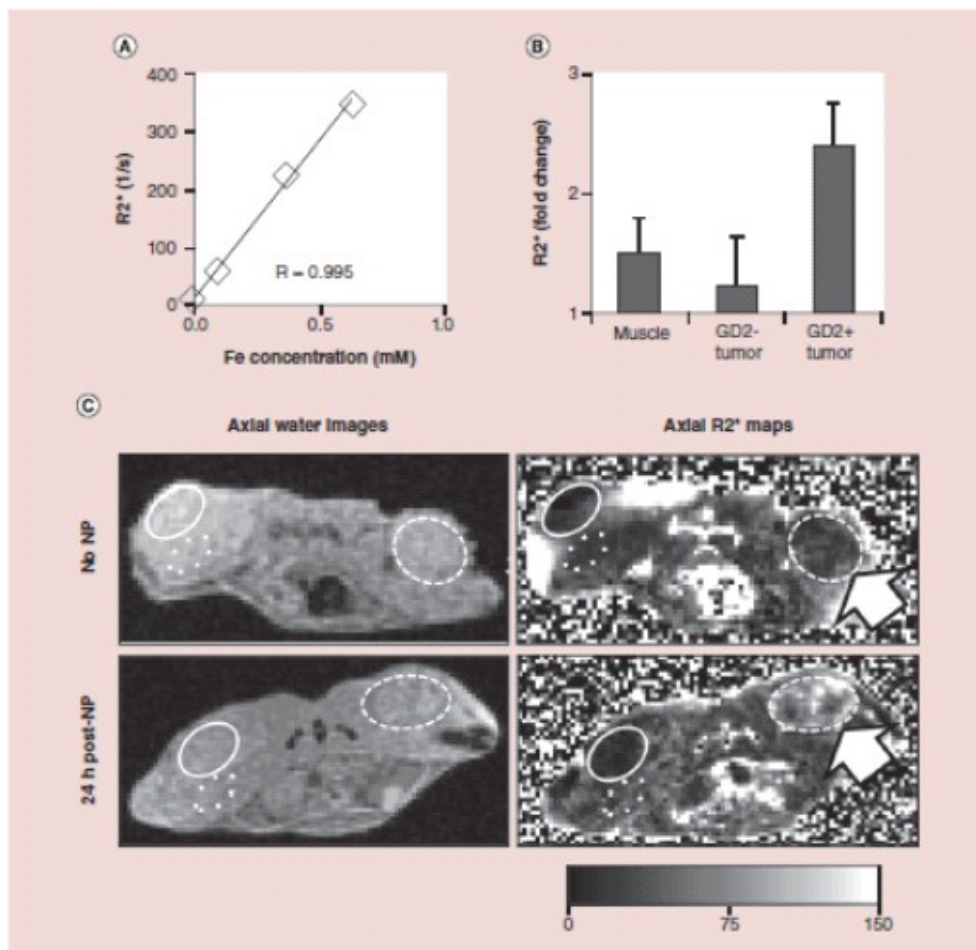


Figure 3. Iron oxide nanoparticles in GD2+ xenografts are detectable by magnetic resonance. (A) Correlation between MR R2* values and iron concentration for BNF nanoparticle phantoms (linear regression, coefficient $R = 0.995$). (B) R2* fold change in GD2+ tumors, GD2- tumors and muscle in mice 24 h after anti-GD2-BNF injection versus mice with no treatment. Averages \pm standard deviation, $n = 2$. (C) MR images (method parameters B) of a noninjected mouse (upper panels) and a mouse 24 h after intravenous anti-GD2-BNF NP administration shows elevated R2* for the injected mouse in the GD2+ tumor (arrow). Region of interest defined on water images (left panels) and corresponding R2* images (right panels) circumscribe GD2+ xenografts (CHLA-20, dashed line), GD2-xenografts (PC-3, solid line) and control skeletal muscle (dotted). Representative images of two experiments with two separate anti-GD2-BNF batches.

magnetic micro- and nanoparticles

8.1.7 Non-invasive detection of complement activation in placenta and foetal brain in an *in vivo in utero* model by MRI

Girardi et al. found that anti-complement C3-targeted 20 nm nanomag[®]-D-spio bind within the inflamed placenta and foetal brain cortical tissue, causing a shortening of the T2* relaxation time. Two mouse models of pregnancy complications were used in the study. The detection of C3 deposition in the placenta in the antiphospholipid syndrome (APS) model was associated with placental insufficiency characterized by increased oxidative stress, decreased vascular endothelial growth factor and placental growth factor levels and intrauterine growth restriction. The foetal brain C3 deposition was associated with cortical axonal cytoarchitecture disruption and increased neurodegeneration in both mouse models. Importantly, the C3-targeted nanomag[®]-D-spio particles did not affect pregnancy outcomes and liver function in the mother and the offspring, suggesting that this method may be useful for detecting complement activation *in vivo in utero* and predicting placental insufficiency and abnormal foetal neurodevelopment that leads to neuropsychiatric disorders [9].

8.1.8 Diagnosis and treatment of acute temporal lobe epilepsy with anti-IL-1b conjugated MNPs by MRI

Temporal lobe epilepsy (TLE) is the most prevalent form of adult focal onset epilepsy and is often associated with pharmacological resistance. A hallmark in the neuropathology of TLE is brain inflammation, in particular the activation of interleukin-1b (IL-1b) induced by activated glial cells, which has been considered a new mechanistic target for treatment. Fu et al. determined the feasibility of nanomag[®]-D-spio conjugated to anti-IL-1b monoclonal antibody to render MRI diagnoses and simultaneously provide targeted therapy with the neutralization of IL-1b overexpressed in epileptogenic zone of an acute rat model of TLE. This novel approach enhanced accumulation and the therapeutic effect of anti-IL-1b mAb by magnetic-targeted drug delivery system using MNPs [10].

8.2 MNPs for targeted magnetic particle imaging (MPI) applications

Atherosclerosis, or the formation of plaques in the arterial wall, leads to cardiovascular disease, the number one cause of death in the United States. Atherosclerosis develops through multiple stages, which makes it a particularly difficult disease to detect. Drews et al. have selectively targeted and deliver perimag[®] particles to atherosclerotic plaques through the use of peptides that bind to unique markers of plaque development and used MPI to diagnose atherosclerotic plaques [11].

8.3 MNPs for targeted multimodal imaging purposes

Multimodal imaging with targeted magneto-optical or magneto-radiolabeled probes allows for detection of a broad range of molecular-cellular targets through their modular design. Rimkus et al. described the construction of multimodal 20 nm nanomag[®]-CLD-spio particles addressing mVCAM-1 expression on endothelial cells as response to inflammatory factors [12]. The anti-

magnetic micro- and nanoparticles

VCAM-1 antibody was fluorescence labeled with DY649, thiolated and conjugated to maleimide or PEG-maleimide functionalized nanomag[®]-CLD-spio particles (Fig. 4). Results of optical imaging and MRI showed that the multimodal MNPs can selectively address mVCAM-1 on endothelial cells in murine animal models [12].

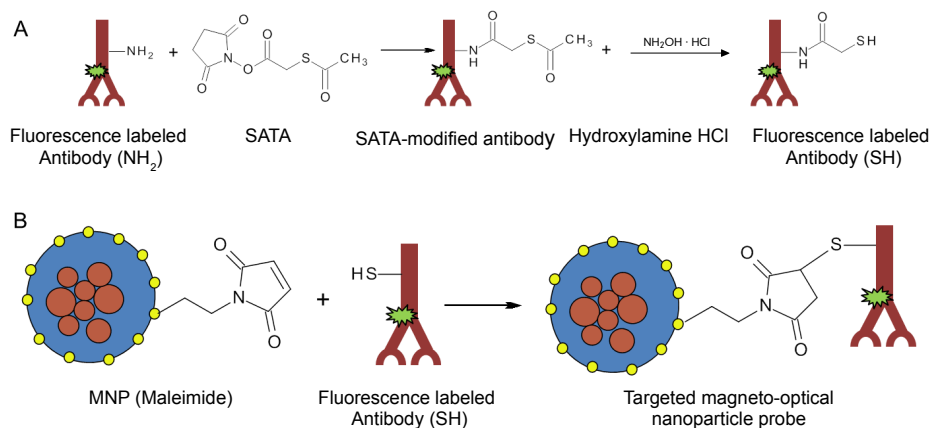


Figure 4. Reaction scheme of antibody-MNP conjugation using maleimide chemistry

Azad et al. have evaluated a PSMA-targeted BNF (Bionized NanoFerrite) nanoparticle in an experimental model for prostate cancer [13]. BNF-Starch particles with a diameter of 80 nm and amino groups on the surface were conjugated to a small-molecule PSMA inhibitor as well as to 1000 Da PEG chains. In addition the obtained nanoconjugate was labeled with the IRDye 800CW[®] for optical imaging or radiolabeled with ¹¹¹In for single photon emission computed tomography (SPECT). The conjugated BNF particles exhibit properties conducive to targeted imaging such as stealth, prolonged circulation time and enhanced clearance from non-target sites. Optical imaging of the targeted BNF particles *in vivo* indicates preferential accumulation in PSMA+ tumors 4 h post-injection, suggesting target specificity. On the other hand, non-targeted BNF particles exhibit lower uptake with similar accumulation in both PSMA+ and PSMA- tumors indicating tumor access without preferential accumulation. SPECT imaging and biodistribution studies indicated highest tumor accumulation at 48 h post-injection. *Ex vivo* fluorescence microscopy, Prussian blue staining, immunohistochemistry and biodistribution studies confirm enhanced BNF particle uptake in PSMA+ tumors compared to those not expressing PSMA. Thus the PSMA-targeted BNF particles are promising for PSMA-targeted imaging applications [13].

8.4 Magnetic nanoparticles for targeted hyperthermia applications

Heating living tissues to temperatures between 42°C and 46°C leads to inactivation of normal cellular processes in a dose-dependent manner described for decades as the classic hyperthermia response. External alternating magnetic fields (AMF) are an interesting possibility to induce heating of MNPs that are bound to the cancer cells. The degree to which this approach can be applied to cancer therapy depends on the MNPs, which after intravenous injection reach the cancer cells in effective concentrations for thermal ablation [14].

magnetic micro- and nanoparticles

DeNardo et al. developed ^{111}In -Chimeric L6 (^{111}In -ChL6) monoclonal antibody conjugated nanomag[®]-D-spio particles for AMF cancer therapy (Fig. 5). The pharmacokinetics, tumor uptake, and the therapeutic effect of inductively heating these nanoconjugates by externally applied AMF were studied in athymic mice bearing human breast cancer HBT3477 xenografts. Tumor cell radioimmunotargeting of the bioprobes and therapeutic and toxic responses were determined.

The ^{111}In -ChL6 antibody was bound to 20 nm nanomag[®]-D-spio particles with PEG-COOH groups on the surface by EDC/ NHS chemistry (Figure 5). The conjugated MNPs remained in the blood circulation sufficiently long to allow significant tumor accumulation. The presence of the MNPs in the tumor xenografts was confirmed by quantitation of the tumor radiotracer in the

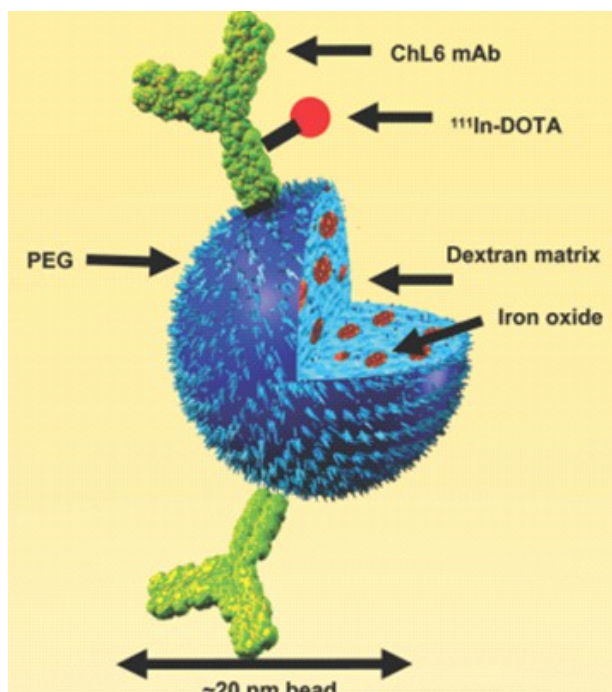


Figure 5. Schematic of ^{111}In -ChL6 antibody conjugated to PEG-COOH functionalized 20 nm nanomag[®]-D-spio particles

pharmacokinetics study and by electron microscopy of the MNPs in the tumor. Treated tumors having MNP-conjugates activated by AMF, demonstrated tumor growth delay without normal tissue toxicity. This tumor response correlated with the calculated heat dose delivered [14, 15]. The study was extended by the comparison of tumor targeting of these ^{111}In -ChL6 conjugated 20 nm nanomag[®]-D-spio particles with corresponding larger BNF particles with diameters of 30 nm and 100 nm. The larger BNF particles targeted the tumor less than the 20 nm nanomag[®]-D-spio particles, but their heating capacity is typically 6 times greater, suggesting the 100 nm BNF particles could still deliver a better therapy with AMF [16]. For the development of a second generation radio-immuno nanoparticle the targeting ChL6 antibody was replaced with anti-Muc-1 di-scFv-cysteine antibody fragment to provide more binding units per particle. The antibody fragment was bound to maleimide functionalized 20 nm nanomag[®]-CLD-spio particles via its terminal cysteine unit in analogy to Figure 2. This site-specific conjugation of the antibody fragment resulted in increased binding to breast cancer tumor cells in comparison to analogous particles with randomly oriented antibodies on the particle surface after conjugation with EDC/NHS chemistry (Figure 1) [17]. This result was confirmed by corresponding studies with model antibodies [18]. Further development of anti-Muc-1 di-scFv conjugated nanomag[®]-CLD-spio particles may provide uniquely high tumor targeting for AMF-driven tumor hyperthermia with less spleen and kidney accumulation [13].

Herceptin, or Trastuzumab, is a high affinity engineered mouse-human-chimeric monoclonal antibody that was raised against the extracellular domain of human epidermal growth factor receptor 2 (HER-2). HER-2 is overexpressed in 20-30% of breast, lung, ovarian and gastric adenocarcinomas. Herceptin was approved by the FDA for the treatment of patients with HER-2 overexpressing breast cancer [19]. Zhang et al. have used the maleimide chemistry (Figure 2) for Herceptin conjugation on the surface of aminated 100 nm BNF-Starch particles. The Herceptin conjugated BNF particles bound selectively to the tumor cells *in vitro*. After AMF exposure the tumor cells died by apoptosis, quantifiable by Live/Dead and nuclear morphology assays. These Herceptin-directed BNF particles can selectively kill HER-2+ human mammary cancer cells (SK-BR-3) by AMF treatment [15].

NDong et al. have compared the tumor cell targeting of 30 nm MNPs and 100 nm nanomag[®]-D-spio particles that were conjugated with Herceptin *in vivo* and *in vitro*. *In vitro*, molecular targeting to the HER-2 receptor was the dominant factor driving cancer cell association. In contrast, size was found to be the key determinant of tumor accumulation *in vivo*, where molecular targeting increased tumor tissue concentration for 30 nm but not 100 nm MNPs. These results indicate that the *in vitro* advantages of molecular targeting may not consistently be extended to pre-clinical *in vivo* settings [20].

8.5 Delivery of therapeutic molecules and MNPs inside cells by nontransgenic approaches

Efficient delivery of therapeutic molecules inside cells by nontransgenic approaches is key as gene editing/correction, directed differentiation, and *in vivo* cell modulation/tracking are translated for regenerative medicine applications. Dixon et al. developed a peptide-based system to enhance the activity of cell-penetrating peptides to achieve exceptional intracellular transduction. Glycosaminoglycan-binding enhanced transduction (GET) uses peptides that interact with cell membrane heparan sulfates and promote cell-penetrating peptide-mediated endocytosis into cells. Thus enzymes, transcription factors, antibodies, native proteins, MNPs (250 nm nanomag[®]-D), and nucleic acids could be delivered in cell types considered hard to transduce, such as mouse embryonic stem cells (mESCs), human ESCs, and induced pluripotent stem cells (hiPSCs). Importantly, this approach does not affect cell proliferation and viability and can be used to deliver a plethora of functional cargoes [21].

8.6 Biomimetic amplification of nanoparticle homing to tumors

MNP-based diagnostics and therapeutics mainly depend on the ability to home to specific sites in the body. Simberg et al. have developed biomimetic particles that not only home to tumors, but also amplify their own homing. The system is based on a peptide that recognizes clotted plasma proteins and selectively homes to tumors, where it binds to vessel walls and tumor stroma. Nanomag[®]-D-spio particles and liposomes coated with this tumor-homing peptide accumulate in tumor vessels, where they induce additional local clotting thereby producing new binding sites for more particles. The system mimics platelets, which also circulate freely but accumulate at a

diseased site and amplify their own accumulation at that site. The self-amplifying homing is a novel function for nanoparticles that greatly enhances tumor imaging [22].

References

- [1] Vigor, K.L., et al., *Nanoparticles functionalised with recombinant single chain Fv antibody fragments (scFv) for the magnetic resonance imaging of cancer cells*. *Biomaterials*, 2010. **31**: p. 1307-1315.
- [2] Luchetti, A., et al., *Monoclonal antibodies conjugated with superparamagnetic iron oxide particles allow magnetic resonance imaging detection of lymphocytes in the mouse brain*. *Molecular imaging*, 2012. **11**(2): p. 114.
- [3] Abdolahi, M., et al., *Synthesis and in vitro evaluation of MR molecular imaging probes using J591 mAb-conjugated SPIONs for specific detection of prostate cancer*. *Contrast media & molecular imaging*, 2013. **8**(2): p. 175-184.
- [4] Shahbazi-Gahrouei, D. and M. Abdolahi, *Detection of MUC1-expressing ovarian cancer by C595 monoclonal antibody-conjugated SPIONs using MR imaging*. *ScientificWorldJournal*, 2013. **2013**: p. 609151.
- [5] Shahbazi-Gahrouei, D. and M. Abdolahi, *Superparamagnetic iron oxide-C595: Potential MR imaging contrast agents for ovarian cancer detection*. *Journal of Medical Physics*, 2013. **38**(4): p. 198-204.
- [6] Shanehsazzadeh, S., et al., *Monoclonal antibody conjugated magnetic nanoparticles could target MUC-1-positive cells in vitro but not in vivo*. *Contrast Media & Molecular Imaging*, 2014: p. n/a-n/a.
- [7] Al Faraj, A., et al., *MR imaging and targeting of a specific alveolar macrophage subpopulation in LPS-induced COPD animal model using antibody-conjugated magnetic nanoparticles*. *Int. J. Nanomed.*, 2014. **9**: p. 1491-1503.
- [8] Baiu, D.C., et al., *High specificity targeting and detection of human neuroblastoma using multifunctional anti-GD2 iron-oxide nanoparticles*. *Nanomedicine*, 2015. **10**(19): p. 2973-2988.
- [9] Girardi, G., et al., *Imaging of activated complement using ultrasmall superparamagnetic iron oxide particles (USPIO)-conjugated vectors: an in vivo in utero non-invasive method to predict placental insufficiency and abnormal fetal brain development*. *Molecular psychiatry*, 2015. **20**(8): p. 1017-1026.
- [10] Fu, T., et al., *Value of Functionalized Superparamagnetic Iron Oxide Nanoparticles in the Diagnosis and Treatment of Acute Temporal Lobe Epilepsy on MRI*. *Neural plasticity*, 2016. **2016**.

- [11] Drews, L.B., et al., *Imaging atherosclerotic plaques in vivo using peptide-functionalized iron oxide nanoparticles*. Magnetic Particle Imaging (IWMPI), 2013 International Workshop on, 2013: p. 1-1.
- [12] Rimkus, G., et al., *mVCAM-1 specific iron oxide nanoparticles based probes for multimodal imaging purposes*. Biomed Tech, 2012. **57**: p. 77-80.
- [13] Behnam Azad, B., et al., *Evaluation of a PSMA-targeted BNF nanoparticle construct*. Nanoscale, 2015. **7**(10): p. 4432-4442.
- [14] DeNardo, S.J., et al., *Development of tumor targeting bioprobes (111In-chimeric L6 monoclonal antibody nanoparticles) for alternating magnetic field cancer therapy*. Clinical Cancer Research, 2005. **11**(19): p. 7087s-7092s.
- [15] DeNardo, S.J., et al., *Thermal dosimetry predictive of efficacy of 111In-ChL6 nanoparticle AMF-induced thermoablative therapy for human breast cancer in mice*. Journal of Nuclear Medicine, 2007. **48**(3): p. 437-444.
- [16] Natarajan, A., et al., *NanoFerrite particle based radioimmunonanoparticles: binding affinity and in vivo pharmacokinetics*. Bioconjugate chemistry, 2008. **19**(6): p. 1211-1218.
- [17] Natarajan, A., et al., *Development of multivalent radioimmunonanoparticles for cancer imaging and therapy*. Cancer Biother. Radiopharm., 2008. **23**(1): p. 82-91.
- [18] Grüttner, C., et al., *Synthesis and antibody conjugation of magnetic nanoparticles with improved specific power absorption rates for alternating magnetic field cancer therapy*. J. Magn. Magn. Mat., 2007. **311**(1): p. 181-186.
- [19] Zhang, J., et al., *Herceptin-directed nanoparticles activated by an alternating magnetic field selectively kill HER-2 positive human breast cancer cells in vitro via hyperthermia*. Int. J. Hyperthermia, 2011. **27**(7): p. 682-697.
- [20] Ndong, C., et al., *Tumor Cell Targeting by Iron Oxide Nanoparticles Is Dominated by Different Factors In Vitro versus In Vivo*. PLoS ONE, 2015. **10**(2): p. e0115636.
- [21] Dixon, J.E., et al., *Highly efficient delivery of functional cargoes by the synergistic effect of GAG binding motifs and cell-penetrating peptides*. Proceedings of the National Academy of Sciences, 2016. **113**(3): p. E291-E299.
- [23] Simberg, D., et al., *Biomimetic amplification of nanoparticle homing to tumors*. Proc. Natl. Acad. Sci. U.S.A., 2007. **104**(3): p. 932-936.

9 Magnetic nanoparticles for stem cell tracking in soft tissue engineering approaches

Bernhard Frerich, Annika Kasten, Birte J. Siegmund

Rostock University Medical Center, Department of Oral and Maxillofacial Surgery, Rostock, Germany

Magnetic resonance imaging emerged as an excellent tool to track implanted stem cells in soft tissue engineering approaches. Kasten et al. and Siegmund et al. reported in consecutive *in vitro* and *in vivo* studies the feasibility of using BNF-Starch and nanomag[®]-D-spio nanoparticles, both 100 nm in diameter and coated with poly-D-lysine, for MRI-based stem cell tracking in a soft tissue engineering approach [1-3].

In the first step, both nanoparticle types were evaluated *in vitro* to determine their MRI properties as well as potential biological effects on adipose-tissue derived mesenchymal stem cells (ASC). Furthermore, to determine dose-dependent effects, three different nanoparticle concentrations were used for cell labeling. In general, no cytotoxic effects or alterations in metabolic activity of ASC were detected. Furthermore, intracellular localization of nanoparticles was examined and no co-localization with nuclei or mitochondria was found. Instead, nanoparticles were associated with lysosomal structures indicating a non-specific particle internalization pathway. Regarding cell proliferation, a dose-dependent increase was observed for both nanoparticle types compared to unlabeled control cells. Evaluation of multipotent differentiation potential of ASC into the adipogenic, osteogenic, and chondrogenic lineage revealed an overall, dose-dependent decrease due to nanoparticle application. In general, effects were more pronounced for BNF-Starch nanoparticles even at much lower concentrations than for nanomag[®]-D-spio nanoparticles. In contrast, MRI-properties of BNF-Starch nanoparticles in terms of R2* values were much better compared to nanomag[®]-D-spio nanoparticles.

In the second step, both nanoparticle types were tested under *in vivo* conditions. ASC were loaded with both types of nanoparticles (25 µg Fe/ml nanomag[®]-D-spio, 10 µg Fe/ml BNF-Starch) and seeded on collagenous three dimensional scaffolds which were implanted subcutaneously in the back region of severe combined immunodeficient mice (SCID mice, n=69). As control group, cell seeded scaffolds without nanoparticles were implanted. MRI scans were performed at several time points from 24 hours up to four months postoperatively and constructs were explanted afterwards for light microscopic histomorphometric analyses.

magnetic micro- and nanoparticles

As a result, nanoparticle loaded cells showed a high contrast in MRI (t2-tse-sequence) and could be detected inside the implanted scaffold (Fig. 1). Cells of the control group could not be separated from the surrounding tissue. The contrasting effect of both nanoparticle types was observed even after four months in a stage of total resorption of the scaffolds. Nanoparticles could be detected inside the scar tissue. Histomorphometric analysis showed iron oxide containing cells inside the constructs using Prussian blue staining. Except six mice which had to be excluded because of perioperative complications, animals of all groups did not show any signs of infection or other complications. Regarding the shrinkage of implanted scaffolds, no significant differences were observed between nanoparticle loaded groups and the control group.

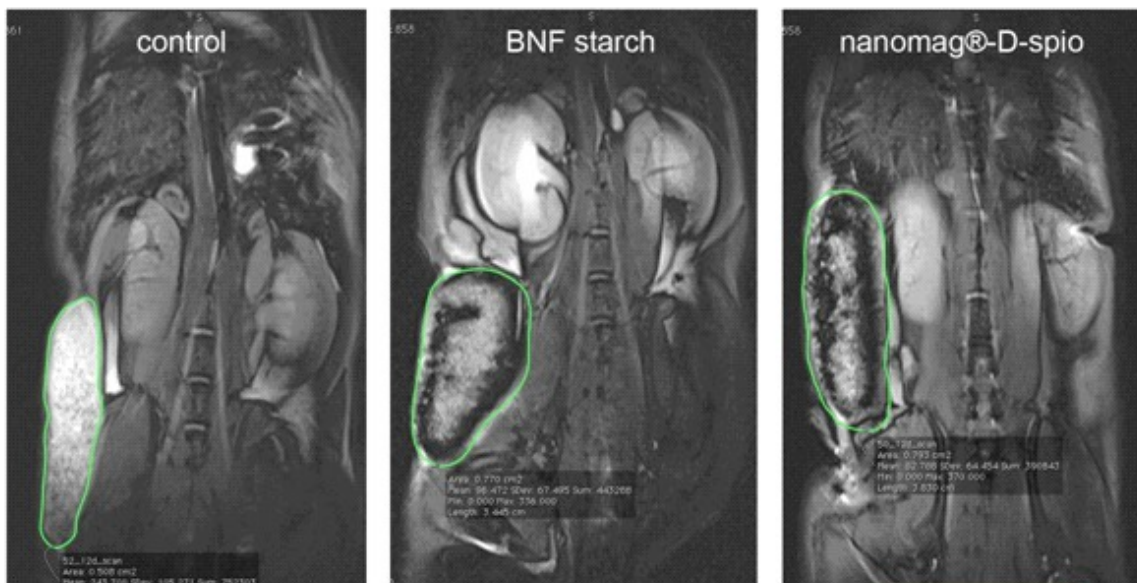


Fig. 1 : *In vivo* MRI scans of nanoparticle-labeled ASC.

T2-tse-maps (coronary views) of collagen scaffolds implanted in SCID mice are shown 12 days after implantation. Scaffold borders are marked with a green line. Only BNF-Starch and nanomag®-D-spio-labeled ASC lead to a high contrast on collagenous scaffolds compared to control cells.

MRI scans were performed by using a 7.1 T MR system (ClinScan, Bruker Corp., Billerica, MA, USA) in cooperation with the Department of Radiology and Neuroradiology, Greifswald University Medical Center.

References

- [1] Kasten, A., et al., *Comparative In Vitro Study on Magnetic Iron Oxide Nanoparticles for MRI Tracking of Adipose Tissue-Derived Progenitor Cells*. PloS one, 2014. **9**(9): p. e108055.
- [2] Kasten, A., et al., *Tracking of adipose tissue-derived progenitor cells using two magnetic nanoparticle types*. Journal of Magnetism and Magnetic Materials, 2015. **380**: p. 34-38.
- [3] Siegmund, B.J., et al., *MRI-tracking of transplanted human ASC in a SCID mouse model*. Journal of Magnetism and Magnetic Materials, 2016.

10 Applications of fluorescent magnetic particles

Cordula Grüttner

micromod Partikeltechnologie GmbH, Friedrich-Barnewitz-Str. 4, 18119 Rostock, Germany

10.1 Combination of optical imaging with Magnetic Resonance Imaging (MRI) or Magnetic Particle Imaging (MPI)

The combination of fluorescent and magnetic properties allows the design of nanoparticles for individual multimodal applications. Here we introduce highly specific applications of fluorescent magnetic nanoparticles that combine optical imaging and different magnetic techniques.

This combination allows for detection of fluorescent magnetic nanoparticles (MNPs) in a variety of biomedical applications. Rimkus et al. have studied the selective cell binding of fluorescent MNPs to endothelial cells as response to inflammatory factors. Functionalized nanomag®-CLD-spio particles were conjugated with antibodies that are directed to the cell-surface molecule VCAM-1 on. The antibodies were labelled with a near-infrared fluorochrome (DY-649) before conjugation (Fig. 1). Cell-binding properties of the targeted opto-magnetic probes were successfully evaluated on murine endothelial cells by fluorescence and MR imaging [1].

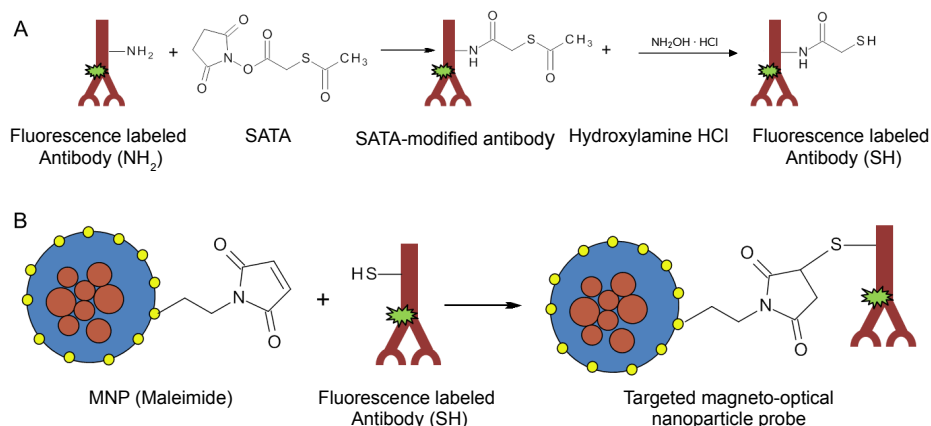


Figure 1: Reaction scheme of antibody-MNP conjugation using maleimide chemistry

MNPs are an interesting tool for labelling of stem/ progenitor cells for their homing and tracking by MRI or MPI in the field of regenerative medicine. Additional fluorescence labelling of the particles allows the visualization of the MNPs in the cell compartments to provide insight into the mechanism of particle-cell interaction. Kasten et al. labelled adipose tissue-derived progenitor cells with plain nanomag®-CLD-redF or BNF-Starch-redF particles for MR tracking. Poly-L-lysine (PLL) was used as transfection agent known for promoting cell adhesion. No co-localization between nanoparticles and mitochondria or nuclei was found. Both nanoparticle types appeared to be associated with lysosomes (Fig. 2) [2]. Cells were seeded onto collagen scaffolds and subcutaneously implanted into severe combined immunodeficient (SCID) mice. MRI analyses were performed visualizing nanoparticle-labelled cells using T2-weighted sequences over 28 days [3].

magnetic micro- and nanoparticles

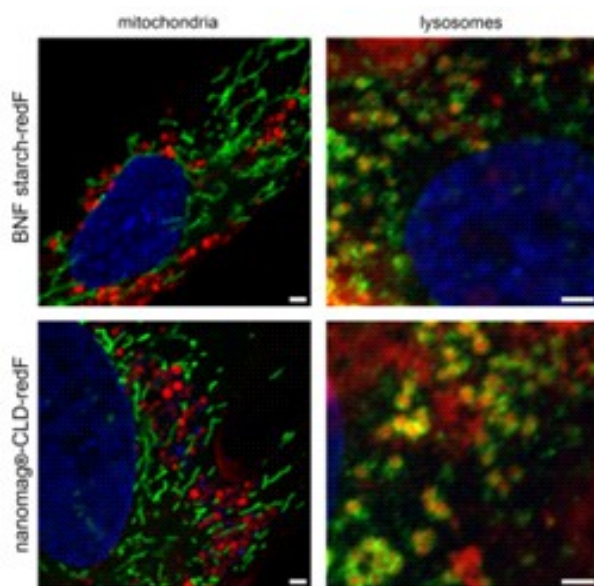
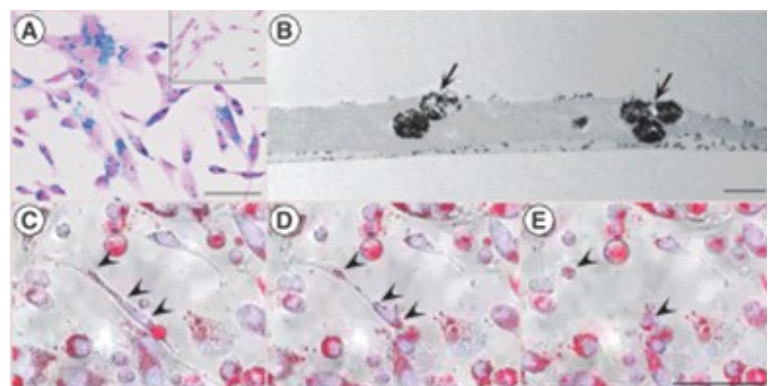


Figure 2. Intracellular localization of nanoparticles. Confocal laser scanning images of stem cells labeled with BNF-Starch-redF or nanomag®-CLD-redF and stained for mitochondria and lysosomes (both shown in green). Cell's nuclei were counterstained with Hoechst 33342 (blue).

To allow a direct labelling of stem cells without the use of any transfection agents perimag® particles with a medium positive zeta potential were developed (research name: M4A (plain), M4E (NH₂), M4G (red fluorescent)). Kilian et al. analyzed the suitability of aminated perimag® (M4E) for safe human mesenchymal stem cell (hMSC) labeling and determined cell labeling maintenance in 2D and 3D culture (Fig. 3) as well as the cell tracking possibility by MPI [4].

Figure 3. Microscopic characterization of labeled cells. (A) Prussian blue staining of M4E-labeled human mesenchymal stem cells revealed successful cell-particle interaction. Nonlabeled controls were Prussian blue, negative (A, inset). M4E particles were mostly found in lysosomes (B, arrows). Live cell imaging showed fluorescent M4G particle distribution in the course of human mesenchymal stem cell division (C-E, arrowheads). (C-E) Represent overlays of transmission light and fluorescent images and indicate different time points during cell division. Scale bars: (A, inset; E): 100 µm; (B): 1000 nm.



Multi-echo susceptibility weighted imaging (SWI) in combination with optical imaging was applied to monitor the transportation of dextran-iron oxide nanoparticles (nanomag®-CLD-redF) in normal and hydrocephalus rat brains via intrathecal delivery [5]. Hydrocephalus can be experimentally induced by producing a sustained increase in cerebrospinal fluid (CSF) osmolarity. This implies that the macromolecular content in the CSF is critical in determining the ventricular volume. Krishnamurthy et al. confirmed that intraventricularly injected nanomag®-CLD-redF particles are transported into the brain tissue prior to clearance into the vascular system [5].

10.2 Visualization of MNPs at controlled apoptosis by nanoparticle rotation in dynamic magnetic fields

Zhang et al. have designed a unique dynamic magnetic field (DMF) generator that can induce rotational movements of superparamagnetic iron oxide nanoparticles (SPIONs). It was examined whether the rotational nanoparticle movement could be used for remote induction of cell death by injuring lysosomal membrane structures. For this study **micromod** has conjugated 20 nm nanomag®-CLD-redF particles with antibodies targeting the lysosomal protein marker LAMP1. Remote activation of slow rotation of LAMP1-conjugated particles significantly improved the efficacy of cellular internalization of the nanoparticles. Confocal imaging of nanoparticle location in rat insulinoma cells demonstrated that the efficacy of cellular internalization of the particles was significantly improved and that cell apoptosis can be controlled by nanoparticle rotation via dynamic magnetic fields [6].

10.3 Nanoparticle-assisted optical tethering of endosomes (NOTE)

Chowdary et al. have developed a microfluidic platform that allows to visualize retrograde axonal endosome transport using ligand-bound quantum dots and oblique illumination imaging in microfluidic neuron cultures. This microfluidic platform was refined to study a novel phenomenon termed nanoparticle-assisted optical tethering of endosomes (NOTE) that made it possible to study the collective function of dyneins on retrograde axonal endosomes in live neurons [7]. To answer the question if the velocity of retrograde endosomes in axons reflects the number of dyneins on the endosomes, the retrograde axonal transport of Alexa-wheat germ agglutinin (WGA) (~2 nm), WGA-coated quantum dots (QDs, ~15 nm) and WGA-coated fluorescent iron oxide nanoparticles of different sizes (INPs, 30, 50, 100 nm) were analysed. Streptavidin coated 100 nm BNF-Starch-redF particles were conjugated with biotin-WGA as largest nanoparticles as model particles for this study [7].

References

- [1] Rimkus, G., et al., *mVCAM-1 specific iron oxide nanoparticles based probes for multimodal imaging purposes*. Biomed Tech, 2012. **57**: p. 77-80.
- [2] Kasten, A., et al., *Comparative In Vitro Study on Magnetic Iron Oxide Nanoparticles for MRI Tracking of Adipose Tissue-Derived Progenitor Cells*. PloS one, 2014. **9**(9): p. e108055.
- [3] Kasten, A., et al., *Tracking of adipose tissue-derived progenitor cells using two magnetic nanoparticle types*. Journal of Magnetism and Magnetic Materials, 2015. **380**: p. 34-38.
- [4] Kilian, T., et al., *Stem cell labeling with iron oxide nanoparticles: impact of 3D culture on cell labeling maintenance*. Nanomedicine, 2016. **11**(15): p. 1957-1970.
- [5] Krishnamurthy, S., et al., *SWI monitoring iron tagged dextran transportation in normal and hydrocephalus rat brains via intrathecal delivery*. Proc. Intl. Soc. Mag. Reson. Med., 2015. **23**: p. 0237.

- [6] Zhang, E., et al., *Dynamic Magnetic Fields Remote-Control Apoptosis via Nanoparticle Rotation*. ACS Nano, 2014. **8(4):3192-201**(8(4)): p. 3192-201.
- [7] Chowdary, P.D., et al., *Nanoparticle-assisted optical tethering of endosomes reveals the cooperative function of dyneins in retrograde axonal transport*. Scientific Reports, 2015. **5**: p. 18059.

11 Magnetic silica particles for radionuclide extraction

Cordula Grüttner

micromod Partikeltechnologie GmbH, Friedrich-Barnewitz-Str. 4, 18119 Rostock, Germany

The recovery of lanthanides and actinides from high level nuclear waste is an area of world-wide concern. Current approaches are based on the TRUEX process which utilizes the highly efficient, neutral, organophosphorous ligand octyl phenyl N,N-disobutyl carbamoylmethyl phosphine oxide (CMPO). Such CMPO moieties were incorporated at the wide rim of calix[4]arenes. This preorganization of the chelating CMPO ligands at the cup-shaped calixarene lead to a 100 fold increase in extraction efficiency combined with an enhanced selectivity for actinides and lighter lanthanides [1]. Solvent extraction methods using either simple or calix[4]arene-based systems, despite being highly efficient, do not lead to a marked decrease in waste volume and require large volumes of organic solvents. The application of magnetic particles has a high potential to circumvent these drawbacks. With a special surface design magnetic particles combine the selectivity of a solvent exchange ligand system with improved separation using the magnetically assisted chemical separation (MACS). After binding radionuclides the magnetic particles can be separated with a magnetic system, stripped to enable re-use, or vitrified.

Our 6 μm sicastar[®]-M particles were conjugated to calix[4]arenes bearing four CMPO moieties at the wide rim. The comparison of the extraction capacity for europium, americium and cerium of the CMPO-calix[4]arene bearing particles in comparison to particles with the same amount of simple CMPO ligands showed a significantly higher level of extraction of all radionuclides studied. This demonstrates the importance of pre-organization of the chelating ligands on a suitable macrocyclic scaffold, prior to their attachment at the particle surface [2].

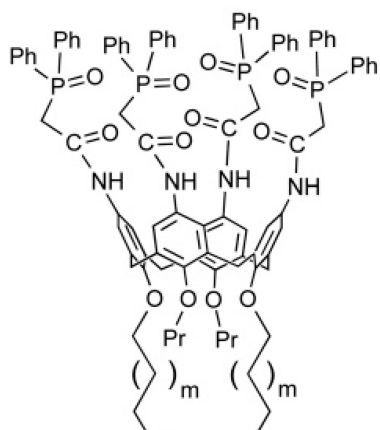


Figure 1. sicastar[®]-M particles with CMPO-bearing calix[4]arenes on the surface

Highly porous sicastar[®]-M particles with a diameter of 100 μm have a larger area for the immobilization of the chelator per g of particles than the non-porous particles. Therefore porous sicastar[®]-M particles were specially developed and conjugated to CMPO-containing calix[4]arenes via different spacer lengths between calixarene and particle surface (Figure 1).

magnetic micro- and nanoparticles

In comparison to solvent extraction methods a more efficient extraction of americium and europium from simulated nuclear waste conditions has been achieved [3]. In addition surprisingly high levels of cerium could be extracted with the magnetic particles. It was also demonstrated that shorter spacer lengths of three to five carbon atoms lead to a more efficient extraction of europium and americium than the highly flexible spacer of 10 carbon atoms due to additional intermolecular interaction between CMPO units of neighboring calixarenes. But the increasing spacer length to C10 results in an increasing selectivity of the sicastar[®]-M particles for americium over europium due to complex formation with the CMPO units of single calixarenes. Thus the optimal spacer length for calixarene attachment on a particle surface must prevent interactions between the CMPO units of different calixarenes for a complete exploitation of the pre-organization effect of the CMPO chelators [4] The possibility of recycling the magnetic particles was demonstrated for back extraction of europium from the particle surface. The complexation capacity of the particles did not change within four complexation-back extraction cycles, that makes the magnetic particles interesting for economic industrial nuclear waste water cleaning [3,4].

Another strategy for the design of magnetic particles for an efficient binding of radionuclides is the attachment of dendrimers with a high number of terminal amino groups on the surface of our porous 100 μm sicastar[®]-M particles. The dendrimer-coated magnetic particles were used as a universal platform for the covalent binding of CMPO (Figure 2)[5], tripodal CMPO compounds and other selective chelators for radionuclides [6]. The introduction of the dendrimer spacers led to a 50 to 400-fold increase in europium and americium extraction in comparison with corresponding chelator-coated particles without the dendrimer spacers.

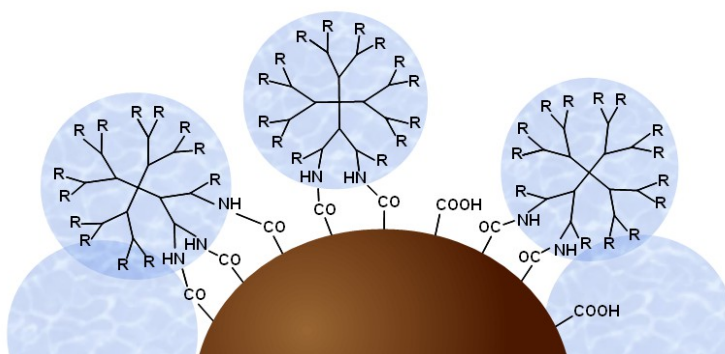
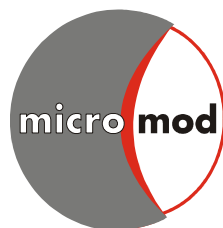


Figure 2. sicastar[®]-M particles with CMPO-bearing dendrimers on the surface (R=CMPO)

Back-extraction experiments with CMPO-bearing dendrimer-coated sicastar[®]-M particles demonstrated the possibility of multiple particle use, which also makes the application of CMPO-dendrimer coated particles an interesting alternative to conventional liquid-liquid extractions [5].

References

- [1] Arnaud-Neu F, Böhmer V, Dozol J-F, Grüttner C, Jakobi RA, Kraft D et al. Calixarenes with diphenylphosphoryl acetamide functions at the upper rim. A new class of highly efficient extractants for lanthanides and actinides. *J.Chem.Soc.Perkin Trans.2* 1996:1175-1182.
- [2] Matthews SE, Parzuchowski P, Garcia-Carrera A, Grüttner C, Dozol J-F, Böhmer V. Extraction of lanthanides and actinides by a magnetically assisted chemical separation technique based on CMPO-calix[4]arenes. *Chem. Commun.* 2001:417-418.
- [3] Grüttner C, Rudershausen S, Matthews SE, Wang P, Böhmer V, Dozol J-F. Selective extraction of lanthanides and actinides by magnetic silica particles with CMPO-modified calix[4]arenes on the surface. *Eur. Cells Materials* 2002;3:48-51.
- [4] Böhmer V, Dozol J-F, Grüttner C, Liger K, Matthews SE, Rudershausen S et al. Separation of lanthanides and actinides using magnetic silica particles bearing covalently attached tetra-CMPO-calix[4]arenes. *Org. Biomol. Chem.* 2004;2:2327-2334.
- [5] Grüttner C, Böhmer V, Casnati A, Dozol J-F, Reinhoudt DN, Reinoso-Garcia MM et al. Dendrimer-coated magnetic particles for radionuclide separation. *J Magn Magn Mat* 2005;293:559-566.
- [6] Reinoso-Garcia MM, Janczewski D, Reinhoudt DN, Verboom W, Malinowska E, Pietrzak M et al. CMP(O) tripodands: synthesis, potentiometric studies and extractions. *New J. Chem.* 2006;30:1480-1492.



Editor:
micromod Partikeltechnologie GmbH

Registergericht: Amtsgericht Rostock HRB 5837
Steuernummer: 4079/114/03352
Ust-Id Nr. (Vat No.): DE167349493

Compilation date - May the 10th, 2017
micromod Partikeltechnologie GmbH

www.micromod.de

micromod Partikeltechnologie GmbH
Friedrich-Barnewitz-Straße 4, D-18119 Rostock
Tel.: +49 381/54 34 56 10, Fax: +49 381/54 34 56 20
E-mail: info@micromod.de, Internet: www.micromod.de